Study on the Regulation of Adipocyte Differentiation and Maturation by Ser/Thr Phosphatase PPM1D

(Ser/Thr ホスファターゼ PPM1D による

脂肪細胞の分化および成熟に関する研究)

Graduate School of Chemical Sciences and Engineering,
Hokkaido University

Sae Uno

2025

Table of Contents

Abbreviations

ab-TAP-4PH	2-[4'-(4-aminobutyl)biphenyl-4-yl)]-1,3a,6a-triazapentalene
aP2	Adipocyte protein 2
ApoE	Apolipoprotein E
ATP	Adenosine triphosphate
β-AR	β-adrenergic receptor
BSA	Bovine Serum Albumin
C/EBP	CCAAT/ enhancer binding protein
CIDE	Cell death-inducing DFF45-like effector
Chk1/ Chk2	Checkpoint kinase 1/ 2
DCM	Dichloromethane
DMEM	Dulbecco's Modified Eagle's Medium-high glucose
DMSO	Dimethyl sulfoxide
ECM	Extracellular matrix
ER	Endoplasmic reticulum
EtOH	Ethanol
FA	Fatty acid
FAS	Fatty acid synthase
FBS	Fetal Bovine Serum
FFAs	Free fatty acids
FIT2	Fat storage-inducing transmembrane protein 2
Fsp27	Fat-specific protein 27
g-beige fat	Glycolytic beige fat
GLUT4	Solute carrier family 2 (facilitated glucose transporter), member 4

IBMX	3-Isobutyl-1-methylxanthine
LDs	Lipid droplets
LPL	Lipoprotein lipase
MDH	Monodansylpentane
MEF	Mouse Embryonic Fibroblast
NBCS	Newborn Calf Serum
PBS	Phosphate buffered saline
PGC-1α	Peroxisome proliferator-activated receptor gamma coactivator 1-alpha
PKA	Protein kinase A
PP1	Protein phosphatase 1
PPARγ	Peroxisome proliferator-activated receptor gamma
PPM1	Metal-dependent protein phosphatase 1
PPM1A	Metal-dependent protein phosphatase 1A
PPM1D	Metal-dependent protein phosphatase 1D
RPMI-1640	Roswell Park Memorial Institute medium-1640
TAP	1,3a,6a-triazapentalene
TAP-2CY4E1	2-(2-cyano-4-(methoxycarbonyl)phenyl)-1,3a,6a-triazapentalene
TAP-4PH	2-(biphenyl-4-yl)-1,3a,6a-triazapentalene
UCP1	Mitochondrial brown fat uncoupling protein 1
Wip1	Wild-type p53-induced phosphatase 1

1. General introduction

1.1. Adipocytes

Adipocytes are classified into white adipocytes, brown adipocytes, beige adipocytes, and pink adipocytes. They play a crucial role in maintaining energy homeostasis and metabolism [1, 2] (**Figure 1-1**). White adipocytes have large unilocular lipid droplets and a small number of mitochondria. White adipocytes store energy in the form of triacylglycerol and release it as fatty acids and glycerol during periods of nutrient deficiency, thereby regulating the nutritional levels throughout the body [3]. White adipocytes also regulate metabolism, inflammation, and appetite through the secretion of adipokines [4]. Obesity is caused by hyperplasia of white adipocytes due to hypertrophy of white adipocytes and differentiation of preadipocytes, which occurs due to the accumulation of excess fat [5]. Hypertrophy of white adipocytes undergo functional changes, exhibiting reduced signaling sensitivity, decreased insulin-induced glucose uptake, diminished hormone-induced lipolysis, decreased adiponectin secretion, and increased cytokine secretion. These changes can lead to immune cell infiltration and trigger inflammation [6]. The disfunction of perivascular adipocytes leads to altered secretion of adipokines and pro-inflammatory cytokines, increasing the risk of developing symptomatic cardiovascular diseases [7]. Adipocytes release inflammatory cytokines and extracellular matrix (ECM) proteins, promoting cancer growth [8, 9]. Additionally cancer cells promote the release of free fatty acids (FFAs) from white adipocytes, which in turn enhances the proliferation and migration of cancer cells [10]. Furthermore it has been shown that obese patients have worse clinical outcomes compared to non-obese patients [11, 12], suggesting that white adipocytes may be involved in the resistance to chemotherapy and radiotherapy in cancer treatment [13–15]. Adipogenesis is a complex multistep process in which preadipocytes differentiate into mature lipid-containing adipocytes. Adipogenesis includes a stage where multipotent stem cells differentiate into unipotent preadipocytes, and a subsequent stage where preadipocytes fully differentiate into mature adipocytes. Once multipotent stem cells commit to the

adipocyte lineage, they lose the ability to differentiate into other cell types, undergoing morphological and functional changes regulated by numerous signaling pathways, transcription factors, and genes [16]. Adipogenesis is strictly regulated by transcriptional cascades and signaling pathways (**Figure 1-2**) [17]. In the early stage of differentiation, CCAAT/ enhancer binding protein β (C/EBPβ) and C/EBPδ are temporarily highly expressed. In the middle stage, C/EBPβ and C/EBPδ stimulate peroxisome proliferator-activated receptor γ (PPARγ) and C/EBPα, which are crucial transcription factors for adipogenesis. PPARγ and C/EBPα cooperate to promote differentiation, and in the late stage of differentiation, they facilitate the induction of several adipocyte-specific genes, including perilipin, lipoprotein lipase (LPL), adipocyte protein 2 (aP2), and fatty acid synthase (FAS).

Brown adipocytes and beige adipocytes contain multilocular lipid droplets and numerous mitochondria. They are important for thermogenesis, as they dissipate chemical energy in the form of heat, playing a crucial role in body temperature and weight regulation [18]. Brown adipocytes develop prenatally. In contrast, beige adipocytes are induced from white adipocytes or preadipocytes in response to stimuli such as cold exposure, exercise, and endocrine hormones [19]. The mechanism by which beige adipocytes emerge is referred to as "beiging" or "browning." The differentiation mechanisms of beige adipocytes are gaining attention due to their potential applications in obesity treatments. However, excessive browning can have detrimental effects. It has been shown that browning of white adipocytes occurs in the early stages of cancer cachexia [20]. In cancer-associated cachexia, characterized by the wasting of skeletal muscle and adipose tissue, the ability of brown and beige adipocytes to dissipate energy as heat is suggested to contribute to a negative energy balance in patients with cancer cachexia.

Pink adipocytes differentiate from white adipocytes during pregnancy and produce milk [21]. Pink adipocytes form milk-secreting alveoli. Pink adipocytes are characterized by abundant intracellular organelles, including lipid droplets, cytoplasmic projections, mitochondria, peroxisomes, and rough endoplasmic reticulum, and have an epithelial cell-like structure. After lactation, pink adipocytes can

transdifferentiate into white adipocytes and brown adipocytes [22]. The loss of PPARγ expression in mammary secretory epithelial cells has been shown to create a microenvironment that promotes breast cancer [23], and PPARγ is identified as a key factor in the transdifferentiation of pink adipocytes to white adipocytes [24]. Understanding the mechanisms of reversible transdifferentiation from white adipocytes to pink adipocytes could elucidate the biology of breast cancer. Dysfunction of adipocyte differentiation and function can lead to diseases such as obesity and cancer, it is important to elucidate the mechanisms controlling adipocyte differentiation and function for the development of therapeutic strategies.

In recent years, subtypes of adipocytes with distinct functions have been identified [25]. In mouse adipose tissue, multiple adipocyte populations have been identified, each having distinct gene expression profiles and differing responses to metabolic and inflammatory cytokines, insulin, and growth hormones [26]. Subtype of white adipocytes have also been reported in mice fed a high-fat diet [27]. Two subtypes of brown adipocytes with differing expression levels of adiponectin, a type of adipokine produced by adipocytes, have been reported in the interscapular brown adipose tissue of mice [28]. *Adipoq*^{low} brown adipocytes have lower expression levels of thermogenic genes and reduced mitochondrial content compared to *Adipoq*^{high} brown adipocytes. Unlike the typical beige adipocytes induced by β-adrenergic receptor (β-AR) signaling in the inguinal white adipose tissue of mice, a subtype of beige adipocytes that is independent of β-AR signaling, known as glycolytic beige fat (g-beige fat), has been identified [29]. g-beige fat is characterized by high glucose catabolism. Multiple populations of beige adipocytes have been reported in mature adipocytes subjected to cold exposure and β3-adrenergic agonist stimulation [30]. Furthermore multiple subtypes of adipocytes with distinct gene expression profiles and functions have been reported in humans as well [31–33]. Obesity presents challenges in providing appropriate treatment options due to the variability in individual metabolic states. Therefore, elucidating the functions of diverse adipocyte subtypes is crucial for understanding individual

metabolic states and providing tailored treatment options.

1.2. Lipid droplets

Lipid droplets are intracellular organelles that serve as energy storage, consisting of a core of lipid esters surrounded by a monolayer of phospholipids [34, 35] (**Figure 1-3**). In adipocytes, lipid droplets are primarily composed of triacylglycerols. However, in many cell types, lipid droplets coexist with triacylglycerols and sterol esters in various ratios [36]. The biosynthesis of lipid droplets begins with the synthesis of triacylglycerols and sterol esters in the endoplasmic reticulum (ER), leading to the formation of neutral lipid lenses [37]. The expansion of the neutral lipid lens leads to the budding of lipid droplets from the ER membrane. Several ER membrane proteins, such as fat storage-inducing transmembrane protein 2 (FIT2) and Seipin, are suggested to play important roles in this budding process, although the detailed mechanisms remain unclear. After budding, lipid droplets continue to expand. They grow through the fusion of two lipid droplets, a process regulated by the cell death-inducing DFF45-like effector (CIDE) protein family members CIDEA, CIDEB, and CIDEC, as well as the PAT protein family member perilipin 1 [38]. In adipose tissue, CIDEC and perilipin 1 interact to promote the fusion of lipid droplets [39, 40]. However, the mechanisms of lipid droplet fusion remain unclear. Perilipin 1 localizes to the surface of lipid droplets and protects from lipolysis by inhibiting the access of lipases to the lipid droplets [41]. Perilipin 1 knockout mice exhibit a lean phenotype, demonstrating that perilipin 1 is a key protein responsible for lipid storage [42]. On the other hand, during lipolysis, perilipin 1 is phosphorylated by protein kinase A (PKA), which activates lipolysis [43]. The phosphorylation of perilipin 1 may play an important role in the regulation of both lipid droplet formation and lipolysis.

Lipid droplets are associated with various intracellular organelles [44]. The contact between lipid droplets and mitochondria serves as a site for both lipogenesis and lipolysis. During nutrient

deficiency, fatty acids released from lipid droplets are utilized for energy production via β-oxidation and the citric acid cycle in mitochondria. In contrast, in brown adipocytes, β-oxidation decreases while adenosine triphosphate (ATP) synthesis increases in mitochondria associated with lipid droplets.

1.3. Ser/Thr phosphatase PPM1D

Ser/Thr phosphatase PPM1D (Wip1, PP2Cδ) belongs to the PPM1 family, which is a group of Mn^{2+}/Mg^{2+} dependent Ser/Thr phosphatases [45]. PPM1D has been identified as a protein that is induced in a p53-dependent manner as a tumor suppressor protein [46]. PPM1D inactivates the p53 pathway through the dephosphorylation of p53 and other proteins involved in the p53 pathway [47, 48], serving as a negative feedback regulator of the p53 pathway (**Figure 1-4**). PPM1D possesses a proline-rich P-loop and a basic amino acid-rich B-loop, both of which are crucial for substrate recognition and enzyme functionality (**Figure 1-5**).

PPM1D is known as an oncogene due to its gene amplification and protein overexpression observed in many malignancies [49, 50]. Our laboratory has shown that PPM1D is involved in the promotion of nucleolus formation, which is one of the markers of cancer [51]. On the other hand, PPM1D is involved in various biological functions [52], and immune deficiencies and abnormalities in spermatogenesis have been reported in PPM1D knockout mice [53]. Our laboratory has also demonstrated that PPM1D exerts an inhibitory effect on neutrophil differentiation [54]. Additionally it has been reported that the tumor suppression is enhanced in neutrophils lacking PPM1D [55], suggesting that PPM1D plays a significant role in the regulation of neutrophil differentiation and function. Our laboratory has also reported that PPM1D is involved in the regulation of NT2 cell differentiation [56].

PPM1D has been suggested to be involved in metabolism. In apolipoprotein E (ApoE) knockout mice, atherosclerosis is induced. However, in ApoE and PPM1D double knockout mice, both atherosclerosis and macrophage lipid accumulation are suppressed. Furthermore, PPM1D knockout

mice show reduced weight gain and inhibition of fat accumulation when fed a high-fat diet [57]. It has been reported that PPM1D knockout mice exhibit insulin resistance [58], suggesting that PPM1D is involved in maintaining glucose homeostasis. In obese model mice, it has been reported that the expression level of PPM1D increases [59], suggesting that PPM1D is involved in obesity. Furthermore our laboratory has reported that the inhibition of PPM1D suppresses white adipocyte differentiation in 3T3-L1 cells [60], suggesting that PPM1D is involved in metabolic regulation through the control of white adipocyte differentiation.

Our laboratory is developing PPM1D-specific inhibitors and has successfully developed a potent PPM1D inhibitor, SL-176 [61] (**Figure 1-6**). SL-176 exhibits a higher inhibitory effect on PPM1D phosphatase activity compared to previously reported PPM1D inhibitors such as GSK2830371 and SPI-001 [62]. Furthermore, it shows minimal inhibitory effects on other PPM1 family members like PPM1A and on PPP family proteins such as PP1 and PP2A, demonstrating its high specificity for PPM1D. Furthermore, it has been reported that intraperitoneal injection of SL-176 in nude mice with xenografted medulloblastoma and neuroblastoma, which show PPM1D overexpression, results in tumor growth inhibition [63]. This suggests that SL-176 may be effective as an anticancer agent against cancers characterized by PPM1D overexpression.

1.4. Cell imaging

Fluorescent probes are widely used in the study of intracellular biochemical events. These probes include fluorescent proteins, quantum dots, and organic dyes. Organic small molecules are one of the important fluorescent probes, as they can be used for real-time analysis of cells and are relatively easy to use [64]. Furthermore, fluorescent probes allow for the simultaneous detection of multiple probes, making them an effective means for analyzing dynamic changes in living cells. Various fluorescent probes targeting specific organelles, such as LipiDye [65] and CellVue Kit for Fluorescent Cell Linker

[66], have been reported for live-cell imaging. Probes have also been developed to visualize cellular functions, such as the Cellular Thermoprobe for Fluorescence Ratio [67] for measuring intracellular temperature, Ap3 and SHG Imaging Dye [68] for detecting membrane potential, and Ageladine A [69] for detecting pH changes. However, methods that visualize cellular states without dependence on specific organelles or pH remain to be developed.

1.5. 1,3a,6a-triazapentalene (TAP) compounds

1,3a,6a-triazapentalene (TAP) is a compact 10π-system aromatic compound, and a simple synthesis method via click reactions has been reported [70] (**Figure 1-7**). TAP derivatives are highly sensitive small molecules that exhibit solubility in aqueous solvents, allowing for the control of their fluorescent properties by substitution. Substituents at the C2 position of TAP allow for the modulation of fluorescence wavelength, with electron-withdrawing substituents causing a red shift in wavelength as the strength of the inductive effect increases. Substituents at the C5 position of TAP can control the quantum yield, and the introduction of electron-donating substituents significantly enhances fluorescence intensity with minimal impact on fluorescence wavelength [71]. Substituents at the C4 position can provide further red shifts and enhance brightness, with the introduction of a phenyl group leading to a significant increase in the extinction coefficient [72]. Electron substituents at the C6 position induce a red shift in fluorescence wavelength and alter the quantum yield depending on the substituents at the C2 position, while electron-withdrawing substituents at the C6 position can quench fluorescence [73]. Introducing electron-withdrawing group at the C3 position allows for the synthesis of TAP derivatives that emit strong fluorescence [74]. A number of fluorescent probes suitable for cellular use have been synthesized from TAP derivatives. Our laboratory has reported that TAP-4PH, which contains a biphenyl group, is a novel fluorescent probe that exhibits fluorescence in the cytoplasm of living cells [75]. TAP-2CY4E1, which contains a 3-cyano benzoic acid moiety, has been reported to be taken up by

living cells and is usable as a fluorescent probe [76]. Furthermore various TAP derivatives with diverse properties have been reported, including the thiol-specific fluorescent labeling reagent TAP-VK1, which contains a vinyl ketone [77], and 2-*p*-nitrophenyl-TAP, which exhibits photo-induced cytotoxicity [78]. TAP derivatives allow for modulation of fluorescent properties and are highly useful fluorescent small molecules for use in living cells.

1.6. Deep learning for cell recognition

Deep learning has garnered significant attention in recent years for image analysis in the biosciences [79]. Deep learning refers to a set of machine learning techniques, specifically neural networks, that learn effective representations of data at multiple levels of abstraction. Common tasks related to images in biosciences include: Unsupervised image exploration: comparing features of image collections to identify morphological changes in cells during image-based drug screening; Image classification: predicting labels for images, such as determining whether stem cells have undergone differentiation; Image segmentation: identifying parts of an image corresponding to individual objects, such as recognizing single cells within images; Object tracking: tracking objects, like single cells within living embryos, across frames in a video. These applications highlight the versatility and impact of deep learning techniques in advancing research in the biosciences [80].

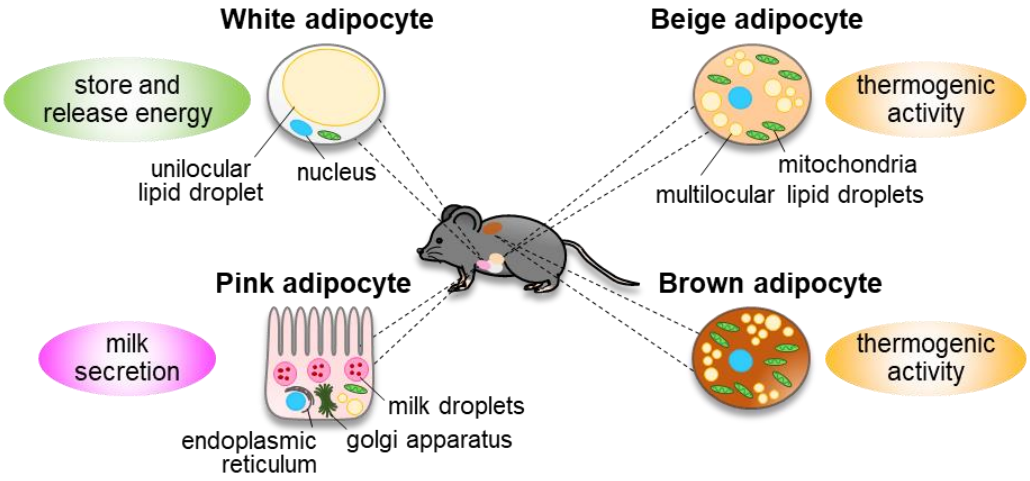

Figure 1-1. Adipocyte classification.

Adipocytes are classified into white, brown, beige, and pink adipocytes [2]. White adipocytes have unilocular lipid droplets, store and release energy. Brown and beige adipocytes are high mitochondrial contents and dissipate chemical energy in the form of heat. Pink adipocytes contain milk droplets and secrete milk.

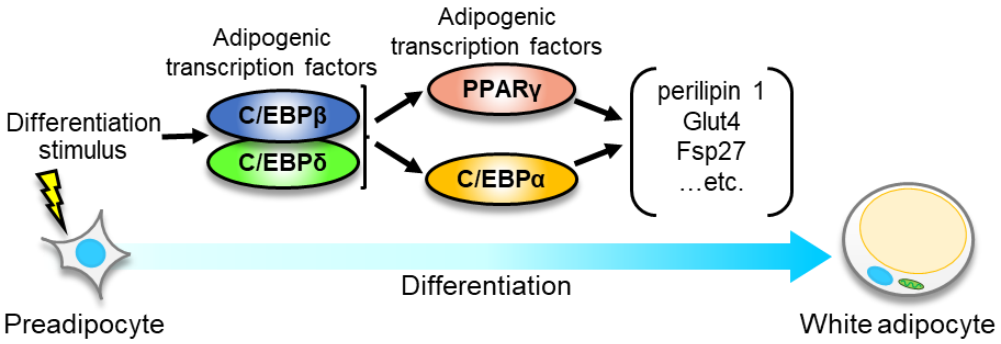

Figure 1-2. Transcriptional cascade of white adipocyte differentiation.

Preadipocytes receive differentiation stimuli, the expression of transcription factors C/EBPβ and C/EBPδ is induced, which in turn regulate the expression of PPARγ and C/EBPα. PPARγ and C/EBPα control the expression of downstream genes responsible for regulating adipocyte functions [17].

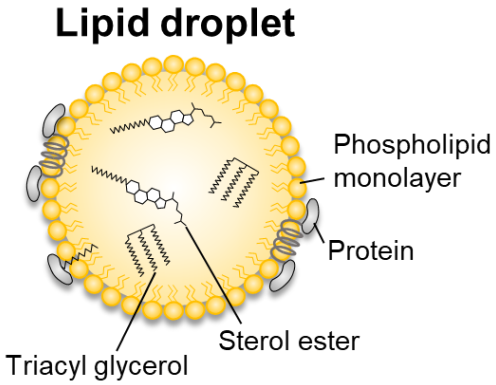

Figure 1-3. Structure of lipid droplets.

Lipid droplets are responsible for energy storage, composed of a core of lipid esters surrounded by a phospholipid monolayer [44].

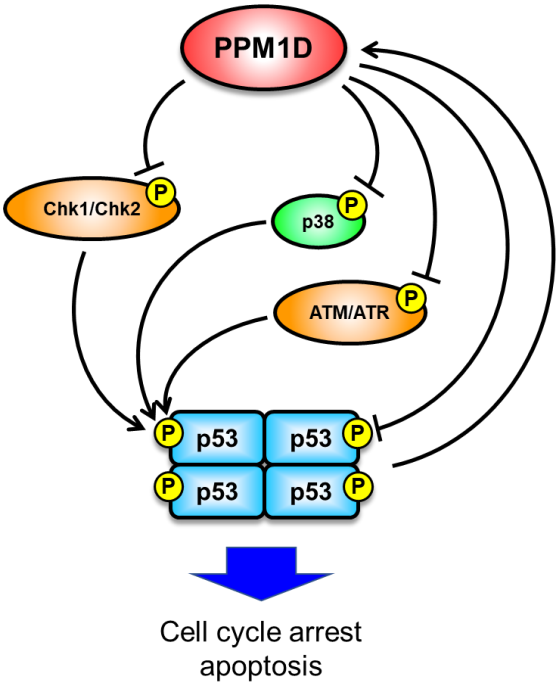

Figure 1-4. Functions of PPM1D on p53 pathway.

In p53 pathway, ATM/ATR, Chk1/Chk2, and p38 activate the tumor suppressor protein p53 by controlling its phosphorylation levels, thereby inducing cell cycle arrest or apoptosis. PPM1D is induced in a p53-dependent manner and inactivates the p53 pathway by dephosphorylating p53 and proteins involved in the p53 pathway. PPM1D serves as a negative feedback regulator of the p53 pathway [47, 48].

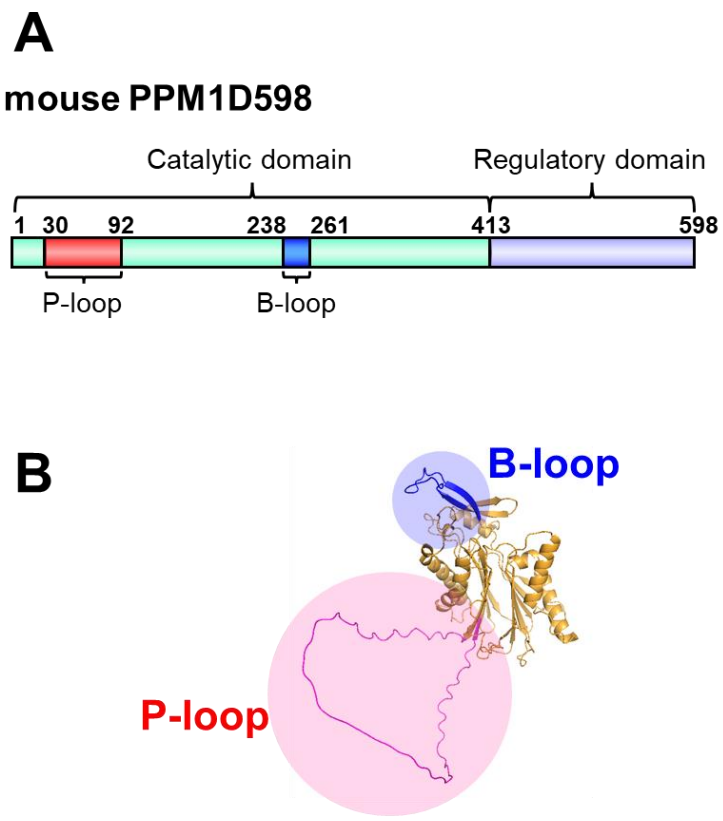

Figure 1-5. (A) Schematic structure of mouse PPM1D598. (B) AlphaFold structure of PPM1D catalytic domain.

PPM1D has a P-loop, a proline-rich region, and a B-loop, a region rich in basic amino acids. These regions are characteristic features of PPM1D and are important for substrate recognition and the enzyme's function.

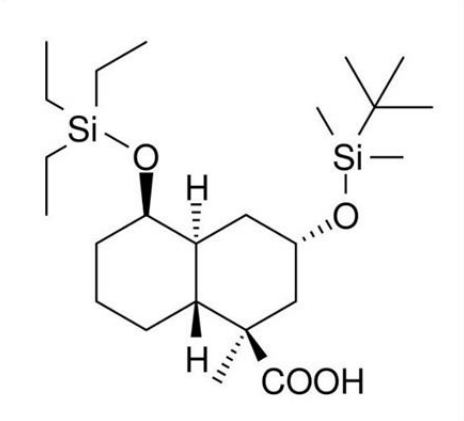

Figure 1-6. Structure of PPM1D-inhibitor SL-176.

SL-176 is a PPM1D-specific inhibitor with a molecular weight of 456.7. The *in vitro* IC_{50} of SL-176 is 110 ± 12.9 nM, and it potently and specifically inhibits the phosphatase activity of PPM1D [61].

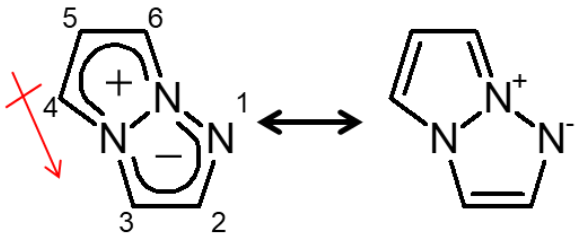

Figure 1-7. Structure of 1,3a,6a-triazapentalene.

1,3a,6a-triazapentalene is a compact 10π-electron aromatic compound [70].

1.7. Aim of this study

As described above, adipocytes are responsible for maintaining energy homeostasis and regulating metabolism. Abnormal differentiation and function of adipocytes are implicated in obesity, obesity-related diseases, and even cellular carcinogenesis [5, 7–9]. Understanding the mechanisms underlying their differentiation, maturation, and functional regulation is crucial for developing therapeutic strategies for obesity-related diseases and cancers. Lipid droplets are intracellular organelles that store energy [34, 35]. Excessive formation of lipid droplets causes hypertrophy of white adipocytes and leads to obesity. Elucidating the mechanisms of lipid droplet formation is important for the development of obesity treatments. However, the molecular mechanisms involved in lipid droplet formation and fusion remain unclear. Perilipin 1, localized on the surface of lipid droplets, is known to regulate lipid droplet formation [38–42]. It has been suggested that the phosphorylation of perilipin 1 plays an important role in this process [43]. On the other hand, the phosphatases involved in the dephosphorylation of perilipin 1 remain largely unknown. Identifying the dephosphorylation pathways targeting perilipin 1 and the associated phosphatases is therefore crucial for understanding the regulation of lipid droplet formation. PPM1D regulates metabolism and cell differentiation [56–59]. Furthermore, PPM1D is suggested to be involved in the regulation of adipocyte differentiation [60]; however, the precise mechanisms of this regulation remain unclear. In particular, investigating how PPM1D interacts with key signaling pathways during adipocyte differentiation could provide new insights into its regulatory role. Moreover, elucidating the functional implications of PPM1D in adipocyte maturation may uncover novel therapeutic targets for metabolic disorders.

To elucidate the molecular mechanisms that regulate adipocyte differentiation and maturation, it is essential to identify and analyze the differentiation and maturation states of adipocytes at the single-cell level. For this purpose, it is required to develop fluorescent probes that exhibit fluorescence broadly throughout the cell rather than in specific organelles, and whose fluorescence characteristics change

according to the cellular states. Furthermore, for continuous cell observation, fluorescence probes that can be removed from cells after observation and do not affect cellular function are desirable. TAP derivatives allow for the control of fluorescence properties through substituents [71–74], and a variety of fluorescent probes that are usable in cells have been synthesized [75–78]. Therefore, they are highly useful fluorescent small molecules for the development of cell identification methods. Deep learning, which has garnered significant attention in bioscience image analysis, is capable of extracting features and patterns from large amounts of data [79, 80]. Accordingly, deep learning can extract cellular characteristics from cell staining images using TAP derivatives and enable cell identification.

In this study, I elucidated the regulatory mechanisms of adipocyte differentiation and maturation mediated by PPM1D. Additionally, I developed a novel TAP derivative that visualizes the diverse states of cells and established a method for identifying cells at the single-cell level through multiplex staining with TAP derivatives and deep learning.

1.8. References

1. A. M. Cypess, Reassessing Human Adipose Tissue, *N. Engl. J. Med.*, **386**, 768–779 (2022). https://doi.org/10.1056/NEJMRA2032804/SUPPL_FILE/NEJMRA2032804_DISCLOSURES.PDF.
2. A. J. Richard, U. White, C. M. Elks, and J. M. Stephens, Adipose Tissue: Physiology to Metabolic Dysfunction, *Endotext*, (2020).
3. K. Frayn, Adipose tissue as a buffer for daily lipid flux, *Diabetologia*, **45**, 1201–1210 (2002). https://doi.org/10.1007/S00125-002-0873-Y/METRICS.
4. S. Galic, J. S. Oakhill, and G. R. Steinberg, Adipose tissue as an endocrine organ, *Mol. Cell. Endocrinol.*, **316**, 129–139 (2010). https://doi.org/10.1016/J.MCE.2009.08.018.
5. A. L. Ghaben and P. E. Scherer, Adipogenesis and metabolic health, *Nature Reviews Molecular Cell Biology*, **20**. Nature Publishing Group, 242–258 (2019). https://doi.org/10.1038/s41580-018-0093-z.
6. C. E. Hagberg and K. L. Spalding, White adipocyte dysfunction and obesity-associated pathologies in humans, *Nat. Rev. Mol. Cell Biol. 2023 254*, **25**, 270–289 (2023). https://doi.org/10.1038/s41580-023-00680-1.
7. Z. F. Huang Cao, E. Stoffel, and P. Cohen, Role of Perivascular Adipose Tissue in Vascular Physiology and Pathology, *Hypertension*, **69**, 770–777 (2017). https://doi.org/10.1161/HYPERTENSIONAHA.116.08451/ASSET/BC7BA20C-8FA8-415D-82D8-3A9EE0516453/ASSETS/GRAPHIC/770FIG01.JPEG.
8. B. Dirat, L. Bochet, M. Dabek, D. Daviaud, S. Dauvillier, B. Majed, Y. Y. Wang, A. Meulle, B. Salles, S. Le Gonidec, I. Garrido, G. Escourrou, P. Valet, and C. Muller, Cancer-Associated Adipocytes Exhibit an Activated Phenotype and Contribute to Breast Cancer Invasion, *Cancer Res.*, **71**, 2455–2465 (2011). https://doi.org/10.1158/0008-5472.CAN-10-3323.
9. N. Mubtasim, N. Moustaid-Moussa, and L. Gollahon, The Complex Biology of the Obesity-Induced, Metastasis-Promoting Tumor Microenvironment in Breast Cancer, *Int. J. Mol. Sci. 2022, Vol. 23, Page 2480*, **23**, 2480 (2022). https://doi.org/10.3390/IJMS23052480.
10. S. Balaban, R. F. Shearer, L. S. Lee, M. van Geldermalsen, M. Schreuder, H. C. Shtein, R. Cairns, K. C. Thomas, D. J. Fazakerley, T. Grewal, J. Holst, D. N. Saunders, and A. J. Hoy, Adipocyte lipolysis links obesity to breast cancer growth: adipocyte-derived fatty acids drive breast cancer cell proliferation and migration, *Cancer Metab. 2017 51*, **5**, 1–14 (2017). https://doi.org/10.1186/S40170-016-0163-7.
11. J. J. Castillo, F. Mulkey, S. Geyer, J. E. Kolitz, W. Blum, B. L. Powell, S. L. George, R. A. Larson, and R. M. Stone, Relationship between obesity and clinical outcome in adults with acute myeloid leukemia: A pooled analysis from four CALGB (alliance) clinical trials, *Am. J. Hematol.*, **91**, 199–204 (2016). https://doi.org/10.1002/AJH.24230.

12. A. Levitsky, K. Brismar, I. Hafström, K. Hambardzumyan, C. Lourdudoss, R. F. Van Vollenhoven, and S. Saevarsdottir, Obesity is a strong predictor of worse clinical outcomes and treatment responses in early rheumatoid arthritis: results from the SWEFOT trial, *RMD Open*, **3**, e000458 (2017). https://doi.org/10.1136/RMDOPEN-2017-000458.
13. J. Incio, J. A. Ligibel, D. T. McManus, P. Suboj, K. Jung, K. Kawaguchi, M. Pinter, S. Babykutty, S. M. Chin, T. D. Vardam, Y. Huang, N. N. Rahbari, S. Roberge, D. Wang, I. L. Gomes-Santos, S. B. Puchner, C. L. Schlett, U. Hoffmman, M. Ancukiewicz, S. M. Tolaney, I. E. Krop, D. G. Duda, Y. Boucher, D. Fukumura, and R. K. Jain, Obesity promotes resistance to anti-VEGF therapy in breast cancer by up-regulating IL-6 and potentially FGF-2, *Sci. Transl. Med.*, **10**, (2018). https://doi.org/10.1126/SCITRANSLMED.AAG0945/SUPPL_FILE/AAG0945_SM.PDF.
14. L. Bochet, A. Meulle, S. Imbert, B. Salles, P. Valet, and C. Muller, Cancer-associated adipocytes promotes breast tumor radioresistance, *Biochem. Biophys. Res. Commun.*, **411**, 102–106 (2011). https://doi.org/10.1016/J.BBRC.2011.06.101.
15. Y. Cao, Adipocyte and lipid metabolism in cancer drug resistance, *J. Clin. Invest.*, **129**, 3006–3017 (2019). https://doi.org/10.1172/JCI127201.
16. Q. Chen, P. Shou, C. Zheng, M. Jiang, G. Cao, Q. Yang, J. Cao, N. Xie, T. Velletri, X. Zhang, C. Xu, L. Zhang, H. Yang, J. Hou, Y. Wang, and Y. Shi, Fate decision of mesenchymal stem cells: adipocytes or osteoblasts?, *Cell Death Differ. 2016 237*, **23**, 1128–1139 (2016). https://doi.org/10.1038/cdd.2015.168.
17. E. D. Rosen, C. J. Walkey, P. Puigserver, and B. M. Spiegelman, Transcriptional regulation of adipogenesis, *Genes Dev.*, **14**, 1293–1307 (2000). https://doi.org/10.1101/GAD.14.11.1293.
18. W. Wang and P. Seale, Control of brown and beige fat development, *Nature Reviews Molecular Cell Biology*, **17**. Nature Publishing Group, 691–702 (2016). https://doi.org/10.1038/nrm.2016.96.
19. S. Kajimura, B. M. Spiegelman, and P. Seale, Brown and beige fat: Physiological roles beyond heat generation, *Cell Metabolism*, **22**. Cell Press, 546–559 (2015). https://doi.org/10.1016/j.cmet.2015.09.007.
20. M. Petruzzelli, M. Schweiger, R. Schreiber, R. Campos-Olivas, M. Tsoli, J. Allen, M. Swarbrick, S. Rose-John, M. Rincon, G. Robertson, R. Zechner, and E. F. Wagner, A switch from white to brown fat increases energy expenditure in cancer-associated cachexia, *Cell Metab.*, **20**, 433–447 (2014). https://doi.org/10.1016/j.cmet.2014.06.011.
21. A. Giordano, A. Smorlesi, A. Frontini, G. Barbatelli, and S. Cint, MECHANISMS IN ENDOCRINOLOGY: White, brown and pink adipocytes: the extraordinary plasticity of the adipose organ, *Eur. J. Endocrinol.*, **170**, R159–R171 (2014). https://doi.org/10.1530/EJE-13-0945.

22. S. Cinti, Pink Adipocytes, *Trends Endocrinol. Metab.*, **29**, 651–666 (2018). https://doi.org/10.1016/J.TEM.2018.05.007/ATTACHMENT/921560A2-A624-4641-B4C2-478E611E60C2/MMC2.DOCX.
23. A. J. Apostoli, G. E. A. Skelhorne-Gross, R. E. Rubino, N. T. Peterson, M. A. Di Lena, M. M. Schneider, S. K. Sengupta, and C. J. B. Nicol, Loss of PPARγ expression in mammary secretory epithelial cells creates a pro-breast tumorigenic environment, *Int. J. Cancer*, **134**, 1055–1066 (2014). https://doi.org/10.1002/IJC.28432.
24. Y. Yin, H. Yuan, C. Wang, N. Pattabiraman, M. Rao, R. G. Pestell, and R. I. Glazer, 3-Phosphoinositide-Dependent Protein Kinase-1 Activates the Peroxisome Proliferator-Activated Receptor-γ and Promotes Adipocyte Differentiation, *Mol. Endocrinol.*, **20**, 268–278 (2006). https://doi.org/10.1210/ME.2005-0197.
25. B. Maniyadath, Q. Zhang, R. K. Gupta, and S. Mandrup, Adipose tissue at single-cell resolution, *Cell Metab.*, **35**, 386–413 (2023). https://doi.org/10.1016/J.CMET.2023.02.002.
26. K. Y. Lee, Q. Luong, R. Sharma, J. M. Dreyfuss, S. Ussar, and C. R. Kahn, Developmental and functional heterogeneity of white adipocytes within a single fat depot, *EMBO J.*, **38**, (2019). https://doi.org/10.15252/EMBJ.201899291/SUPPL_FILE/EMBJ201899291-SUP-0003-TABLEEV2.XLSX.
27. A. K. Sárvári, E. L. Van Hauwaert, L. K. Markussen, E. Gammelmark, A. B. Marcher, M. F. Ebbesen, R. Nielsen, J. R. Brewer, J. G. S. Madsen, and S. Mandrup, Plasticity of Epididymal Adipose Tissue in Response to Diet-Induced Obesity at Single-Nucleus Resolution, *Cell Metab.*, **33**, 437-453.e5 (2021). https://doi.org/10.1016/J.CMET.2020.12.004/ASSET/7FB97ECC-A0BA-46DD-96C6-AF3CAC243E49/MAIN.ASSETS/GR6.JPG.
28. A. Song, W. Dai, M. J. Jang, L. Medrano, Z. Li, H. Zhao, M. Shao, J. Tan, A. Li, T. Ning, M. M. Miller, B. Armstrong, J. M. Huss, Y. Zhu, Y. Liu, V. Gradinaru, X. Wu, L. Jiang, P. E. Scherer, and Q. A. Wang, Low- and high-thermogenic brown adipocyte subpopulations coexist in murine adipose tissue, *J. Clin. Invest.*, **130**, 247–257 (2020). https://doi.org/10.1172/JCI129167.
29. Y. chen, K. ikeda, takeshi Yoneshiro, A. Scaramozza, K. tajima, Q. Wang, K. Kim, K. Shinoda, carlos Henrique Sponton, Z. Brown, A. Brack, and S. Kajimura, Thermal stress induces glycolytic beige fat formation via a myogenic state, (2019). https://doi.org/10.1038/s41586-018-0801-z.
30. C. A. O. de Biagi, S. S. Cury, C. de P. Alves, N. Rabhi, W. A. Silva, S. R. Farmer, R. F. Carvalho, and M. L. Batista, Multidimensional Single-Nuclei RNA-Seq Reconstruction of Adipose Tissue Reveals Adipocyte Plasticity Underlying Thermogenic Response, *bioRxiv*, 2021.02.16.431320 (2021). https://doi.org/10.1101/2021.02.16.431320.
31. M. P. Emont, C. Jacobs, A. L. Essene, D. Pant, D. Tenen, G. Colleluori, A. Di Vincenzo, A. M.

Jørgensen, H. Dashti, A. Stefek, E. McGonagle, S. Strobel, S. Laber, S. Agrawal, G. P. Westcott, A. Kar, M. L. Veregge, A. Gulko, H. Srinivasan, Z. Kramer, E. De Filippis, E. Merkel, J. Ducie, C. G. Boyd, W. Gourash, A. Courcoulas, S. J. Lin, B. T. Lee, D. Morris, A. Tobias, A. V. Khera, M. Claussnitzer, T. H. Pers, A. Giordano, O. Ashenberg, A. Regev, L. T. Tsai, and E. D. Rosen, A single-cell atlas of human and mouse white adipose tissue, *Nat. 2022 6037903*, **603**, 926–933 (2022). https://doi.org/10.1038/s41586-022-04518-2.

32. J. Bäckdahl, L. Franzén, L. Massier, Q. Li, J. Jalkanen, H. Gao, A. Andersson, N. Bhalla, A. Thorell, M. Rydén, P. L. Ståhl, and N. Mejhert, Spatial mapping reveals human adipocyte subpopulations with distinct sensitivities to insulin, *Cell Metab.*, **33**, 1869-1882.e6 (2021). https://doi.org/10.1016/J.CMET.2021.07.018.
33. W. Sun, H. Dong, M. Balaz, M. Slyper, E. Drokhlyansky, G. Colleluori, A. Giordano, Z. Kovanicova, P. Stefanicka, L. Balazova, L. Ding, A. S. Husted, G. Rudofsky, J. Ukropec, S. Cinti, T. W. Schwartz, A. Regev, and C. Wolfrum, snRNA-seq reveals a subpopulation of adipocytes that regulates thermogenesis, *Nat. 2020 5877832*, **587**, 98–102 (2020). https://doi.org/10.1038/s41586-020-2856-x.
34. K. Tauchi-Sato, S. Ozeki, T. Houjou, R. Taguchi, and T. Fujimoto, The surface of lipid droplets is a phospholipid monolayer with a unique fatty acid composition, *J. Biol. Chem.*, **277**, 44507–44512 (2002). https://doi.org/10.1074/jbc.M207712200.
35. T. Fujimoto and R. G. Parton, Not Just Fat: The Structure and Function of the Lipid Droplet, *Cold Spring Harb. Perspect. Biol.*, **3**, a004838 (2011). https://doi.org/10.1101/CSHPERSPECT.A004838.
36. D. Zweytick, K. Athenstaedt, and G. Daum, Intracellular lipid particles of eukaryotic cells, *Biochim. Biophys. Acta - Rev. Biomembr.*, **1469**, 101–120 (2000). https://doi.org/10.1016/S0005-2736(00)00294-7.
37. M. F. Renne, Y. A. Klug, and P. Carvalho, Lipid droplet biogenesis: A mystery "unmixing"?, *Semin. Cell Dev. Biol.*, **108**, 14–23 (2020). https://doi.org/10.1016/J.SEMCDB.2020.03.001.
38. G. Gao, F. J. Chen, L. Zhou, L. Su, D. Xu, L. Xu, and P. Li, Control of lipid droplet fusion and growth by CIDE family proteins, *Biochim. Biophys. Acta - Mol. Cell Biol. Lipids*, **1862**, 1197–1204 (2017). https://doi.org/10.1016/J.BBALIP.2017.06.009.
39. T. H. M. Grahn, Y. Zhang, M. J. Lee, A. G. Sommer, G. Mostoslavsky, S. K. Fried, A. S. Greenberg, and V. Puri, FSP27 and PLIN1 interaction promotes the formation of large lipid droplets in human adipocytes, *Biochem. Biophys. Res. Commun.*, **432**, 296–301 (2013). https://doi.org/10.1016/J.BBRC.2013.01.113.
40. Z. Sun, J. Gong, H. Wu, W. Xu, L. Wu, D. Xu, J. Gao, J. W. Wu, H. Yang, M. Yang, and P. Li, Perilipin1 promotes unilocular lipid droplet formation through the activation of Fsp27 in adipocytes, *Nat. Commun.*, **4**, 1–15 (2013). https://doi.org/10.1038/ncomms2581.

41. C. Sztalryd and D. L. Brasaemle, The perilipin family of lipid droplet proteins: Gatekeepers of intracellular lipolysis, *Biochim. Biophys. Acta - Mol. Cell Biol. Lipids*, **1862**, 1221–1232 (2017). https://doi.org/10.1016/J.BBALIP.2017.07.009.
42. J. Martinez-Botas, J. B. Anderson, D. Tessier, A. Lapillonne, B. H. J. Chang, M. J. Quast, D. Gorenstein, K. H. Chen, and L. Chan, Absence of perilipin results in leanness and reverses obesity in Leprdb/db mice, *Nat. Genet. 2000 264*, **26**, 474–479 (2000). https://doi.org/10.1038/82630.
43. A. R. Kimmel and C. Sztalryd, The Perilipins: Major Cytosolic Lipid Droplet–Associated Proteins and Their Roles in Cellular Lipid Storage, Mobilization, and Systemic Homeostasis*, *http://dx.doi.org/10.1146/annurev-nutr-071813-105410*, **36**, 471–509 (2016). https://doi.org/10.1146/ANNUREV-NUTR-071813-105410.
44. J. A. Olzmann and P. Carvalho, Dynamics and functions of lipid droplets, *Nature Reviews Molecular Cell Biology*, **20**. Nature Publishing Group, 137–155 (2019). https://doi.org/10.1038/s41580-018-0085-z.
45. G. Lu and Y. Wang, Functional diversity of mammalian type 2C protein phosphatase isoforms: New tales from an old family, *Clinical and Experimental Pharmacology and Physiology*, **35**. John Wiley & Sons, Ltd, 107–112 (2008). https://doi.org/10.1111/j.1440-1681.2007.04843.x.
46. M. Fiscella, H. Zhang, S. Fan, K. Sakaguchi, S. Shen, W. E. Mercer, G. F. Vande Woude, P. M. O'Connor, and E. Appella, Wip1, a novel human protein phosphatase that is induced in response to ionizing radiation in a p53-dependent manner, *Proc. Natl. Acad. Sci. U. S. A.*, **94**, 6048–6053 (1997). https://doi.org/10.1073/pnas.94.12.6048.
47. X. Lu, B. Nannenga, and L. A. Donehower, PPM1D dephosphorylates Chk1 and p53 and abrogates cell cycle checkpoints, *Genes Dev.*, **19**, 1162–1174 (2005). https://doi.org/10.1101/gad.1291305.
48. S. Shreeram, O. N. Demidov, W. K. Hee, H. Yamaguchi, N. Onishi, C. Kek, O. N. Timofeev, C. Dudgeon, A. J. Fornace, C. W. Anderson, Y. Minami, E. Appella, and D. V. Bulavin, Wip1 Phosphatase Modulates ATM-Dependent Signaling Pathways, *Mol. Cell*, **23**, 757–764 (2006). https://doi.org/10.1016/j.molcel.2006.07.010.
49. D. V. Bulavin, O. N. Demidov, S. Saito, P. Kauraniemi, C. Phillips, S. A. Amundson, C. Ambrosino, G. Sauter, A. R. Nebreda, C. W. Anderson, A. Kallioniemi, A. J. Fornace, and E. Appella, Amplification of PPM1D in human tumors abrogates p53 tumor-suppressor activity, *Nat. Genet.*, **31**, 210–215 (2002). https://doi.org/10.1038/ng894.
50. G. B. Li, X. L. Zhang, L. Yuan, Q. Q. Jiao, D. J. Liu, and J. Liu, Protein Phosphatase Magnesium-Dependent 1δ (PPM1D) mRNA Expression Is a Prognosis Marker for Hepatocellular Carcinoma, *PLoS One*, **8**, (2013). https://doi.org/10.1371/journal.pone.0060775.
51. Y. Kozakai, R. Kamada, J. Furuta, Y. Kiyota, Y. Chuman, and K. Sakaguchi, PPM1D controls

nucleolar formation by up-regulating phosphorylation of nucleophosmin, *Sci. Rep.*, **6**, 1–11 (2016). https://doi.org/10.1038/srep33272.

52. R. Kamada, F. Kudoh, S. Ito, I. Tani, J. I. B. Janairo, J. G. Omichinski, and K. Sakaguchi, Metal-dependent Ser/Thr protein phosphatase PPM family: Evolution, structures, diseases and inhibitors, *Pharmacol. Ther.*, **215**, 107622 (2020). https://doi.org/10.1016/j.pharmthera.2020.107622.
53. J. Choi, B. Nannenga, O. N. Demidov, D. V. Bulavin, A. Cooney, C. Brayton, Y. Zhang, I. N. Mbawuike, A. Bradley, E. Appella, and L. A. Donehower, Mice Deficient for the Wild-Type p53-Induced Phosphatase Gene (Wip1) Exhibit Defects in Reproductive Organs, Immune Function, and Cell Cycle Control, *Mol. Cell. Biol.*, **22**, 1094–1105 (2002). https://doi.org/10.1128/mcb.22.4.1094-1105.2002.
54. R. Kamada, F. Kudoh, F. Yoshimura, K. Tanino, and K. Sakaguchi, Inhibition of Ser/Thr phosphatase PPM1D induces neutrophil differentiation in HL-60 cells, *J. Biochem.*, **162**, 303–308 (2017). https://doi.org/10.1093/JB/MVX032.
55. B. Uyanik, A. R. Goloudina, A. Akbarali, B. B. Grigorash, A. V. Petukhov, S. Singhal, E. Eruslanov, J. Chaloyard, L. Lagorgette, T. Hadi, E. V. Baidyuk, H. Sakai, L. Tessarollo, B. Ryffel, S. J. Mazur, F. Lirussi, C. Garrido, E. Appella, and O. N. Demidov, Inhibition of the DNA damage response phosphatase PPM1D reprograms neutrophils to enhance anti-tumor immune responses, *Nat. Commun. 2021 121*, **12**, 1–15 (2021). https://doi.org/10.1038/s41467-021-23330-6.
56. S. Ogasawara, Y. Chuman, T. Michiba, R. Kamada, T. Imagawa, and K. Sakaguchi, Inhibition of protein phosphatase PPM1D enhances retinoic acid-induced differentiation in human embryonic carcinoma cell line, *J. Biochem.*, **165**, 471–477 (2019). https://doi.org/10.1093/jb/mvy119.
57. X. Le Guezennec, A. Brichkina, Y. F. Huang, E. Kostromina, W. Han, and D. V. Bulavin, Wip1-dependent regulation of autophagy, obesity, and atherosclerosis, *Cell Metab.*, **16**, 68–80 (2012). https://doi.org/10.1016/j.cmet.2012.06.003.
58. H. L. Armata, S. Chamberland, L. Watts, H. J. Ko, Y. Lee, D. Y. Jung, J. K. Kim, and H. K. Sluss, Deficiency of the Tumor Promoter Gene *wip1* Induces Insulin Resistance, *Mol. Endocrinol.*, **29**, 28–39 (2015). https://doi.org/10.1210/me.2014-1136.
59. D. Li, L. Zhang, L. Xu, L. Liu, Y. He, Y. Zhang, X. Huang, T. Zhao, L. Wu, Y. Zhao, K. Wu, H. Li, X. Yu, T. Zhao, S. Gong, M. Fan, and L. Zhu, WIP1 phosphatase is a critical regulator of adipogenesis through dephosphorylating PPARγ serine 112, *Cell. Mol. Life Sci.*, **74**, 2067–2079 (2017). https://doi.org/10.1007/s00018-016-2450-4.
60. R. Kamada, N. Kimura, F. Yoshimura, K. Tanino, and K. Sakaguchi, Inhibition of lipid droplet formation by Ser/Thr protein phosphatase PPM1D inhibitor, SL-176, *PLoS One*, **14**, (2019).

https://doi.org/10.1371/journal.pone.0212682.

61. S. Ogasawara, Y. Kiyota, Y. Chuman, A. Kowata, F. Yoshimura, K. Tanino, R. Kamada, and K. Sakaguchi, Novel inhibitors targeting PPM1D phosphatase potently suppress cancer cell proliferation, *Bioorganic Med. Chem.*, **23**, 6246–6249 (2015). https://doi.org/10.1016/j.bmc.2015.08.042.
62. H. Yagi, Y. Chuman, Y. Kozakai, T. Imagawa, Y. Takahashi, F. Yoshimura, K. Tanino, and K. Sakaguchi, A small molecule inhibitor of p53-inducible protein phosphatase PPM1D, *Bioorganic Med. Chem. Lett.*, **22**, 729–732 (2012). https://doi.org/10.1016/j.bmcl.2011.10.084.
63. J. Milosevic, D. Treis, S. Fransson, G. Gallo-Oller, B. Sveinbjörnsson, N. Eissler, K. Tanino, K. Sakaguchi, T. Martinsson, M. Wickström, P. Kogner, and J. I. Johnsen, PPM1D Is a Therapeutic Target in Childhood Neural Tumors, *Cancers 2021, Vol. 13, Page 6042*, **13**, 6042 (2021). https://doi.org/10.3390/CANCERS13236042.
64. X. Tian, L. C. Murfin, L. Wu, S. E. Lewis, and T. D. James, Fluorescent small organic probes for biosensing, *Chem. Sci.*, **12**, 3406–3426 (2021). https://doi.org/10.1039/D0SC06928K.
65. M. Taki, K. Kajiwara, E. Yamaguchi, Y. Sato, and S. Yamaguchi, Fused Thiophene- S, S-dioxide-Based Super-Photostable Fluorescent Marker for Lipid Droplets, *ACS Mater. Lett.*, **3**, 42–49 (2021). https://doi.org/10.1021/ACSMATERIALSLETT.0C00451/SUPPL_FILE/TZ0C00451_SI_007.CIF.
66. Vinod Kaimal, Z. Chu, Y. Y. Mahller, B. Papahadjopoulos-Sternberg, T. P. Cripe, S. K. Holland, and X. Qi, Saposin C coupled lipid nanovesicles enable cancer-selective optical and magnetic resonance imaging, *Mol. Imaging Biol.*, **13**, 886–897 (2011). https://doi.org/10.1007/S11307-010-0417-7/FIGURES/6.
67. S. Uchiyama, T. Tsuji, K. Ikado, A. Yoshida, K. Kawamoto, T. Hayashi, and N. Inada, A cationic fluorescent polymeric thermometer for the ratiometric sensing of intracellular temperature, *Analyst*, **140**, 4498–4506 (2015). https://doi.org/10.1039/C5AN00420A.
68. T. Mizuguchi, M. Yasui, and M. Nuriya, High-Resolution Plasma Membrane-Selective Imaging by Second Harmonic Generation, *iScience*, **9**, 359–366 (2018). https://doi.org/10.1016/J.ISCI.2018.11.008.
69. Y. Q. Wang and Z. H. Miao, Marine-Derived Angiogenesis Inhibitors for Cancer Therapy, *Mar. Drugs 2013, Vol. 11, Pages 903-933*, **11**, 903–933 (2013). https://doi.org/10.3390/MD11030903.
70. K. Namba, A. Osawa, S. Ishizaka, N. Kitamura, and K. Tanino, Direct synthesis of fluorescent 1,3a,6a-triazapentalene derivatives via click-cyclization-aromatization cascade reaction, *J. Am. Chem. Soc.*, **133**, 11466–11469 (2011). https://doi.org/10.1021/JA203917R/SUPPL_FILE/JA203917R_SI_002.CIF.
71. K. Namba, A. Mera, A. Osawa, E. Sakuda, N. Kitamura, and K. Tanino, One-pot synthesis of

highly fluorescent 2,5-disubstituted-1,3a,6a- triazapentalene, *Org. Lett.*, **14**, 5554–5557 (2012). https://doi.org/10.1021/OL302668Y/SUPPL_FILE/OL302668Y_SI_001.PDF.

72. A. Nakayama, S. Nishio, A. Otani, A. Mera, A. Osawa, K. Tanino, and K. Namba, Substituent Effect at the C4-Position of 1,3a,6a-Triazapentalene, *Chem. Pharm. Bull.*, **64**, 830–837 (2016). https://doi.org/10.1248/CPB.C16-00196.
73. A. Mera, M. Ito, A. Nakayama, and K. Namba, Synthesis of 2,6-Disubstituted-1,3a,6a-Triazapentalenes and Their Fluorescence Properties, *Chem. Lett.*, **46**, 539–542 (2017). https://doi.org/10.1246/CL.170078.
74. B. Verbelen and W. Dehaen, Two-Step Synthesis of Fluorescent 3-Arylated 1,3a,6a-Triazapentalenes via a Three-Component Triazolization Reaction, *Org. Lett.*, **18**, 6412–6415 (2016). https://doi.org/10.1021/ACS.ORGLETT.6B03309/ASSET/IMAGES/LARGE/OL-2016-03309J_0001.JPEG.
75. R. Kamada, F. Tano, F. Kudoh, N. Kimura, Y. Chuman, A. Osawa, K. Namba, K. Tanino, and K. Sakaguchi, Effective Cellular Morphology Analysis for Differentiation Processes by a Fluorescent 1,3a,6a-Triazapentalene Derivative Probe in Live Cells, *PLoS One*, **11**, e0160625 (2016). https://doi.org/10.1371/JOURNAL.PONE.0160625.
76. K. Namba, A. Osawa, A. Nakayama, A. Mera, F. Tano, Y. Chuman, E. Sakuda, T. Taketsugu, K. Sakaguchi, N. Kitamura, and K. Tanino, Synthesis of yellow and red fluorescent 1,3a,6a-triazapentalenes and the theoretical investigation of their optical properties, *Chem. Sci.*, **6**, 1083–1093 (2015). https://doi.org/10.1039/C4SC02780A.
77. A. Nakayama, A. Otani, T. Inokuma, D. Tsuji, H. Mukaiyama, A. Nakayama, K. Itoh, A. Otaka, K. Tanino, and K. Namba, Development of a 1,3a,6a-triazapentalene derivative as a compact and thiol-specific fluorescent labeling reagent, *Commun. Chem. 2020 31*, **3**, 1–9 (2020). https://doi.org/10.1038/s42004-019-0250-0.
78. D. Tsuji, A. Nakayama, R. Yamamoto, S. Nagano, T. Taniguchi, R. Sato, S. Karanjit, N. Muguruma, T. Takayama, K. Itoh, and K. Namba, 1,3a,6a-Triazapentalene derivatives as photo-induced cytotoxic small fluorescent dyes, *Commun. Chem. 2023 61*, **6**, 1–11 (2023). https://doi.org/10.1038/s42004-023-00838-0.
79. A. Kan, Machine learning applications in cell image analysis, *Immunol. Cell Biol.*, **95**, 525–530 (2017). https://doi.org/10.1038/ICB.2017.16.
80. E. Moen, D. Bannon, T. Kudo, W. Graf, M. Covert, and D. Van Valen, Deep learning for cellular image analysis, *Nat. Methods 2019 1612*, **16**, 1233–1246 (2019). https://doi.org/10.1038/s41592-019-0403-1.

2. Regulation of adipocyte differentiation and lipid droplet formation by PPM1D

2.1. Abstract

White adipocytes contain large lipid droplets, store and release energy, and secrete multiple hormones. Excessive formation of lipid droplets, which are responsible for energy storage, leads to hypertrophy of white adipocytes and contributes to obesity. Understanding the mechanisms of adipocyte differentiation and lipid droplet formation is crucial for the developing effective obesity treatments. Ser/Thr phosphatase PPM1D is involved in various physiological functions, including metabolism and immune responses. Our laboratory has demonstrated that the addition of the PPM1D inhibitor SL-176 during the induction of white adipocyte differentiation significantly suppresses this process. This study highlights the novel functions of PPM1D in regulating white adipocyte differentiation and lipid droplet formation.

PPM1D knockdown during white adipocyte differentiation showed that adipocyte differentiation was inhibited in the early phase by PPM1D inhibition. By inhibiting PPM1D in a differentiation stage-dependent manner, it was revealed that PPM1D regulates lipid droplet formation through the control of adipocyte differentiation in the early stage, while it is involved in differentiation-independent lipid droplet formation in the middle and late stages. Inhibition of PPM1D in mature white adipocytes led to the formation of multilocular lipid droplets with reduced size. Analysis of function of PPM1D on perilipin 1, which regulates lipid droplet formation, showed that PPM1D controls lipid droplet formation through dephosphorylation of perilipin 1 at Ser511. Furthermore, although mitochondrial activity significantly increased in PPM1D-inhibited mature white adipocytes, there was no change in the expression levels of beige adipocyte differentiation markers. These findings suggest that PPM1D-inhibited mature white adipocytes may differentiate into a novel subtype with characteristics resembling beige adipocytes. These results indicate that PPM1D has novel functions in adipocyte differentiation and lipid droplet formation.

2.2. Introduction

White adipocytes are important cells that store and release energy, secrete hormones, and play a critical role in maintaining energy homeostasis [1, 2]. Excessive fat accumulation leads to hypertrophy and hyperplasia of white adipocytes through the differentiation of preadipocytes, which leads to obesity [3]. Therefore, elucidating the mechanisms of differentiation and maturation of white adipocytes is important for developing effective obesity treatments.

The differentiation of white adipocytes is tightly regulated by transcriptional cascades and signaling pathways. The most frequently used *in vitro* model to study adipogenesis is 3T3-L1 cells, immortalized murine cells derived from Swiss 3T3 mouse embryos [4]. 3T3-L1 cells differentiate into white adipocytes in response to stimulation by the peptide hormone insulin, the synthetic glucocorticoid dexamethasone, and the cAMP enhancer 3-Isobutyl-1-methylxanthine (IBMX) [5]. Upon differentiation stimuli, the transcription factors C/EBPβ and C/EBPδ are induced, which in turn regulate the expression of PPARγ and C/EBPα, key transcription factors critical for adipocyte differentiation [6, 7]. PPARγ and C/EBPα regulate each other's expression [8], and control the expression of genes involved in lipid droplet formation, including perilipin 1 and Fat-specific protein 27 (FSP27) [9].

Lipid droplets store lipids and play a crucial role in cellular energy metabolism [10]. In mature white adipocytes, lipid droplets are involved in the storage of energy and respond to lipolytic stimulation to regulate the accumulation and release of fat. Therefore, it is important to elucidate pathways for lipid droplet formation that are independent of adipocyte differentiation. Lipid droplets are present in various cell types, and the size of these droplets is associated with various diseases, including cancer, obesity, and diabetes [11, 12]. Lipid size is involved in lipolysis and lipophagy in hepatocytes [13]. Lipolysis has been reported to target larger lipid droplets compared to smaller lipid droplets, while smaller lipid droplets have also been reported to promote lipolysis [14]. These findings suggest that lipolysis is not solely dependent on lipid droplet size. However, it remains unclear how lipid droplet size and lipolysis

are regulated in different cell types.

In mature white adipocytes, various proteins localize to the surface of lipid droplets and regulate their fusion, fission and lipolysis. Perilipin 1 localizes to the surface of lipid droplets and regulates lipid droplet fusion while preventing lipase binding during lipolysis [15]. The C-terminal region of perilipin 1 has been reported to contain multiple phosphorylation sites, which are suggested to regulate its function. It has been reported that perilipin 1 is phosphorylated by PKA in response to lipolytic stimuli via adrenergic receptors, promoting lipolysis [16]. It has been reported that PP1 is involved in the dephosphorylation of perilipin 1, although the specific target sites remain unknown [17]. Furthermore, the enzymes involved in the dephosphorylation of perilipin 1 in lipid droplet formation have not yet been identified.

Beige adipocytes have multilocular lipid droplets and numerous mitochondria, and they are involved in thermogenesis [18]. Mitochondria localize the mitochondrial brown fat uncoupling protein 1 (UCP1), which uncouples oxidative phosphorylation and electron transport to facilitate ATP-independent thermogenesis [19]. Beige adipocytes are induced from preadipocytes and white adipocytes in response to stimuli such as cold exposure, exercise, and endocrine hormones [20]. The characteristic properties of beige adipocytes induced in response to stimuli have attracted much attention and are expected to elucidate the regulatory mechanism of beige adipocyte induction and to develop into an obesity treatment method. Recently, various subtypes of adipocytes with distinct gene expression and functions have been discovered [21]. Obesity presents challenges in providing appropriate treatments due to the variability in individual metabolic states. Understanding the functions of diverse adipocyte subtypes can aid in developing therapies informed by an understanding of individual metabolic conditions.

Ser/Thr phosphatase PPM1D has been identified as a p53-inducible phosphatase that is involved in maintaining cellular homeostasis through negative feedback of the p53 pathway [22–24].

PPM1D is involved in metabolism. In ApoE deficient mice, atherosclerosis is induced; however, in ApoE and PPM1D double knockout mice, both atherosclerosis and macrophage lipid accumulation are suppressed. Additionally, PPM1D knockout mice exhibit reduced weight gain and fat accumulation when subjected to a high-fat diet [25]. It has been reported that PPM1D expression levels are increased in obesity model mice [26], suggesting that PPM1D plays a role in fat accumulation and obesity. Furthermore our laboratory has demonstrated that the addition of the potent and specific PPM1D inhibitor SL-176 [27] to 3T3-L1 cells inhibits white adipocyte differentiation and reduces lipid droplet content and size [28]. These results suggest that PPM1D is involved in adipocyte differentiation and lipid droplet formation.

In this study, I elucidated the role of PPM1D in adipocyte differentiation and lipid droplet formation.

2.3. Experimental procedures

2.3.1. Cell lines and materials

3T3-L1 mouse fibroblasts were obtained from the Japanese Collection of Research Bioresource (JCRB, Tokyo, Japan). PPM1D inhibitor SL-176 was obtained from Laboratory of Organic Chemistry II (Faculty of Science, Hokkaido University). SL-176 was dissolved in ethanol (EtOH, Wako Pure Chemical Industries, Osaka, Japan, Cat. 054-07225) to prepare a 8 mM stock solution. Insulin (Sigma-Aldrich, St. Louis, MO, USA, Cat. I0516-5ML) was 10 mg/mL stock. Dexamethasone (Wako Pure Chemical Industries, Osaka, Japan, Cat. 047-18863) was dissolved in EtOH to prepare a 10 mM stock solution. 3-Isobutyl-1-methylxanthine (IBMX, Sigma-Aldrich, St. Louis, MO, USA, Cat. I5789-250MG) was dissolved in dimethyl sulfoxide (DMSO, Wako Pure Chemical Industries, Osaka, Japan, Cat. 045-28335) to prepare a 100 mM stock solution. Control siRNA (Invitrogen, Waltham, MA, USA, Cat. 12935-300) and mouse PPM1D (744-768) siRNA were 20 μM stock. Plasmids containing the Venus-NLS-2A-perilipin 1(S511A/D) vectors were used for transient expression of perilipin 1 Ser511A and Ser511D mutants. The plasmids contained Venus-NLS and perilipin 1 (S511A) or perilipin 1 (S511D) linked by a 2A self-processing peptide. Plasmids were dissolved in TE (pH8.0) to prepare a 0.4 mg/mL stock solution. Monodansylpentane (MDH, AUTODOT, Abgent, San Diego, CA, USA, Cat. SM1000a) was dissolved in DMSO to prepare a 0.1 M stock solution. MitoTracker Red CM-H_2Xros (Invitrogen, Waltham, MA, USA, Cat. M7513) was dissolved in DMSO to prepare a 1 mM stock solution.

2.3.2. Cell manipulation

3T3-L1 cells were grown in Dulbecco's modified Eagle's medium (DMEM, Sigma-Aldrich, St. Louis, MO, USA, Cat. D5796-500ML) supplemented with 10% v/v Newborn Calf Serum (NBCS, Thermo Fisher Scientific, Waltham, MA, USA, Cat. 16010159) at 37℃ in an atmosphere of 5% CO_2.

3T3-L1 cells were seeded at a density of 8×10^4 cells or 2.0×10^5 cells per 35 mm dish or 1.6×10^4 cells in 24-well plates. Two days after 100% cell confluence (day 0), the cells were cultured in differentiation medium (MDI) [DMEM containing 10% v/v fetal bovine serum (FBS) with 100 units/mL penicillin and 100 μg/mL streptomycin (P/S, Thermo Fisher Scientific, Waltham, MA, USA, Cat. 15140-122) with 1.0 μg/mL insulin, 1.0 μM dexamethasone, and 0.5 mM IBMX]. Cells were placed in adipocyte maintenance medium (DMEM containing 10% FBS with P/S and 1.0 μg/mL insulin) on day 1. Media were exchanged to adipocyte maintenance medium every 2 days until day 8 of induction of differentiation. For experiments with the PPM1D inhibitor (SL-176), the cells were treated with 15 μM SL-176 for the indicated time.

For transient transfection of siRNA for PPM1D, 3T3-L1 cells detached with Trypsin-EDTA (0.25%), phenol red (Trypsin-EDTA, Thermo Fisher Scientific, Waltham, MA, USA, Cat. 25200056) The cells were suspended in DMEM 10% NBCS and centrifuged at 1,000 rpm for 5 min, then remove the solution. After adding 2 mL of phosphate buffer saline (PBS), the cells were resuspended and counted. The required number of cells was transferred to a 50 mL conical tube, centrifuged again at 1,000 rpm for 5 min, and remove the solution. The cells were resuspended in Resuspension buffer and transferred to a microtube. Control siRNA or mouse PPM1D (744-768) siRNA was added, the cells were then electroporated at 1,300 V, 20 ms using the Neon Transfection System (Thermo Fisher Scientific, Waltham, MA, USA). After electroporation, the cells were seeded in 24-well plate in DMEM supplemented with 10% NBCS. After 48 h, the cells were cultured in a differentiation medium and cultured as described above.

For the experiments involving overexpression of perilipin 1, 3T3-L1 cells were seeded at a density of 8×10^4 cells per 35-mm dish and induced to differentiate. On day 3 of differentiation, 3T3-L1 cells were washed with PBS twice then add 100 μL of Trypsin-EDTA and incubated at 37°C for 5 min. Once the cells detached, resuspended in 750 μL of Opti-MEM (Thermo Fisher Scientific, Waltham,

MA, USA, Cat. 31985-070) and centrifuge at 1,400 rpm for 5 min then remove the solution. 3T3-L1 cells were resuspended in 200 μL of Opti-MEM containing 20 μg of perilipin 1 expression plasmids. The cells were then electroporated at 500 μF/160 V using the Bio-Rad Gene Pulser Xcell System (Bio-Rad, Hercules, CA, USA). After electroporation, the cells were seeded on micro cover glass (Matsunami Glass Industries, Osaka, Japan, Cat. 83-0205) in 35-mm dish in DMEM supplemented with 10% FBS and 1.0 μg/mL insulin. After 24 h, the cells were washed with PBS twice and cultured in an adipocyte maintenance medium for 2 days. Then transfer the micro cover glass to 24-well plate, the cells were fixed, and the size of the lipid droplets (LDs) was analyzed.

2.3.3. RT-qPCR

3T3-L1 cells were seeded at the density of 2.0×10^5 cells per 35 mm dish or 1.6×10^4 cells in 24-well plates and cultured as described above. Cells were washed with PBS and lysed with TRIzol reagent (Thermo Fisher Scientific, Waltham, MA, USA, Cat. 15596-026). For the purification of total RNA, to the collected 1 mL of TRIzol solution, 200 μL of chloroform (Kanto Chemical, Tokyo, Japan, Cat. 07278-00) was added, and to 500 μL of TRIzol solution, 100 μL of chloroform was added. After mixing well, the solution was centrifuged at 15,000 rpm for 2 min at 4°C to separate the aqueous and organic layers. The upper aqueous layer was collected, and 500 μL of 2-Propanol (Wako Pure Chemical Industries, Osaka, Japan, Cat. 168-21675) was added to it, followed by thorough mixing and centrifugation at 15,000 rpm for 15 min at 4°C. After confirming the RNA precipitation and pellet formation, the supernatant was removed. The pellet was washed with 80% EtOH/UltraPure Distilled Water (Invitrogen, Waltham, MA, USA, Cat. 10977-015), centrifuged at 15,000 rpm for 5 min at 4°C, and the supernatant was removed. This washing step was performed twice. The pellet was then dried for about 10 min until it became clear. 10 or 20 μL of UltraPure Distilled Water was added to dissolve the pellet, which was incubated at 55°C for 5 min, and then immediately placed on ice. The absorbance of

this RNA solution was measured at 260 nm with a spectrophotometer to quantify the RNA concentration. The RNA concentration for each sample was normalized to 100 ng/μL. Total RNA was then reverse transcribed using the PrimerScript II 1st strand cDNA Synthesis Kit (TaKaRa, Kusatsu, Japan, Cat. 6210A) with Random 6 mers. To each well of an 8 strips PCR tube, 3 μL of RNase free dH_2O, 1 μL of Random 6 mers, 1 μL of dNTP Mixture, and 5 μL of 100 ng/μL RNA were added. The mixture was incubated at 65°C for 5 min using a Thermal Cycler, and then immediately placed on ice. Subsequently, to each well, a buffer mixture was added (4 μL of 5× PrimeScript II buffer, 0.5 μL of RNase Inhibitor, 1 μL of PrimeScript II RTase, and 4.5 μL of RNase free dH_2O). Reverse transcription was performed using a Thermal Cycler at 30°C for 10 min, 42°C for 60 min, and 75°C for 15 min. Quantitative PCR was performed to each well of a 96-well plate for PCR reactions, 5 μL of PowerUp SYBR Green Master Mix (Thermo Fisher Scientific, Waltham, MA, USA, Cat. A25742), 2 μL of cDNA, 1 μL of primer, and 2 μL of H_2O were added and react with a CFX96 Touch Real-Time PCR Detection System (Bio-Rad, Hercules, CA, USA) The primers used for quantitative PCR were as follows: PPM1D forward, GATGTATGTAGCGCATGTAGGTG; PPM1D reverse, GTTCTGGCTTGTGATCTTGTGT; perilipin 1 forward, GGGACCTGTGAGTGCTTCC; perilipin 1 reverse, GTATTGAAGAGCCGGGATCTTTT; PPARγ forward, CCATTCTGGCCCACCAAC; PPARγ reverse, AATGCGAGTGGTCTTCCATCA; C/EBPα forward, CAAGAACAGCAACGAGTACCG; C/EBPα reverse, GTCACTGGTCAACTCCAGCAC; UCP1 forward, AGGCTTCCAGTACCATTAGGT; UCP1 reverse, CTGAGTGAGGCAAAGCTGATTT; CIDEA forward, TGCTCTTCTGTATCGCCCAGT; CIDEA reverse, GCCGTGTTAAGGAATCTGCTG; actin forward, GGCTGTATTCCCCTCCATCG; actin reverse, CCAGTTGGTAACAATGCCATGT.

2.3.4. Oil red O staining

3T3-L1 cells were cultured at the density of 8×10^4 cells per 35 mm dish. The Oil Red O

solution constituted 0.3% Oil Red O (Wako Pure Chemical Industries, Osaka, Japan, Cat. 154-02072) /2-propanol (Nacalai, Kyoto, Japan, Cat. 29113-53): H_2O in the ratio 6:4 and was filtered through a 0.45 μm PVDF filter (Millipore, Burlington, MA, USA, Cat. SLHVX13NL). Then, 5% v/v 60% 2-propanol/H_2O was added to the filtered solution. After day 8 or day 15 of differentiation, cells were washed with PBS once, then fixed with 10% neutral-buffered formalin (Wako Pure Chemical Industries, Osaka, Japan, Cat.062-01661) for 30 min, washed with PBS once, and 60% 2-propanol/H_2O once, and then added to an Oil Red O solution for 30 min. After staining, the cells were washed with 60% 2-propanol/H_2O three times. Cells were added PBS, photographs of the stained dish were taken using scanner GT-X900 (EPSON, Nagano, Japan). After drying the dishes overnight, extraction of Oil Red O was performed with 100% 2-propanol, once for 60 min and twice for 10 min. For quantification, the absorbance of Oil Red O extract was measured at 490 nm with a microplate reader.

2.3.5. Lipid droplet imaging and quantification

3T3-L1 cells were seeded at a density of 1.6×10^4 cells on micro cover glass in a 24-well plate and cultured as described above. On day 8 or day 15 of differentiation, transfer the micro cover glass to 24-well plate, cells were washed with PBS twice, then fixed with 10% neutral-buffered formalin for 1 h, washed with PBS three times. Cells were permeabilized with 0.2% Triton X-100 (Nacalai, Kyoto, Japan, Cat. 355-01) /PBS for 15 min, washed with PBS three times, then incubated with 10 μM MDH/PBS for 30 min, washed with PBS three times. Mounted a micro cover glass onto a microscope slide (Matsunami Glass Industries, Osaka, Japan, Cat. SO318) and then observed via fluorescence microscopy (BZ-9000, KEYENCE, Osaka, Japan) using a DAPI filter (Ex360/40 Dm400 Em460/50).

The diameter of the LDs was measured in nine images of MDH-stained cells (approximately 100–200 cells). The LDs in the images were circled and painted black using PowerPoint. Figures that overlapped with each other were removed. The images obtained were used as the binarized images. The

size of the circles was measured using Image J. For the experiments involving overexpression of perilipin 1, the cells that showed Venus fluorescence were analyzed.

2.3.6. Mitochondria imaging

3T3-L1 cells were seeded at a density of 2.0×10^5 cells in a 35-mm high μ-Dish (ibidi GmbH, Germany, Cat. ib81156) and cultured as described above. After differentiation for 8 days followed by treatment with SL-176 for 7 days, cells were washed with PBS and incubated with 500 nM MitoTracker Red CM-H2Xros/Opti-MEM for 30 min at 37°C. After incubation, cells were washed with PBS twice, then add Opti-MEM and observed via fluorescence microscopy (BZ-9000) using a TRITC filter (Ex540/25 Dm565 Em605/55).

2.3.7. Lipolysis assay

3T3-L1 cells were seeded at a density of 2.0×10^5 cells in a 35-mm high μ-Dish or 4.0×10^4 cells in 24-well plates, and cultured as described above. After differentiation for 8 days followed by treatment with SL-176 for 7 days, the cells were washed with PBS and treated with Lipolysis medium [DMEM, 2% fatty acid (FA)-free BSA (Sigma-Aldrich, St. Louis, MO, USA, Cat. A1595-50ML), 10 μM isoprenaline hydrochloride (Sigma-Aldrich, St. Louis, MO, USA, Cat. I5627-5G)/H_2O]. The cells were observed using BZ-9000 at the indicated time points.

For the quantification of free glycerol and FAs, after 1 h of incubation with lipolysis medium, the cells were incubated in measurement medium (DMEM, 2% FA-free BSA), and the amount of free glycerol and FAs released in the supernatant at 0.5, 1, 2, and 4 h was analyzed using free glycerol reagent (Sigma-Aldrich, St. Louis, MO, USA, Cat. F6428-40ML) and LabAssay NEFA kit (Wako Pure Chemical Industries, Osaka, Japan, Cat. 294-63601), respectively.

2.3.8. Protein purification

His-PPM1D(1-413) was expressed in E. coli BL21 (DE3) pLysS cells and purified by affinity purification and gel filtration, as previously described [27]. The cell pellets were lysed using a French press and then TALON resins (Clontech, Mountain View, CA, USA) with an elution buffer (25 mM HEPES-NaOH pH 6.8, 150 mM imidazole, 200 mM NaCl, 1 mM $MgCl_2$, 10% glycerol, and 0.005% Triton X-100) and were used to purify His-PPM1D(1-413). His-PPM1D(1-413) was further purified using a HiTrap Q FF (GE Healthcare, Chicago, IL, USA) column and eluted with IEX start buffer and IEX elution buffer, followed by Superdex 75 (GE Healthcare Bioscience, Chicago, IL, USA) column with SEC elution buffer (25 mM HEPES-NaOH pH 6.8, 500 mM NaCl, 1 mM $MgCl_2$, 10% glycerol, and 0.005% Triton X-100).

2.3.9. *In vitro* phosphatase assay

The phosphopeptides perilipin 1(487–498, 492pS) [Ac-WGPARRVS(P)DSFFRP-NH_2], perilipin 1(506-517, 511pS) [Ac-WGGRAQYS(P)QLRKKS-OH], and perilipin 1(506-517, 517pS) [Ac-WGGRAQYSQLRKKS(P)-OH] were synthesized using Fmoc-standard chemistry and purified. The phosphatase activity of PPM1D was assayed by measuring the absorbance of the released *p*-nitrophenol or free phosphate by BIOMOL GREEN (Enzo Life Sciences, Farmingdale, NY, USA). Briefly, all assays were carried out using 50 mM Tris-HCl pH 7.5, 50 mM NaCl, 0.1 mM EGTA, 0.02% 2-mercaptoethanol, 30 mM $MgCl_2$, 40 μM substrate peptide with His-PPM1D(1-413) (2, 5, and 10 nM) for 25 min at 30℃. The number of phosphatases released was calculated using a standard phosphatase curve.

2.3.10. Statistical analysis

Statistical analysis was performed by one-way analysis-of-variance (ANOVA) followed by

Tukey's post-hoc test, Wilcoxon Rank Sum test, or Student's *t*-test using R version 4.2.1 (https://www.r-project.org/ (accessed on 23 June 2022)) [29]. For all comparisons, a p value of < 0.05 was considered statistically significant. * $p < 0.05$, ** $p < 0.01$, *** $p < 0.001$.

2.4. Results

2.4.1. Effects of PPM1D knockdown on white adipocyte differentiation

To clarify the role of PPM1D in white adipocyte differentiation, PPM1D was knocked down in the adipocyte differentiation model cell line 3T3-L1, and white adipocyte differentiation was induced. The mRNA expression levels of PPM1D, the transcription factor PPARγ, which regulates adipocyte differentiation, and perilipin 1, a downstream gene of PPARγ that controls lipid droplet formation, were analyzed using RT-qPCR. The results showed that in the siPPM1D condition, the mRNA expression of *Ppm1d* was reduced by 50% compared to siCtrl (**Figure 2-1**). The mRNA expression of *Pparg* decreased by approximately 50% in siPPM1D on differentiation day 1. The mRNA expression of *Plin1* decreased by about 50% in siPPM1D on differentiation day 3.

PPM1D knockdown reduced the mRNA expression of *Pparg*, a transcription factor that regulates adipocyte differentiation, which may have contributed to the decreased expression of its downstream gene, *Plin1*. These results indicate that PPM1D is involved in promoting white adipocyte differentiation by regulating the mRNA expression levels of PPARγ, a key transcription factor in adipocyte differentiation.

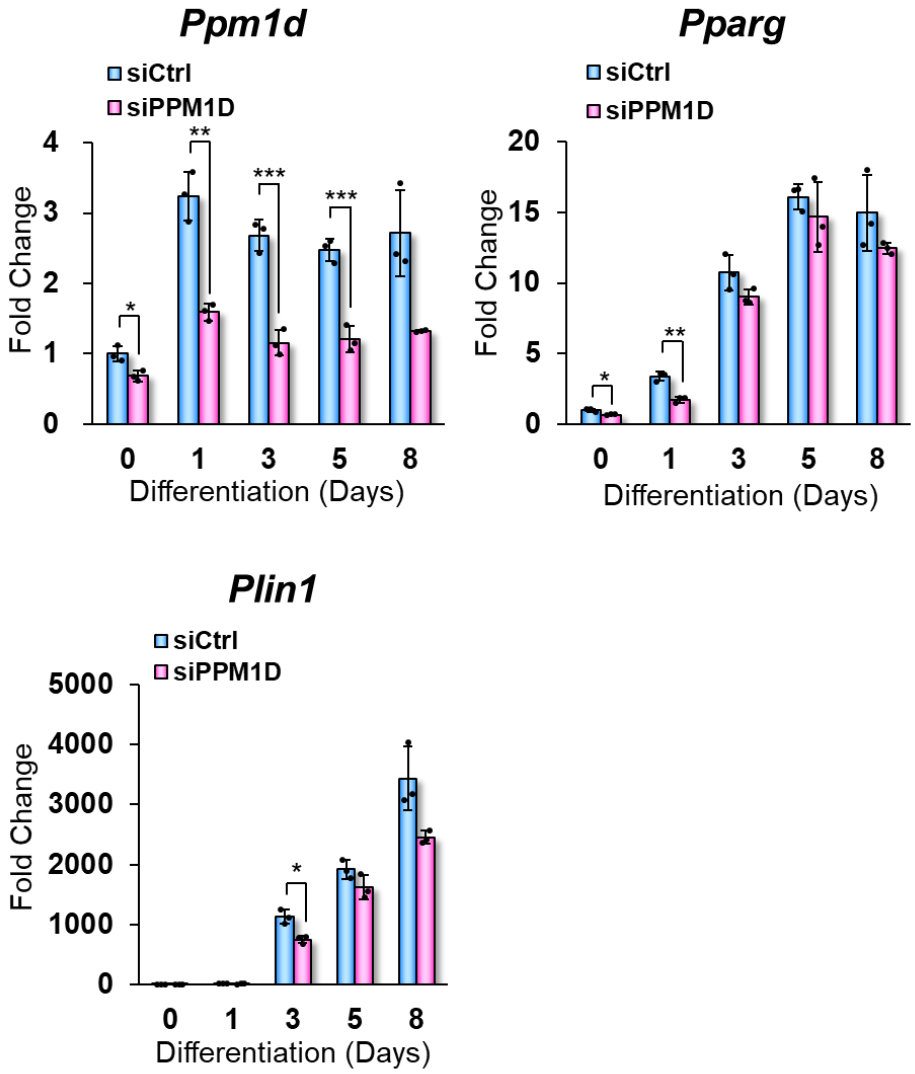

Figure 2-1. Effect of PPM1D knockdown on *Pparg* and *Plin1* expression levels.

3T3-L1 cells were transfected with Control siRNA (siCtrl) or mouse PPM1D siRNA (siPPM1D) and seeded. After 48 h, the cells were cultured in differentiation medium. The mRNA expression levels of *Ppm1d*, *Pparg*, and *Plin1* were analyzed using qPCR in 3T3-L1 cells on day 0, 1, 3, 5, and 8 of differentiation induction. The data was normalized by actin mRNA expression and expressed as fold change. Values are presented as the mean ± S.D. of three independent samples. Significance was analyzed by using Student's *t*-test. * $p < 0.05$, ** $p < 0.01$, *** $p < 0.001$.

2.4.2. Time-dependent analysis of PPM1D-inhibition in lipid droplet formation

To elucidate the function of PPM1D at each differentiation stage of white adipocyte differentiation, the PPM1D inhibitor SL-176 was used to specifically inhibit PPM1D during the differentiation period (**Figure 2-2A**). To analyze the effect on lipid droplet formation, the amount of lipid droplets on day 8 of differentiation was quantified using Oil Red O staining. As a result, the condition where SL-176 was added from day 0 to day 8 of differentiation (All) showed a 30% reduction in the amount of lipid droplets compared to Ctrl (**Figure 2-2B, C**). In the conditions where SL-176 was added from day 0 to day 3 (Early), from day 3 to day 6 (Middle), and from day 3 to day 8 (Middle-Late), the amount of lipid droplets decreased to 80% of the Ctrl, and in the condition where SL-176 was added from day 0 to day 5 (Early-Middle), it decreased to 60%. On the other hand, no change in lipid droplet amount was observed in the condition where SL-176 was added from day 5 to day 8 (Late).

As a result of quantifying the lipid droplet size on the 8 days of differentiation, the average lipid droplet size (LD size) in the condition where SL-176 was added from day 0 to day 8 (All) decreased to 1.30 μm, compared to the average value of 2.6 μm in the Ctrl (**Figure 2-3, Table 2-1**). In the conditions where SL-176 was added from day 0 to day 3, from day 3 to day 6, and from day 0 to day 5, the lipid droplet sizes decreased to 1.76 μm, 1.73 μm, and 1.33 μm, respectively. In the conditions where SL-176 was added from day 5 to day 8 and from day 3 to day 8, the lipid droplet sizes slightly decreased to 2.33 μm and 1.91 μm, respectively.

Inhibition of PPM1D during the early stages of white adipocyte differentiation significantly reduces both the amount and size of lipid droplets, whereas inhibition of PPM1D during the later stages does not affect the amount of lipid droplets but does reduce their size. These findings demonstrate that PPM1D regulates lipid droplet formation through different pathways in the early and late stages of white adipocyte differentiation.

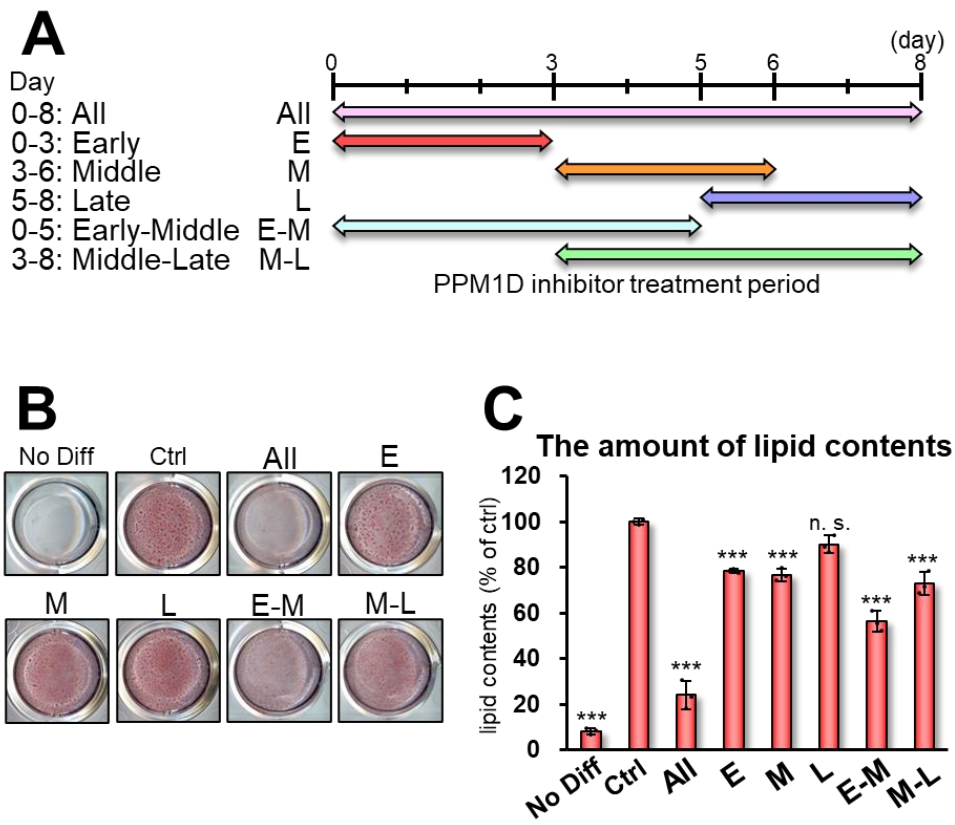

Figure 2-2. Effect on lipid contents by the differentiation stage-dependent PPM1D inhibition [30].

(A) Experimental design. (B) Oil red O-stained phase-contrast images of 3T3-L1 adipocytes differentiation day 8. 3T3-L1 cells were cultured in differentiation medium with the addition of SL-176 (15 μM) on the indicated days. (C) Absorbance of Oil red O extract was measured at 490 nm. Data are presented as the mean ± S.D. values and were obtained from three independent samples in each condition. Significance was analyzed by using one-way ANOVA with a post hoc Tukey's multiple-comparison test. *** $p < 0.001$, n. s., not statistically significant compared with the Ctrl group.

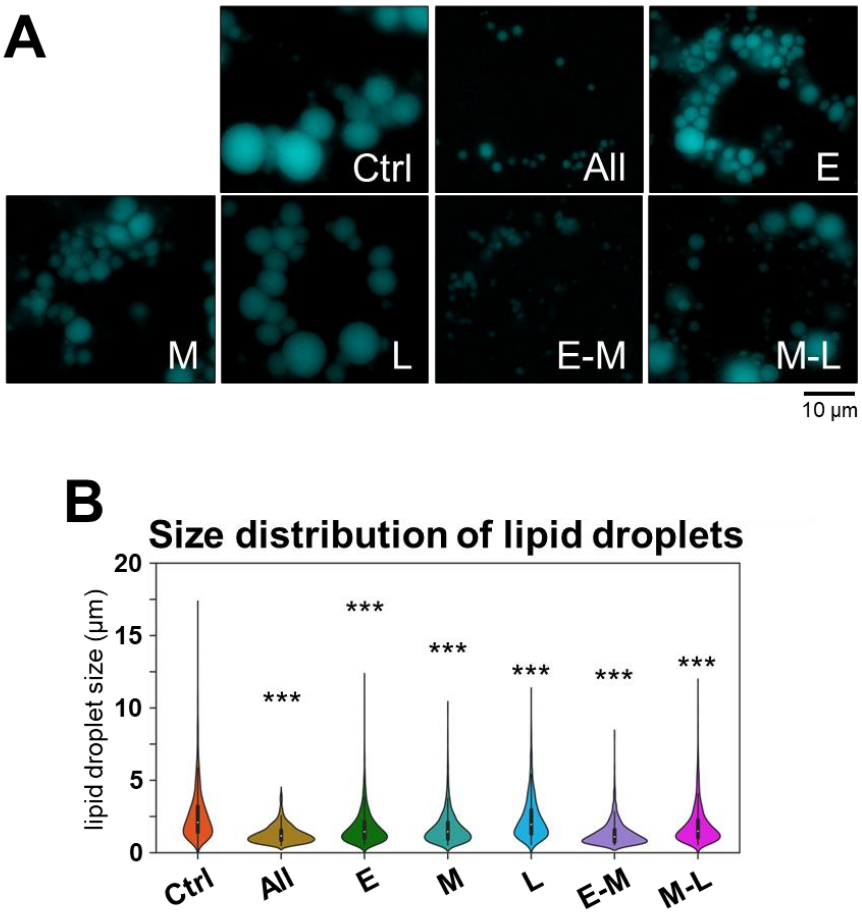

Figure 2-3. Effect on lipid droplet size by the time-dependent PPM1D inhibition [30].

(A) Lipid droplet imaging of 3T3-L1 adipocytes differentiation day 8 stained by MDH. 3T3-L1 cells were cultured in differentiation medium with the addition of SL-176 (15 μM) on the indicated days. MDH, Ex 360/40 nm, Em 460/50 nm. Scale bar: 10 μm. (B) Violin plot of size distribution of lipid droplets of 3T3-L1 adipocytes. Data were obtained from three independent experiments of 3T3-L1 cells. Significance was analyzed by using Wilcoxon Rank Sum Test. *** $p < 0.001$, compared with the Ctrl group.

Table 2-1. Average size of lipid droplets (LDs) in 3T3-L1 adipocytes treated with SL-176 [30].

	Average size[1]	Size distribution of LDs (%)[2]				
	[μm]	0-2 μm	2-4 μm	4-6 μm	6-8 μm	> 8 μm
Ctrl	2.60 ± 0.03	46.6	37.7	10.7	3.1	1.9
Day 0–8	1.30 ± 0.02	88.2	11.4	0.3	0.0	0.0
Day 0–3	1.76 ± 0.02	71.9	23.2	3.7	0.3	0.3
Day 3–6	1.73 ± 0.02	72.7	22.9	3.4	0.2	0.2
Day 5–8	2.33 ± 0.03	52.8	34.7	9.5	0.6	0.6
Day 0–5	1.33 ± 0.02	85.0	13.4	1.5	0.1	0.1
Day 3–8	1.91 ± 0.02	68.3	24.4	5.4	0.5	0.5

[1] Average size of LD. Data are presented as the mean ± S.E. of values obtained via three independent samples in each condition. Significance was analyzed by using Wilcoxon Rank Sum Test and shown in Figure 2-3B. [2] LD size distribution in 3T3-L1 cells treated with SL-176. LD diameters were calculated using ImageJ software.

2.4.3. Time-dependent analysis of adipogenic transcription factor expression under stage-specific PPM1D inhibition

We analyzed the mRNA expression levels of transcription factors that regulate adipocyte differentiation by adding SL-176 at differentiation stage-specific time points to inhibit PPM1D, using RT-qPCR. The results showed that in the conditions where SL-176 was added from day 0 to day 3 (Early) and from day 0 to day 5 (Early-Middle), the mRNA expression levels of PPARγ and C/EBPα were significantly reduced compared to the Ctrl (**Figure 2-4**). On the other hand, in the conditions where SL-176 was added from day 3 to day 6 (Middle) and from day 3 to day 8 (Middle-Late), the mRNA expression level of PPARγ was reduced compared to the Ctrl up to day 5, but by day 8, it was at a similar level to the Ctrl. The mRNA expression level of C/EBPα was also decreased compared to the Ctrl. In the condition where SL-176 was added from day 5 to day 8 (Late), the mRNA expression level of PPARγ was similar to that of the Ctrl. However, the mRNA expression level of C/EBPα was reduced compared to the Ctrl.

It was found that the inhibition of PPM1D during the early stages of white adipocyte differentiation suppresses the expression of transcription factors that regulate adipocyte differentiation. Additionally, PPM1D inhibition during the middle and late stages of differentiation was shown to slightly suppress the expression of these transcription factors.

These results suggest that the inhibition of PPM1D during the early stages of white adipocyte differentiation suppressed the induction of transcription factors that regulate adipocyte differentiation, leading to a reduction in the amount and size of lipid droplets due to inhibited lipid droplet formation. In contrast, during the middle stages of differentiation, the inhibition of PPM1D resulted in a smaller suppression of the induction of these transcription factors compared to early-stage inhibition, yet there was still a reduction in lipid droplet amount and size. These findings suggest that PPM1D controls the induction of transcription factors that regulate adipocyte differentiation in the early stages, whereas in

the middle stages, it regulates lipid droplet formation independently of adipocyte differentiation.

2.4.4. Effects of PPM1D inhibition on lipid droplets in mature white adipocytes

To clarify the differentiation-independent function of PPM1D in lipid droplet formation, I inhibited PPM1D in mature white adipocytes. After inducing differentiation of 3T3-L1 cells into white adipocytes, SL-176 was added and the cells were treated with SL-176 for 7 days and quantified lipid droplet size. The average size for the Ctrl was 5.47 μm, while the average size in the SL-176-treated group was 2.50 μm (**Figure 2-5A, B, Table 2-2**). Interestingly, inhibition of PPM1D resulted in a significant decrease in lipid droplet size. However, when quantifying lipid droplet quantity, there was no change between the Ctrl and SL-176-treated groups (**Figure 2-5C**).

Inhibition of PPM1D in mature white adipocytes resulted in a significant decrease in lipid droplet size, while the amount of lipid droplets remained unchanged. These findings suggest that PPM1D positively regulates the size of lipid droplets independently of differentiation.

2.4.5. Lipolysis of lipid droplets produced upon PPM1D inhibition

To elucidate the effect of smaller-sized lipid droplets formed by the inhibition of PPM1D in mature white adipocytes on lipolysis, a lipolytic stimulus was applied. Observation of the lipid droplets revealed a reduction in droplet size in both the Ctrl and SL-176 conditions following the lipolytic stimulus (**Figure 2-6A**). Quantification of Free Glycerol and Free Fatty Acid, which are produced during lipolysis, showed that the amount of Free Fatty Acid after 4 hours of lipolytic stimulation was reduced in the SL-176 condition compared to the Ctrl (**Figure 2-6B**).

These findings suggest that the smaller-sized lipid droplets formed by the inhibition of PPM1D exhibit slight resistance to lipolysis.

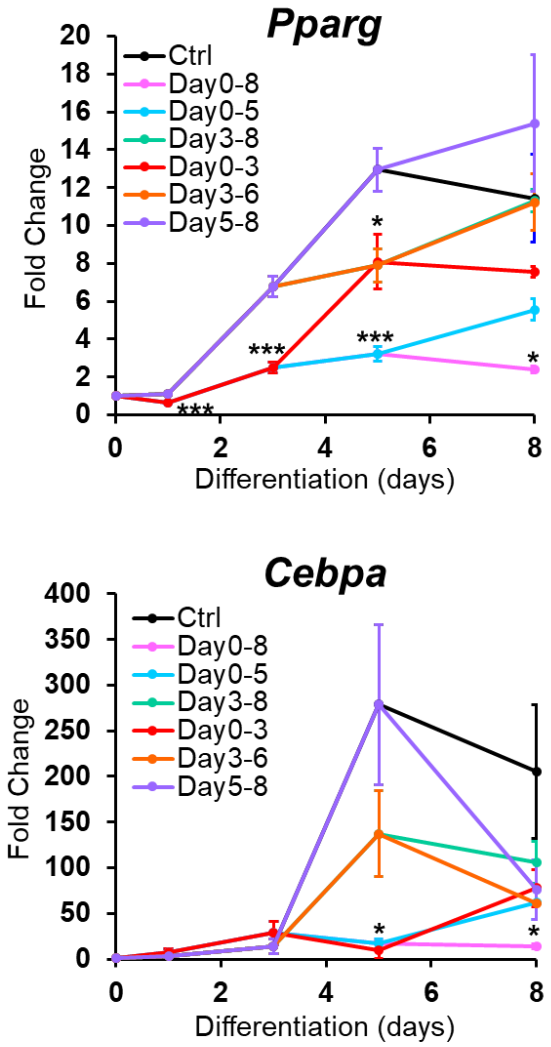

Figure 2-4. Effect of the time-dependent PPM1D inhibition on *Pparg* and *Cebpa* expression levels [30].

3T3-L1 cells were cultured in differentiation medium with the addition of SL-176 (15 μM) on the indicated days. The mRNA expression levels of *Pparg* and *Cebpa* were analyzed using qPCR in 3T3-L1 cells on day 0, 1, 3, 5, and 8 of differentiation induction. The data was normalized by actin mRNA expression and expressed as fold change. Values are presented as the mean ± S.E.M. of three independent experiments. Significance was analyzed by using one-way ANOVA with a post hoc Tukey's multiple-comparison test. * $p < 0.05$, *** $p < 0.001$, compared with the Ctrl group.

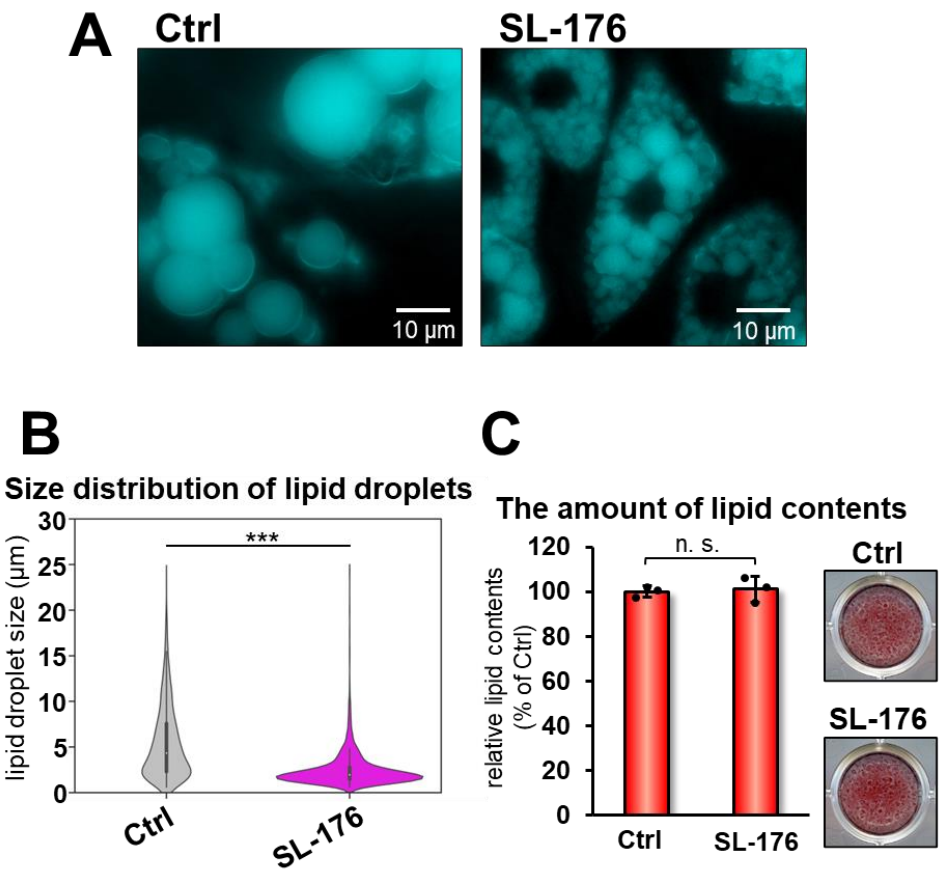

Figure 2-5. Effect on lipid droplets of mature white adipocytes by inhibition of PPM1D [30].

(A) Lipid droplet imaging of PPM1D-inhibited 3T3-L1 adipocytes stained by MDH. 3T3-L1 cells were differentiated into adipocytes for 8 days followed by treatment of SL-176 (15 μM) for 7 days. MDH, Ex 360/40 nm, Em 460/50 nm. Scale bar: 10 μm. (B) Violin plot of size distribution of lipid droplets of 3T3-L1 adipocytes. Data were obtained from three independent experiments of 3T3-L1 cells. Significance was analyzed by using Wilcoxon Rank Sum Test. *** $p < 0.001$. (C) Oil red O-stained phase-contrast images and absorbance of Oil red O extract was measured at 490 nm. Data are presented as the mean ± S.D. values and were obtained from three independent samples. n. s., not statistically significant by Student's *t*-test.

Table 2-2. The average size of lipid droplet (LD) in mature 3T3-L1 cells treated with SL-176 [30].

	Average size[1]	Size distribution of LDs (%)[2]				
	[μm]	0-2 μm	2-4 μm	4-6 μm	6-8 μm	> 8 μm
Ctrl	5.47 ± 0.10	19.4	27.2	17.8	13.1	22.5
SL-176	2.50 ± 0.05	53.7	33.1	8.4	2.7	2.1

[1] Values are presented as the mean ± S.E. of values obtained via three independent samples in each condition. [2] Significance was analyzed by using Wilcoxon Rank Sum Test and shown in Figure 2-5B. LD size distribution in 3T3-L1 cells treated with SL-176. LD diameters were calculated using ImageJ software.

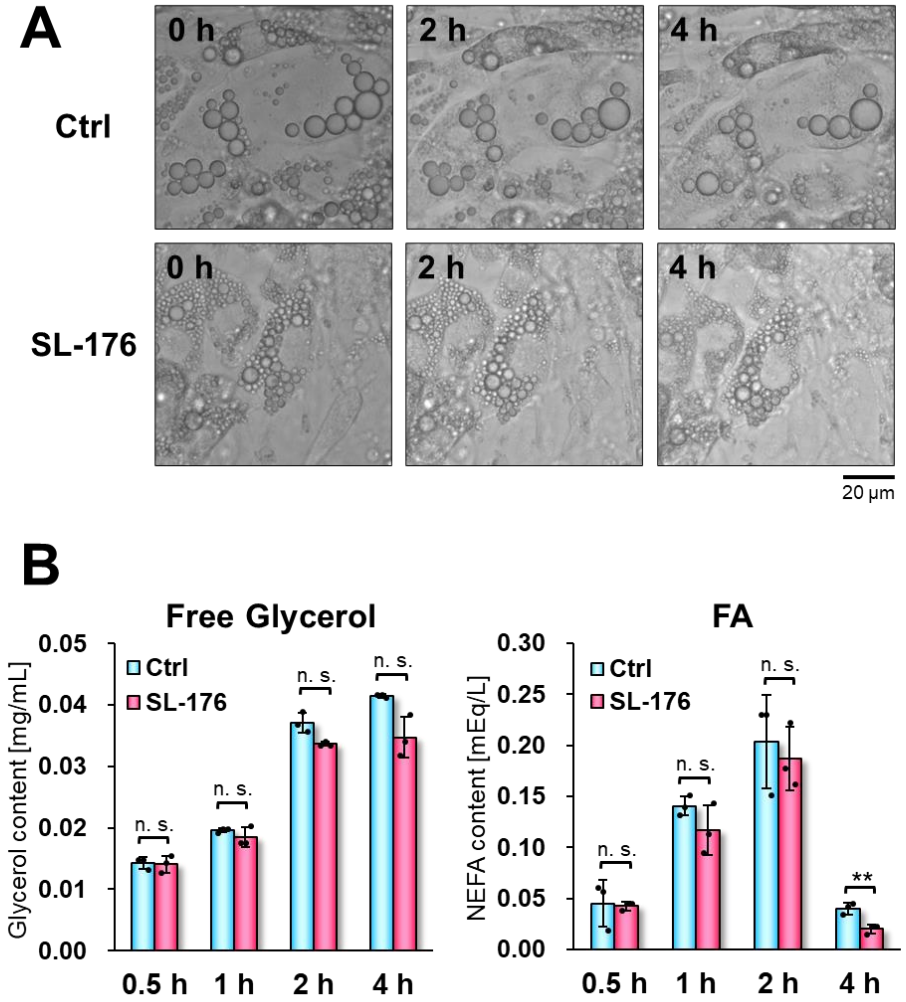

Figure 2-6. Effect of lipolysis on PPM1D-inhibited adipocytes [30].

(A) Cell images of 3T3-L1 adipocytes differentiation day 15 during lipolysis. 3T3-L1 cells were differentiated into adipocytes for 8 days followed by treatment of SL-176 (15 μM) for 7 days, then incubated with lipolysis medium for 2 and 4 h. Scale bar: 20 μm. (B) The amount of free glycerol and FA of 3T3-L1 adipocytes. Cells were differentiated into adipocytes for 8 days followed by treatment of SL-176 (15 μM) for 7 days, then incubated with lipolysis medium for 1 h. After incubation, changed with measurement medium and incubated for the indicated time. Data were obtained from three independent experiments of 3T3-L1 cells. Data are presented as the mean ± S.D. values and were obtained from three independent samples. Significance was analyzed by using Student's *t*-test. * $p < 0.05$; n.s., not statistically significant.

2.4.6. Function of PPM1D via dephosphorylation of perilipin 1 on lipid droplet formation

To elucidate the mechanism by which PPM1D regulates lipid droplet formation, the function of PPM1D concerning perilipin 1, which positively regulates lipid droplet formation, was analyzed. First, to determine the effect of PPM1D inhibition on the expression level of perilipin 1 in mature white adipocytes, SL-176 was added to 3T3-L1 adipocytes for 7 days, and RT-qPCR was used to analyze perilipin 1 mRNA expression. The results showed no change in perilipin 1 mRNA expression (**Figure 2-7A**). Lipid droplet size and lipolysis are controlled by the phosphorylation level of perilipin 1. Therefore, an analysis of the phosphatase activity of PPM1D on phosphorylated peptides of perilipin 1 revealed that PPM1D exhibited phosphatase activity against the Ser511 phosphorylated peptide of perilipin 1 (**Figure 2-7B**). In contrast, PPM1D did not show phosphatase activity against the Ser492 and Ser517 phosphorylated peptides of perilipin 1. These findings suggest that PPM1D specifically targets perilipin 1 at Ser511.

To further elucidate the function of phosphorylation at Ser511 of perilipin 1 in lipid droplet formation, phosphorylation mutant S511D and non-phosphorylation mutant S511A were overexpressed in 3T3-L1 cells, and the lipid droplet size was quantified. The results showed that the average lipid droplet size for the perilipin 1 S511A mutant was 2.61 μm, whereas for the S511D mutant, the average size decreased to 2.27 μm (**Figure 2-7C, D, Table 2-3**).

The overexpression of the phosphorylated mutant of perilipin 1 Ser511 resulted in a significant decrease in lipid droplet size, demonstrating that phosphorylation at Ser511 negatively regulates lipid droplet size. From these findings, it is suggested that PPM1D positively regulates lipid droplet size by dephosphorylating perilipin 1 at Ser511.

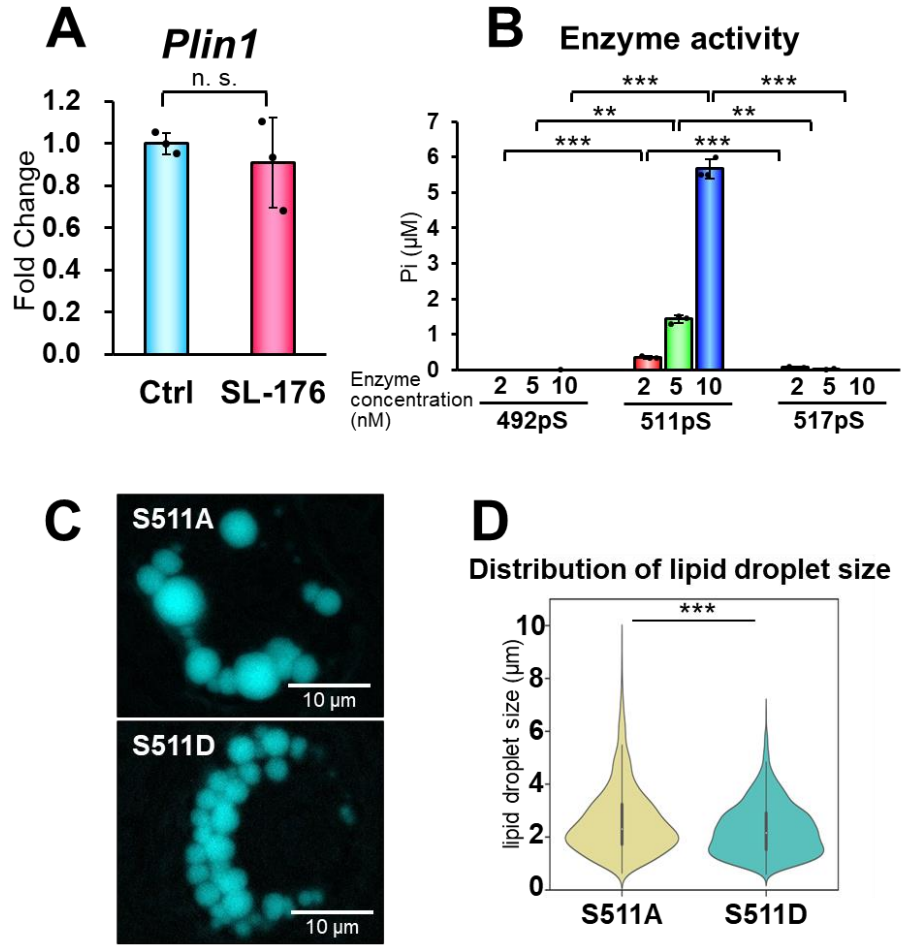

Figure 2-7. PPM1D regulates lipid droplet formation via dephosphorylation of perilipin 1 Ser511 [30].

(A) The mRNA expression level of *Plin1* analyzed using qPCR. 3T3-L1 cells were differentiated into adipocytes for 8 days followed by treatment of SL-176 (15 μM) for 7 days. The data was normalized by actin mRNA expression and expressed as fold change. Data are presented as the mean ± S.D. values and were obtained from three independent samples. n. s., not statistically significant by Student's *t*-test. (B) Phosphatase activity of His-mouse PPM1D on perilipin 1 phosphorylated peptides. Data presents the mean ± S.D. values of three independent experiments. Significance was analyzed by using Student's *t*-test. ** $p < 0.01$, *** $p < 0.001$. (C) Lipid droplet imaging of 3T3-L1 adipocytes transfected with perilipin 1 mutants stained by MDH. 3T3-L1 cells were transfected with perilipin 1 (S511A) or perilipin 1 (S511D) on day 3 of differentiation. After 3 days of transfection, 3T3-L1 cells were stained with MDH. MDH, Ex 360/40 nm, Em 460/50 nm. Scale bar: 10 μm. (D) Violin plot of size distribution of lipid droplets of 3T3-L1 adipocytes. Data were obtained from three independent experiments of 3T3-L1 cells. Significance was analyzed by using Wilcoxon Rank Sum Test. *** $p < 0.001$.

Table 2-3. Size distribution of LDs overexpressing perilipin 1 mutants [30].

	Average size[1]	Size distribution of LDs (%)[2]			
	[μm]	0-2 μm	2-4 μm	4-6 μm	> 6 μm
S511A	2.61 ± 0.03	38.1	49.0	10.2	2.6
S511D	2.27 ± 0.02	44.5	49.7	5.7	0.2

[1] Values are presented as the mean ± S.E. of values obtained via three independent samples in each condition. Data were obtained from 3 independent experiments of 3T3-L1 cells transfected with perilipin 1 S511A or S511D. [2] Significance was analyzed by using Wilcoxon Rank Sum Test and shown in Figure 2-7D. LD size distribution in 3T3-L1 cells overexpressing perilipin 1 S511A or S511D mutants. LD diameters were calculated using ImageJ software.

2.4.7. Effects of PPM1D inhibition on mature white adipocytes

Beige adipocytes are defined by the formation of multilocular lipid droplets, an increase in mitochondrial content, and the expression of beige adipocyte differentiation markers [31]. The accumulation of smaller lipid droplets in the cytoplasm of mature white adipocytes following PPM1D inhibition resembled the multilocular lipid droplets of beige adipocytes, suggesting that PPM1D-inhibited mature white adipocytes might be differentiating into beige adipocytes. Therefore, mitochondrial imaging was performed on PPM1D-inhibited mature white adipocytes, and interestingly, PPM1D inhibition led to a significant increase in mitochondrial activity (**Figure 2-8A**). However, RT-qPCR analysis of the mRNA expression levels of the beige adipocyte differentiation markers UCP1 and CIDEA showed no change (**Figure 2-8B**).

PPM1D-inhibited mature white adipocytes form multilocular lipid droplets and exhibit increased mitochondrial activity, while the expression levels of beige adipocyte differentiation markers remain unchanged. These results suggest that while PPM1D-inhibited white adipocytes display characteristics of beige adipocytes, they differentiate into a cell type distinct from typical beige adipocytes.

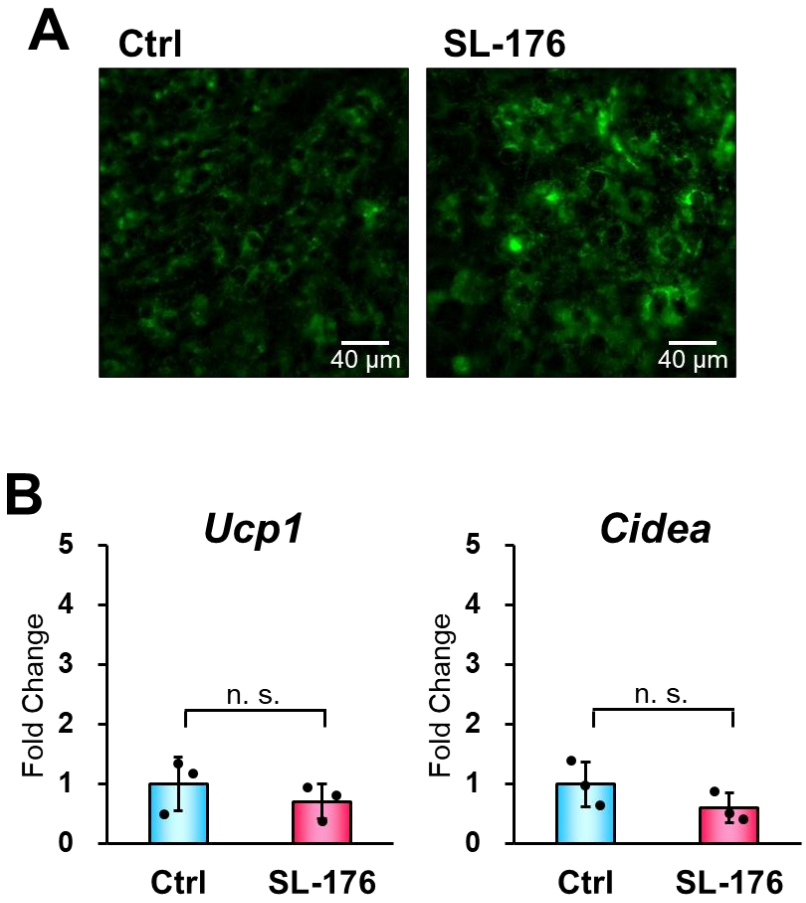

Figure 2-8. Effect of PPM1D inhibition on mitochondria and expression levels of beige adipocytes markers.

(A) Mitochondria imaging of PPM1D-inhibited 3T3-L1 adipocytes stained by MitoTracker Red CM-H_2Xros. 3T3-L1 cells were differentiated into adipocytes for 8 days followed by treatment of SL-176 (15 μM) for 7 days. MitoTracker Red CM-H_2Xros, Ex 540/25 nm, Em 605/55 nm. Scale bar: 40 μm. (B) The mRNA expression levels of *Ucp1* and *Cidea* analyzed using qPCR. The data was normalized by actin mRNA expression and expressed as fold change. Values are presented as the mean ± S.D. of three independent samples. n. s., not statistically significant by Student's *t*-test.

2.5. Discussion

In this study, PPM1D knockdown during white adipocyte differentiation decreased the mRNA expression of PPARγ, a transcription factor that regulates adipocyte differentiation, and its downstream gene perilipin 1 in the early stages of differentiation. This result suggests that PPM1D controls adipocyte differentiation in the early phase of differentiation. Our laboratory has reported that the addition of the PPM1D inhibitor SL-176 during white adipocyte differentiation induction suppresses the expression of PPARγ and perilipin 1 [28]. It has been revealed that PPM1D is involved in the induction of expression of adipocyte differentiation markers. It is suggested that PPM1D regulates the expression of PPARγ by controlling the transcriptional activity of upstream proteins of PPARγ, subsequently modulating the expression of its downstream gene, perilipin 1.

It was revealed that PPM1D regulates lipid droplet formation through two pathways: differentiation-dependent pathway and differentiation-independent pathway in white adipocyte differentiation. In the differentiation-independent lipid droplet formation, PPM1D targets perilipin 1. When the PPM1D inhibitor SL-176 is added after differentiation induction, a decrease in lipid droplet size is observed without a change in lipid droplet amount, suggesting that PPM1D is involved in lipid droplet fusion. Lipid droplet fusion is a mechanism whereby two lipid droplets of different sizes come into contact and merge to form a larger lipid droplet, and it is known as one of the mechanisms that contribute to lipid droplet hypertrophy. It has been reported that during this lipid droplet fusion process, perilipin 1 promotes the fusion of lipid droplets via Fsp27 [32]. If perilipin 1 acts as a scaffolding protein and the proteins that interact with perilipin 1 change with variations in its phosphorylation levels, then the inhibition of PPM1D could lead to an increase in the phosphorylation level of perilipin 1. This change might alter its interactions with proteins, including Fsp27, potentially resulting in the suppression of lipid droplet fusion.

The multilocular lipid droplets formed by the inhibition of PPM1D in mature white adipocytes

have been suggested to exhibit resistance to lipolysis. It has been reported that smaller lipid droplets are more prone to lipolysis compared to larger lipid droplets [14]. On the other hand, there are reports suggesting that lipolysis targets larger lipid droplets and induces the formation of smaller lipid droplets [13], indicating that the relationship between lipid droplet size and degradation has not yet been clarified. In this study, since the small multilocular lipid droplets showed resistance to lipolysis, suggesting that the difference in size is involved in the lipolytic activity. Additionally, the dephosphorylation of perilipin 1 at Ser511 by PPM1D may also play a role in the regulation of lipolytic activity. Perilipin 1 at Ser492 and Ser517 is phosphorylated by PKA, which induces lipolysis. The phosphorylation of perilipin 1 at Ser517 inhibits the interaction between perilipin 1 and CGI-58, allowing CGI-58 to interact with ATGL, thereby triggering its activation [33]. Increased the negative charge at the C-terminal of perilipin 1 due to phosphorylation by PKA is suggested to be involved in the promotion of lipolysis. The dephosphorylation of perilipin 1 at Ser511 by PPM1D may be involved in the regulation of the negative charge at the C-terminal of perilipin 1, potentially controlling lipolysis.

In mature white adipocytes, the inhibition of PPM1D has been shown to increase mitochondrial activity. The increased mitochondrial activity suggests an enhancement of mitochondrial function and an increase in mitochondrial quantity. In adipocytes, peroxisome proliferator-activated receptor gamma coactivator 1-alpha (PGC-1α) is known to interact with PPARγ, thereby increasing the transcriptional activity of PPARγ and enhancing mitochondrial biogenesis and gene expression [34]. PPM1D may be involved in mitochondrial function through genes that regulate mitochondrial biogenesis. This study has revealed that the inhibition of PPM1D during the adipocyte differentiation process leads to a decrease in PPARγ mRNA expression. However, in mature white adipocytes, it may interact with PPARγ through pathways that differ from those during differentiation. Additionally, lipid droplets and mitochondria are in contact, and the fatty acids released from lipid droplets are utilized for energy production in mitochondria [35]. PPM1D inhibition in mature white adipocytes results in the

formation of smaller lipid droplets, while the total lipid contents remain unchanged, thus increasing the surface area of the lipid droplets. Mitochondrial activity may increase due to the increased contact surface with mitochondria and increased uptake of fatty acids released by lipid droplets.

It was suggested that inhibition of PPM1D in mature white adipocytes leads to differentiation into a novel subtype characterized by increased mitochondrial content but without elevated expression of beige adipocyte differentiation markers. While this novel subtype closely resembles beige adipocytes in morphology, its gene expression profile differs, suggesting that it may possess distinct functions compared to typical beige adipocytes. These findings imply that PPM1D not only regulates the differentiation of white adipocytes but also controls the differentiation of beige adipocytes and their subtypes.

In summary, this study demonstrated that PPM1D regulates adipocyte differentiation and maturation (**Figure 2-9**), which may lead to the development of novel obesity therapies targeting PPM1D.

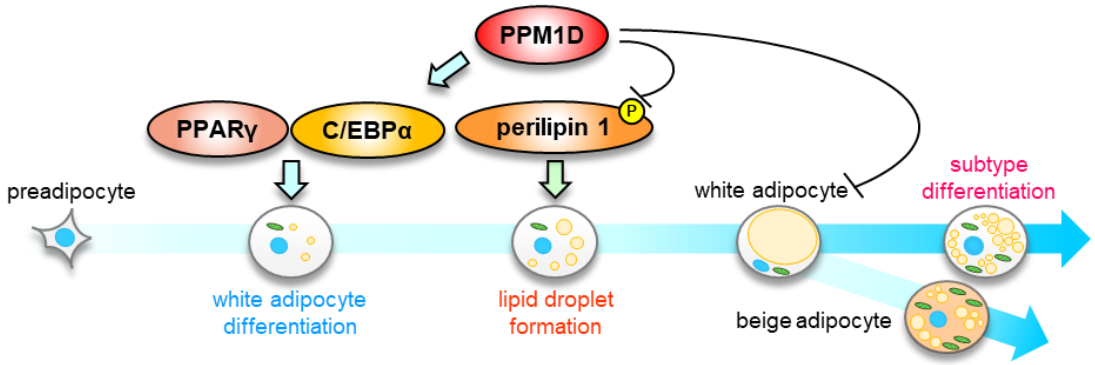

Figure 2-9. Model of the regulatory mechanism of adipocyte differentiation and maturation by PPM1D.

2.6. References

1. K. Frayn, Adipose tissue as a buffer for daily lipid flux, *Diabetologia*, **45**, 1201–1210 (2002). https://doi.org/10.1007/S00125-002-0873-Y/METRICS.
2. S. Galic, J. S. Oakhill, and G. R. Steinberg, Adipose tissue as an endocrine organ, *Mol. Cell. Endocrinol.*, **316**, 129–139 (2010). https://doi.org/10.1016/J.MCE.2009.08.018.
3. A. L. Ghaben and P. E. Scherer, Adipogenesis and metabolic health, *Nat. Rev. Mol. Cell Biol. 2018 204*, **20**, 242–258 (2019). https://doi.org/10.1038/s41580-018-0093-z.
4. M. Audano, S. Pedretti, D. Caruso, M. Crestani, E. De Fabiani, and N. Mitro, Regulatory mechanisms of the early phase of white adipocyte differentiation: an overview, *Cell. Mol. Life Sci. 2022 793*, **79**, 1–14 (2022). https://doi.org/10.1007/S00018-022-04169-6.
5. G. J. TODARO and H. GREEN, Quantitative studies of the growth of mouse embryo cells in culture and their development into established lines., *J. Cell Biol.*, **17**, 299–313 (1963). https://doi.org/10.1083/jcb.17.2.299.
6. Z. Wu, N. L. Bucher, and S. R. Farmer, Induction of peroxisome proliferator-activated receptor gamma during the conversion of 3T3 fibroblasts into adipocytes is mediated by C/EBPbeta, C/EBPdelta, and glucocorticoids., *Mol. Cell. Biol.*, **16**, 4128–4136 (1996). https://doi.org/10.1128/mcb.16.8.4128.
7. W. C. Yeh, Z. Cao, M. Classon, and S. L. McKnight, Cascade regulation of terminal adipocyte differentiation by three members of the C/EBP family of leucine zipper proteins, *Genes Dev.*, **9**, 168–181 (1995). https://doi.org/10.1101/gad.9.2.168.
8. E. D. Rosen, C. H. Hsu, X. Wang, S. Sakai, M. W. Freeman, F. J. Gonzalez, and B. M. Spiegelman, C/EBPα induces adipogenesis through PPARγ: a unified pathway, *Genes Dev.*, **16**, 22 (2002). https://doi.org/10.1101/GAD.948702.
9. E. D. Rosen, The transcriptional basis of adipocyte development, *Prostaglandins, Leukot. Essent. Fat. Acids*, **73**, 31–34 (2005). https://doi.org/10.1016/J.PLEFA.2005.04.004.
10. T. Fujimoto and R. G. Parton, Not Just Fat: The Structure and Function of the Lipid Droplet, *Cold Spring Harb. Perspect. Biol.*, **3**, a004838 (2011). https://doi.org/10.1101/CSHPERSPECT.A004838.
11. A. L. S. Cruz, E. de A. Barreto, N. P. B. Fazolini, J. P. B. Viola, and P. T. Bozza, Lipid droplets: platforms with multiple functions in cancer hallmarks, *Cell Death Dis. 2020 112*, **11**, 1–16 (2020). https://doi.org/10.1038/s41419-020-2297-3.
12. A. S. Greenberg, R. A. Coleman, F. B. Kraemer, J. L. McManaman, M. S. Obin, V. Puri, Q. W. Yan, H. Miyoshi, and D. G. Mashek, The role of lipid droplets in metabolic disease in rodents and humans, *J. Clin. Invest.*, **121**, 2102–2110 (2011). https://doi.org/10.1172/JCI46069.
13. M. B. Schott, S. G. Weller, R. J. Schulze, E. W. Krueger, K. Drizyte-Miller, C. A. Casey, and M. A. McNiven, Lipid droplet size directs lipolysis and lipophagy catabolism in hepatocytes, *J.*

Cell Biol., **218**, 3320–3335 (2019). https://doi.org/10.1083/JCB.201803153.

14. M. Paar, C. Jüngst, N. A. Steiner, C. Magnes, F. Sinner, D. Kolb, A. Lass, R. Zimmermann, A. Zumbusch, S. D. Kohlwein, and H. Wolinski, Remodeling of lipid droplets during lipolysis and growth in adipocytes, *J. Biol. Chem.*, **287**, 11164–11173 (2012). https://doi.org/https://dx.doi.org/10.1074%2Fjbc.M111.316794.
15. A. S. Greenberg, J. J. Egan, S. A. Wek, N. B. Garty, E. J. Blanchette-Mackie, and C. Londos, Perilipin, a major hormonally regulated adipocyte-specific phosphoprotein associated with the periphery of lipid storage droplets, *J. Biol. Chem.*, **266**, 11341–11346 (1991). https://doi.org/10.1016/S0021-9258(18)99168-4.
16. A. Girousse and D. Langin, Adipocyte lipases and lipid droplet-associated proteins: Insight from transgenic mouse models, *International Journal of Obesity*, **36**. Nature Publishing Group, 581–594 (2012). https://doi.org/10.1038/ijo.2011.113.
17. G. M. Clifford, D. K. t. McCormick, C. Londos, R. G. Vernon, and S. J. Yeaman, Dephosphorylation of perilipin by protein phosphatases present in rat adipocytes, *FEBS Lett.*, **435**, 125–129 (1998). https://doi.org/10.1016/S0014-5793(98)01052-7.
18. W. Wang and P. Seale, Control of brown and beige fat development, *Nature Reviews Molecular Cell Biology*, **17**. Nature Publishing Group, 691–702 (2016). https://doi.org/10.1038/nrm.2016.96.
19. A. Fedorenko, P. V. Lishko, and Y. Kirichok, Mechanism of Fatty-Acid-Dependent UCP1 Uncoupling in Brown Fat Mitochondria, *Cell*, **151**, 400–413 (2012). https://doi.org/10.1016/J.CELL.2012.09.010.
20. S. Kajimura, B. M. Spiegelman, and P. Seale, Brown and beige fat: Physiological roles beyond heat generation, *Cell Metabolism*, **22**. Cell Press, 546–559 (2015). https://doi.org/10.1016/j.cmet.2015.09.007.
21. B. Maniyadath, Q. Zhang, R. K. Gupta, and S. Mandrup, Adipose tissue at single-cell resolution, *Cell Metab.*, **35**, 386–413 (2023). https://doi.org/10.1016/J.CMET.2023.02.002.
22. M. Fiscella, H. Zhang, S. Fan, K. Sakaguchi, S. Shen, W. E. Mercer, G. F. Vande Woude, P. M. O'Connor, and E. Appella, Wip1, a novel human protein phosphatase that is induced in response to ionizing radiation in a p53-dependent manner, *Proc. Natl. Acad. Sci. U. S. A.*, **94**, 6048–6053 (1997). https://doi.org/10.1073/pnas.94.12.6048.
23. X. Lu, B. Nannenga, and L. A. Donehower, PPM1D dephosphorylates Chk1 and p53 and abrogates cell cycle checkpoints, *Genes Dev.*, **19**, 1162–1174 (2005). https://doi.org/10.1101/gad.1291305.
24. S. Shreeram, O. N. Demidov, W. K. Hee, H. Yamaguchi, N. Onishi, C. Kek, O. N. Timofeev, C. Dudgeon, A. J. Fornace, C. W. Anderson, Y. Minami, E. Appella, and D. V. Bulavin, Wip1 Phosphatase Modulates ATM-Dependent Signaling Pathways, *Mol. Cell*, **23**, 757–764 (2006).

https://doi.org/10.1016/j.molcel.2006.07.010.

25. X. Le Guezennec, A. Brichkina, Y. F. Huang, E. Kostromina, W. Han, and D. V. Bulavin, Wip1-dependent regulation of autophagy, obesity, and atherosclerosis, *Cell Metab.*, **16**, 68–80 (2012). https://doi.org/10.1016/j.cmet.2012.06.003.
26. D. Li, L. Zhang, L. Xu, L. Liu, Y. He, Y. Zhang, X. Huang, T. Zhao, L. Wu, Y. Zhao, K. Wu, H. Li, X. Yu, T. Zhao, S. Gong, M. Fan, and L. Zhu, WIP1 phosphatase is a critical regulator of adipogenesis through dephosphorylating PPARγ serine 112, *Cell. Mol. Life Sci.*, **74**, 2067–2079 (2017). https://doi.org/10.1007/s00018-016-2450-4.
27. S. Ogasawara, Y. Kiyota, Y. Chuman, A. Kowata, F. Yoshimura, K. Tanino, R. Kamada, and K. Sakaguchi, Novel inhibitors targeting PPM1D phosphatase potently suppress cancer cell proliferation, *Bioorganic Med. Chem.*, **23**, 6246–6249 (2015). https://doi.org/10.1016/j.bmc.2015.08.042.
28. R. Kamada, N. Kimura, F. Yoshimura, K. Tanino, and K. Sakaguchi, Inhibition of lipid droplet formation by Ser/Thr protein phosphatase PPM1D inhibitor, SL-176, *PLoS One*, **14**, (2019). https://doi.org/10.1371/journal.pone.0212682.
29. R Core Team., R: a language and environment for statistical computing. [Online]. Available: https://www.gbif.org/tool/81287/r-a-language-and-environment-for-statistical-computing.
30. R. Kamada, S. Uno, N. Kimura, F. Yoshimura, K. Tanino, and K. Sakaguchi, Lipid Droplet Formation Is Regulated by Ser/Thr Phosphatase PPM1D via Dephosphorylation of Perilipin 1, *Int. J. Mol. Sci.*, **23**, 12046 (2022). https://doi.org/10.3390/IJMS231912046/S1.
31. M. Harms and P. Seale, Brown and beige fat: development, function and therapeutic potential, *Nat. Med.*, **19**, 1252–1263 (2013). https://doi.org/10.1038/nm.3361.
32. Z. Sun, J. Gong, H. Wu, W. Xu, L. Wu, D. Xu, J. Gao, J. W. Wu, H. Yang, M. Yang, and P. Li, Perilipin1 promotes unilocular lipid droplet formation through the activation of Fsp27 in adipocytes, *Nat. Commun.*, **4**, 1–15 (2013). https://doi.org/10.1038/ncomms2581.
33. J. G. Granneman, H. P. H. Moore, R. Krishnamoorthy, and M. Rathod, Perilipin controls lipolysis by regulating the interactions of AB-hydrolase containing 5 (Abhd5) and adipose triglyceride lipase (Atgl), *J. Biol. Chem.*, **284**, 34538–34544 (2009). https://doi.org/10.1074/JBC.M109.068478/ATTACHMENT/63EE8D96-C3B0-4C7B-AC5E-F53A37261FCF/MMC1.ZIP.
34. T. Inagaki, J. Sakai, and S. Kajimura, Transcriptional and epigenetic control of brown and beige adipose cell fate and function, *Nat. Rev. Mol. Cell Biol.*, **17**, 480–495 (2016). https://doi.org/10.1038/nrm.2016.62.
35. J. A. Olzmann and P. Carvalho, Dynamics and functions of lipid droplets, *Nature Reviews Molecular Cell Biology*, **20**. Nature Publishing Group, 137–155 (2019). https://doi.org/10.1038/s41580-018-0085-z.

3. Development of cell recognition method using triazapentalene derivatives with deep learning

3.1. Abstract

Adipocytes play a vital role in energy homeostasis and are implicated in diseases such as obesity and metabolic disorders. Identifying and classifying adipocyte subtypes at the single-cell level is critical for understanding their functions and contributions to disease. Despite progress in fluorescent probes and image analysis, comprehensive methods for distinguishing adipocyte states and differentiation pathways remain limited.

This study introduces a novel method for single-cell-level identification of adipocytes using multiplex staining with newly designed 1,3a,6a-triazapentalene (TAP) derivatives, ab-TAP-4PH and TAP-2CY4E1, in combination with a deep learning model. ab-TAP-4PH fluoresces strongly in polar and acidic environments, while TAP-2CY4E1 exhibits intense fluorescence in hydrophobic regions. These unique properties allowed the selective staining of cellular organelles and lipid droplets, enabling multicolor imaging of cellular states. Cytotoxicity assays confirmed the high biocompatibility of both probes, showing minimal impact on cell proliferation even at high concentrations. Additionally, the probes were easily removed from cells via wash-out, preserving cell viability.

The method was validated using p53 wild-type (A549) and p53-deficient (H1299) lung cancer cells. Fluorescence images analyzed by a deep learning model successfully identified and distinguished these cell types with high accuracy. Co-culture experiments with varying A549:H1299 ratios achieved F1 scores exceeding 0.9 across all conditions, demonstrating the method's capability for precise single-cell identification within heterogeneous populations.

This approach was further applied to white adipocytes under PPM1D inhibition. The differentiation process was analyzed using TAP derivatives, revealing a novel adipocyte subtype characterized by smaller, multilocular lipid droplets and increased mitochondrial activity. Deep learning

models classified adipocytes into three states: state I (immature cells), state II (control adipocytes with large lipid droplets), and state III (PPM1D-inhibited adipocytes with multilocular lipid droplets). These classifications provided insights into the dynamic transitions between states during differentiation.

In summary, this study highlights the potential of multiplex staining with TAP derivatives combined with deep learning for high-resolution cellular analysis. This approach offers significant insights into adipocyte differentiation pathways and cellular heterogeneity, advancing research into obesity and metabolic disorders. Future developments, including additional TAP derivatives for nuclear staining, could further enhance single-cell-level identification and provide a more comprehensive understanding of cellular states.

3.2. Introduction

Adipocytes are essential for maintaining energy homeostasis and metabolism. They are classified into four types: white adipocytes, responsible for energy storage and release; brown and beige adipocytes, responsible for thermogenesis; and pink adipocytes involved in milk production [1, 2]. Furthermore, in recent years, multiple subtypes of these adipocytes with distinct gene expression profiles and function have been reported [3]. In white adipocytes, the emergence of a subtype characterized by the high expression of genes related to lipid uptake and transport, stress response, and immune response has been reported in mice fed high-fat diets [4], suggesting that this subtype could contribute to obesity. Adipocytes are associated with various diseases, including obesity, and identifying their differentiation, maturation, and subtypes at the single-cell level to elucidate their functions is crucial for the diagnosis of diseases and the development of therapeutic strategies.

Fluorescent probes are widely used in research on cell identification [5]. Fluorescent probes are effective tools for analyzing dynamic changes in live cells, as they enable simultaneous staining and detection of multiple probes with different wavelengths and chemical properties. Numerous reports have described fluorescent probes that specifically target certain organelles, such as organelle-specific probes [6, 7] and probes whose fluorescence changes in a pH-dependent manner within organelles [8, 9]. However, to analyze the diverse states of cells, it is important to develop probes that emit fluorescence extensively within the cells, enabling comprehensive visualization of overall state of the cells.

Organic small molecules are one of the important fluorescent probes due to their high selectivity and sensitivity, which allow for real-time analysis of cells, and their relatively straightforward usage [10]. 1,3a,6a-triazapentalene (TAP) is a compact 10π aromatic compound, and a simple synthetic method via click reactions has been reported [11]. TAP derivatives are high-sensitivity small molecules that exhibit solubility in aqueous solvent and allow for the selection of fluorescence properties through substituents [12–16]. A variety of TAP derivatives with different characteristics have been reported. Our

laboratory has reported that TAP-4PH is a novel fluorescent probe that exhibits very low cytotoxicity and fluoresces in the cytoplasm of live cells [17]. TAP-VK1, which contains a vinyl ketone, is a thiol-specific fluorescent labeling reagent, and it has been reported to successfully image the small molecule drug captopril, which is used for hypertension [18]. 2-*p*-nitrophenyl-TAP is a ferroptosis-inducing agent that exhibits photo-induced cytotoxicity selectively in cancer cells [19]. TAP derivatives are highly useful fluorescent small molecules owing to their ability to be tailored for various properties by altering substituents.

Deep learning has recently gained significant attention in image analysis within the biosciences. In particular, image segmentation—tasks that involve identifying specific regions corresponding to individual objects within an image, such as identifying single cells—and unsupervised image exploration, which compares features of image collections to identify changes in cell morphology in image-based drug screening, play a crucial role in single-cell-level cell identification analysis [20].

In this study, I developed a method for identifying cells at the single-cell level using multiplex staining with novel TAP derivatives and a deep learning model developed in our laboratory.

3.3. Experimental procedures

3.3.1. Cell lines and materials

A549 human lung adenocarcinoma cells were obtained from ATCC (Rockville, MD, USA). Mouse Embryonic Fibroblast (MEF) cells were prepared from 13.5-day-old embryos of wild-type mice. H1299(mCh-NLS), expressing mCherry-NLS, were derived from H1299 human non-small cell lung carcinoma cells in our laboratory. 3T3-L1 mouse fibroblasts were obtained from the Japanese Collection of Research Bioresource (JCRB, Tokyo, Japan). Nuclear Green LCS1 (abcam, Cambridge, UK, Cat. ab138904) was dissolved in DMSO (Wako Pure Chemical Industries, Osaka, Japan, Cat. 045-28335) to prepare a 0.5 mM stock solution. ER Tracker Green (Invitrogen, Waltham, MA, USA, Cat. E34251) was dissolved in DMSO to prepare a 100 μM stock solution. ViVidFluor Golgi Green/Red (Wako Pure Chemical Industries, Osaka, Japan, Cat. 227-02171) was dissolved in DMSO to prepare a 1 mM stock solution. LysoTracker Green DND-26 (Invitrogen, Waltham, MA, USA, Cat. L7526) was dissolved in DMSO to prepare a 75 μM stock solution. MitoTracker Red CM-H_2Xros (Invitrogen, Waltham, MA, USA, Cat. M7513) was dissolved in DMSO to prepare a 1 mM stock solution. BODIPY493/503 (Invitrogen, Waltham, MA, USA, Cat. D3922) was dissolved in DMSO to prepare a 1 mM stock solution. Hoechst33342 (Sigma-Aldrich, St. Louis, MO, USA, Cat. B2261) was dissolved in PBS to prepare a 1 mg/mL stock solution. LysoTracker Blue DND-22 (Invitrogen, Waltham, MA, USA, Cat. L7525) was dissolved in DMSO to prepare a 75 μM stock solution. BioTracker 405 Blue Mitochondria Dye (Sigma-Aldrich, St. Louis, MO, USA, Cat. SCT135) was dissolved in DMSO to prepare a 200 μM stock solution. MDH (AUTODOT, Abgent, San Diego, CA, USA, Cat. SM1000a) was dissolved in DMSO to prepare a 0.1 M stock solution. PPM1D inhibitor SL-176 was obtained from Laboratory of Organic Chemistry II (Faculty of Science, Hokkaido University). SL-176 was dissolved in ethanol (EtOH, Wako Pure Chemical Industries, Osaka, Japan, Cat. 054-07225) to prepare a 8 mM stock solution. Insulin (Sigma-Aldrich, St. Louis, MO, USA, Cat. I0516-5ML) was 10 mg/mL stock. Dexamethasone (Wako Pure

Chemical Industries, Osaka, Japan, Cat. 047-18863) was dissolved in EtOH to prepare a 10 mM stock solution. 3-Isobutyl-1-methylxanthine (IBMX, Sigma-Aldrich, St. Louis, MO, USA, Cat. I5789-250MG) was dissolved in DMSO to prepare a 100 mM stock solution.

3.3.2. Synthesis of TAP compounds

ab-TAP-4PH was carried out as follows (**Scheme 3-1**). First, 1.2 g of 4-bromo-4'-iodobiphenyl (**1**) was subjected to a Negishi coupling with 10 mL of 0.5 M organozinc reagent (**2**), yielding ester **3** with a selective reaction at the iodide site in an 80% yield (0.93 g). Next, ester **3** (840 mg) was coupled with 714 mg of TMS-acetylene through a Sonogashira reaction, synthesizing biphenyl **4** with an 87% yield (770 mg). After the DIBAL reduction of ester **4** (809 mg), followed by the removal of the TMS group and the mesylation of the resulting alcohol, acetylene **5** was synthesized with a 92% yield over the three-step process (877 mg). A click reaction was performed between the freed terminal acetylene **5** (155.4 mg) and azide **6** (221.9 mg), inducing the TAP structure and yielding TAP derivative **7** with a 60% yield (297.5 mg). Using sodium azide, an azide group was introduced to the side chain terminal of TAP derivative **7** (285 mg), resulting in azide **8** with a 95% yield (338.6 mg). Finally, 30 mg of azide **8** was reduced through hydrogenation, yielding the target compound ab-TAP-4PH (**9**) in a 50% yield (8 mg). After scaling up, a total of 23.7 mg of ab-TAP-4PH was obtained.

TAP-2CY4E1 was synthesized as previously described [16].

Scheme 3-1. Synthesis route of ab-TAP-4PH.

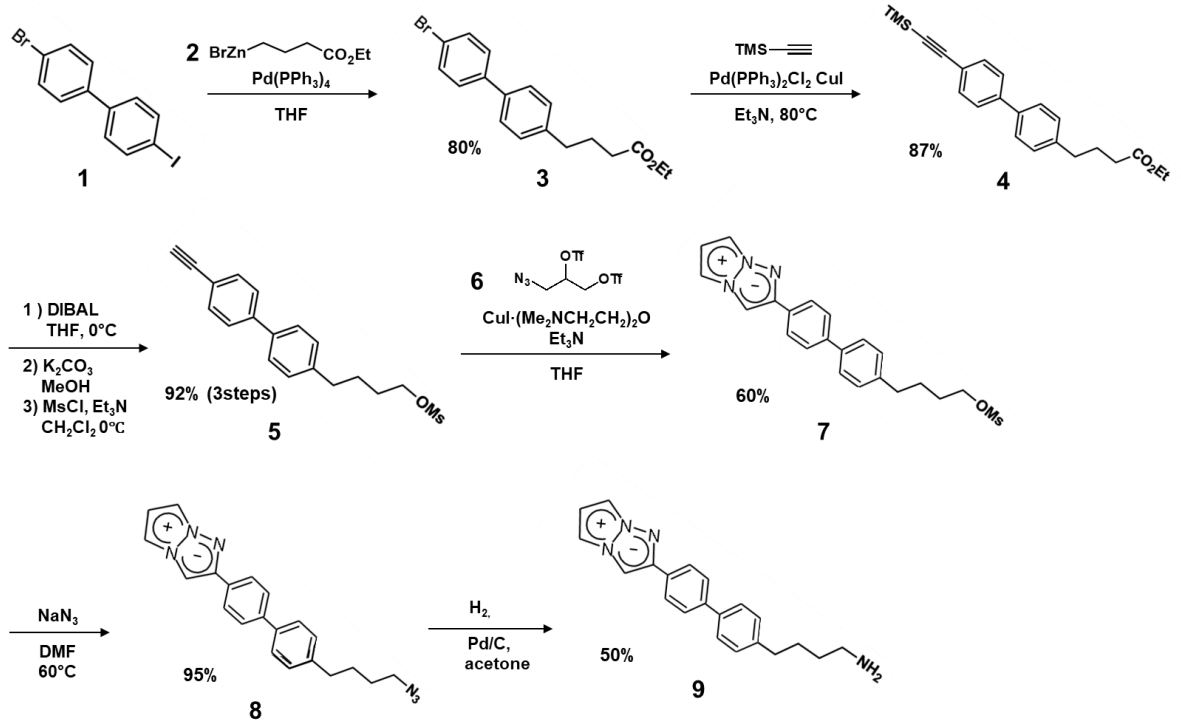

3.3.3. Cell manipulation

A549 and MEF cells were cultured in Dulbecco's modified Eagle's medium (DMEM, Sigma-Aldrich, St. Louis, MO, USA, Cat. D5796-500ML) supplemented with 10% v/v fetal bovine serum (FBS), 100 units/mL penicillin and 100 μg/mL streptomycin (P/S, Thermo Fisher Scientific, Waltham, MA, USA, Cat. 15140-122) at 37°C in an atmosphere of 5% CO_2. H1299 cells were cultured in Roswell Park Memorial Institute medium-1640 (RPMI, Sigma-Aldrich, St. Louis, MO, USA, Cat. R8758-1L) supplemented with 10% v/v FBS, 100 units/mL penicillin and 100 μg/mL streptomycin at 37°C in an atmosphere of 5% CO_2. 3T3-L1 cells were grown in Dulbecco's modified Eagle's medium (DMEM, Sigma-Aldrich, St. Louis, MO, USA, Cat. D5796-500ML) supplemented with 10% v/v Newborn Calf Serum (NBCS, Thermo Fisher Scientific, Waltham, MA, USA, Cat. 16010159) at 37°C in an atmosphere of 5% CO_2. 3T3-L1 cells were seeded at a density of 1.0×10^4 cells in 96-well plates. Two days after 100% cell confluence (day 0), the cells were cultured in differentiation medium (MDI) [DMEM

containing 10% v/v FBS with 100 units/mL penicillin and 100 μg/mL streptomycin (P/S) with 1.0 μg/mL insulin, 1.0 μM dexamethasone, and 0.5 mM IBMX]. Cells were placed in adipocyte maintenance medium (DMEM containing 10% FBS with P/S and 1.0 μg/mL insulin) on day 1. Media were exchanged to adipocyte maintenance medium every 2 days until day 8 of induction of differentiation. Then the cells were treated with 15 μM SL-176 every 2 days until day 15.

3.3.4. Fluorescence spectroscopy

Fluorescence spectra of ab-TAP-4PH and TAP-2CY4E1 (10 μM) in the indicated solutions were measured using a Fluorescence Spectrophotometer F-4500 (Hitachi, Ltd., Tokyo, Japan) under the following conditions. Excitation wavelength of ab-TAP-4PH: 341 nm; excitation wavelength of TAP-2CY4E1: 420 nm; scan speed: 1200 nm/min; excitation and emission slit: 5 nm; PMT voltage: 700 V.

3.3.5. Fluorescence microscopy analysis

A549 or MEF cells were seeded at a density of 0.8×10^4 cells in a glass based dish and cultured for 24 h prior to treatment. For analysis of ab-TAP-4PH localization, cellular organelle co-staining with the nucleus by Nuclear Green LCS1 (2 μM, 30 min) or ER by ER Tracker Green (1 μM, 30 min) or Golgi apparatus by ViVidFluor Golgi Green/Red (5 μM, 30 min) or lysosome by LysoTracker Green DND-26 (75 nM, 30 min) or mitochondria by MitoTracker Red CM-H_2Xros (200 nM, 30 min) or lipid droplet by BODIPY493/503 (1 μM, 30 min) at 37℃ was performed in accordance with the manufacturers' instructions before addition of ab-TAP-4PH. After staining with the indicated organelle probes, the cells were treated with 20 μM ab-TAP-4PH/Opti-MEM for 30 min at 37℃ and then observed under a fluorescence microscope (BZ-9000, Keyence, Osaka, Japan) using the following filter set: DAPI-B (Ex 360/40 nm, Em 460/50 nm) for detection of ab-TAP-4PH, GFP-B (Ex 470/40 nm, Em 535/50 nm) for detection of Nuclear Green LCS1, ER Tracker Green, ViVidFluor Golgi Green/Red,

LysoTracker Green DND-26, and BODIPY493/503, and TRITC (Ex 540/25 nm, Em 605/55 nm) for detection of MitoTracker Red CM-H_2Xros. For analysis of TAP-2CY4E1 localization, cellular organelle co-staining with the nucleus by Hoechst33342 (5 μg/mL, 30 min) or ER by Cell Navigator Live Cell ER Staining Kit Blue Fluorescence (AAT Bioquest, Pleasanton, CA, USA, Cat. 22634) (30 min) or lysosome by LysoTracker Blue DND-22 (75 nM, 30 min) or mitochondria by BioTracker 405 Blue Mitochondria Dye (100 nM, 30 min) or lipid droplet by MDH (10 μM, 30 min) at 37°C was performed in accordance with the manufacturers' instructions before addition of TAP-2CY4E1. After staining with the indicated organelle probes, the cells were treated with 10 μM TAP-2CY4E1/Opti-MEM for 30 min at 37°C and then observed under a fluorescence microscope (BZ-9000) using the following filter set: DM511 (Ex 452 nm, Em 607 nm) for detection of TAP-2CY4E1 and DAPI-B (Ex 360/40 nm, Em 460/50 nm) for detection of Hoechst33342, Cell Navigator Live Cell ER Staining Kit Blue Fluorescence, LysoTracker Blue DND-22, BioTracker 405 Blue Mitochondria Dye, and MDH. Pearson Correlation Coefficent was calculated using ImageJ software. For the experiment of wash out removable assay of TAP derivatives, cells were incubated with 20 μM ab-TAP-4PH/Opti-MEM or 10 μM TAP-2CY4E1/Opti-MEM for 30 min at 37°C, then cells were washed with PBS three times and incubated in fresh medium without TAP compounds. Cells were observed under a fluorescence microscope (BZ-9000) using the following filter set: DAPI-B (Ex 360/40 nm, Em 460/50 nm) for detection of ab-TAP-4PH and DM511 (Ex 452 nm, Em 607 nm) for detection of TAP-2CY4E1.

3.3.6. Cell proliferation assay

A549 or MEF cells were seeded at a density of 0.6×10^4 cells in a 48-well plate and cultured for 24 h prior to treatment. ab-TAP-4PH or TAP-2CY4E1 was added at 0, 5, 10, 20, 30, 50 μM to the culture medium, followed by 24 h incubation. Cell viability was measured by Burker-turk line (Erma, Japan).

For the experiment of wash out removable assay of TAP derivatives, A549 cells were seeded at a density of 0.6×10^4 cells or MEF cells were seeded at a density of 0.8×10^4 cells in a 48-well plate and cultured for 24 h prior to treatment. Cells were incubated with 20 μM ab-TAP-4PH/Opti-MEM or 10 μM TAP-2CY4E1/Opti-MEM or both TAP compounds/Opti-MEM for 30 min at 37℃, then cells were washed with PBS three times and incubated in fresh medium without TAP compounds for 24 h or 48 h. Cell viability was measured by Burker-turk line.

3.3.7. Detection of individual cell by deep learning model

A549 and H1299 cells were seeded at a total density of 0.3×10^4 cells with A549:H1299 ratios of 90%:10%, 70%:30%, 50%:50%, 30%:70%, and 10%:90% respectively in a 96-well plate and cultured for 24 h prior to treatment. Cells were incubated with 20 μM ab-TAP-4PH and 10 μM TAP-2CY4E1/Opti-MEM for 30 min at 37℃, and then observed under a fluorescence microscope (BZ-9000) using the following filter set: DAPI-B (Ex 360/40 nm, Em 460/50 nm) for detection of ab-TAP-4PH and DM511 (Ex 452 nm, Em 607 nm) for detection of TAP-2CY4E1.

Deep learning model developed in our laboratory was trained using images of 36 cells stained with 20 μM ab-TAP-4PH and 10 μM TAP-2CY4E1, split into training, validation, and test sets in a 7:1:1 ratio. To prevent identification issues due to human experimental operations such as background, the chosen CAM model consisted of images captured from completely different wells for the train, validation, and test datasets. The training was conducted on an NVIDIA L4 Tensor core GPU, using Cross-Entropy as the loss function. The learning rate was set as a hyperparameter to maximize validation accuracy within the search space, utilizing a TPE sampler from Optuna, with a batch size adjusted to 128 for the low-resolution model and 16 for the high-resolution model. Hyperparameter optimization was performed using Optuna. To prevent variations in the learning process due to initial parameters, a pre-trained ResNet 50 from the timm model was used, and all random numbers generated during the

learning process were fixed at 42. For the conditions with cell ratios of A549:H1299 at 1:9, 3:7, 7:3, and 9:1, validation was performed on 20 randomly selected images using a Python script. The Precision (Equation 1) and Recall (Equation 2) in the validation were calculated for the cells where the generated rectangles overlapped the most.

$$Precision = \frac{TP}{TP + FP} \tag{1}$$

$$Recall = \frac{TP}{TP + FN} \tag{2}$$

The F1 score can be defined as:

$$F1 = \frac{2 \times TP}{2 \times TP + FN + FP} \tag{3}$$

TP (True Positive): The number of cells predicted as A549 that were actually A549; FP (False Positive): The number of cells predicted as A549 but were actually H1299; TN (True Negative): The number of cells predicted as H1299 that were actually H1299; FN (False Negative): The number of cells predicted as H1299 but were actually A549.

3.3.8. Detection of adipocytes by deep learning model

3T3-L1 cells were cultured as described above. Cells were incubated with 20 μM ab-TAP-4PH and 10 μM TAP-2CY4E1/Opti-MEM for 30 min at 37℃, and then observed under a fluorescence microscope (BZ-9000) using the following filter set: DAPI-B (Ex 360/40 nm, Em 460/50 nm) for detection of ab-TAP-4PH and DM511 (Ex 452 nm, Em 607 nm) for detection of TAP-2CY4E1. Deep

learning model developed in our laboratory was trained as described above.

3.4. Results

3.4.1. Spectroscopic properties of ab-TAP-4PH

To image the diverse states within cells, a novel TAP derivative, ab-TAP-4PH, containing a 4-aminobutyl group in its side chain was designed and synthesized (**Figure 3-1A**). The absorption fluorescence spectrum of ab-TAP-4PH in dichloromethane (DCM) was measured, revealing a characteristic absorbance peak at 341 nm, with λ_{em}^{max} at 457 nm (**Figure 3-1B**). The fluorescence spectra measured in solvents with varying hydrophobicity, including DCM, EtOH, H_2O, PBS, acetonitrile, and acetone, showed that the highest fluorescence intensity was observed in H_2O (**Figure 3-1C**). To analyze the pH dependence of ab-TAP-4PH fluorescence, fluorescence spectra were measured in aqueous solutions with pH levels ranging from 4.0 to 8.0. The results showed that the highest fluorescence intensity was observed at pH 4.0, and the fluorescence intensity decreased as the pH increased (**Figure 3-1D**). The fluorescence intensity significantly decreased with the change from pH 5.5 to pH 6.0, and the fluorescence intensity was notably low at pH 6.0, pH 6.5, and pH 7.0.

It has been demonstrated that ab-TAP-4PH exhibits strong fluorescence in polar solvents. Furthermore, the fluorescence intensity varies in a pH-dependent manner, becoming stronger in acidic regions.

3.4.2. Spectroscopic properties of TAP-2CY4E1

The absorption fluorescence spectrum of the TAP derivative TAP-2CY4E1 (**Figure 3-2A**), which has 3-cyanobenzoyl acid in its side chain, was measured in DCM. TAP-2CY4E1 exhibited a characteristic absorbance peak at 420 nm, with λ_{em}^{max} at 544 nm (**Figure 3-2B**). The fluorescence spectra measured in solvents with varying hydrophobicity, including DCM, EtOH, H_2O, PBS, acetonitrile, and acetone, showed that the highest fluorescence intensity was observed in DCM (**Figure 3-2C**). The fluorescence intensities in EtOH, H_2O, PBS, acetonitrile, and acetone were very weak compared to those

in DCM. The fluorescence spectra of TAP-2CY4E1 were measured in aqueous solutions at different pH levels. Almost no fluorescence was observed across the pH range of 4.0 to 8.0, and no significant changes in fluorescence intensity were detected (**Figure 3-2D**).

It has been revealed that TAP-2CY4E1 emits high fluorescence in hydrophobic regions and shows little pH dependence in hydrophilic regions.

It was also demonstrated that ab-TAP-4PH exhibits strong fluorescence in polar solvents, while TAP-2CY4E1 emits strong fluorescence in hydrophobic regions, indicating that they have distinct fluorescence spectral characteristics in response to solvents. Furthermore, in hydrophilic regions, ab-TAP-4PH shows a pH-dependent change in fluorescence intensity, whereas TAP-2CY4E1 exhibited little pH dependence. These results suggest that, due to their solvent-dependent fluorescent intensities, ab-TAP-4PH and TAP-2CY4E1 can be used to stain different cellular compartments. Thus, it has been demonstrated that ab-TAP-4PH and TAP-2CY4E1 can be used for multiplex staining.

3.4.3. Intracellular localization of ab-TAP-4PH and TAP-2CY4E1

Since ab-TAP-4PH and TAP-2CY4E1 exhibit solvent-dependent changes in their fluorescence spectra, they may localize differently depending on the intracellular environment. To analyze the intracellular localization of ab-TAP-4PH and TAP-2CY4E1, we examined the correlation of their fluorescence patterns with organelle-specific staining reagents. Using organelle-specific fluorescent probes in A549 human lung adenocarcinoma cells and mouse embryonic fibroblasts (MEFs), we analyzed the correlation of ab-TAP-4PH fluorescence patterns with those of the ER, Golgi apparatus, lipid droplets, lysosomes, mitochondria, and nuclei.

ab-TAP-4PH was broadly localized in the cytoplasm and showed high fluorescence intensity in the ER, lysosomes, and Golgi apparatus, but its fluorescence did not completely coincide with these organelles (**Figure 3-3, 3-4**). The Pearson correlation coefficients for ab-TAP-4PH with ER and

lysosomal staining probes were 0.82 and 0.80 in A549 cells, and 0.82 and 0.77 in MEFs, respectively (**Table 3-1**). This indicates that ab-TAP-4PH demonstrated a strong positive correlation with the ER and lysosomes. In contrast, its fluorescence patterns differed from those of nuclear, mitochondrial, and lipid droplet staining probes. The Pearson correlation coefficients for ab-TAP-4PH with nuclear, mitochondrial, and lipid droplet staining probes were -0.48, -0.01, and 0.05 in A549 cells, and -0.54, 0.00, and 0.17 in MEFs, respectively.

TAP-2CY4E1 exhibited high fluorescence intensity in the ER and lipid droplets (**Figure 3-5, 3-6**). The Pearson correlation coefficients for TAP-2CY4E1 with ER and lipid droplet staining probes were 0.92 and 0.84 in A549 cells, and 0.91 and 0.83 in MEFs, respectively, indicating a particularly strong positive correlation with the ER and lipid droplets. (**Table 3-2**) In contrast, its fluorescence patterns differed from those of nuclear and lysosomal staining probes. The Pearson correlation coefficients for TAP-2CY4E1 with nuclear and lysosomal staining probes were -0.44 and 0.06 in A549 cells, and -0.41 and 0.04 in MEFs, respectively.

It has been revealed that ab-TAP-4PH exhibits strong fluorescence in the ER and lysosomes but does not localize exclusively to a single organelle. Additionally, TAP-2CY4E1 was found to stain regions of lipid droplets that are not stained by ab-TAP-4PH. These findings suggest that multiplex staining with ab-TAP-4PH and TAP-2CY4E1 can simultaneously highlight various cellular regions, reflecting the cell's status with distinct fluorescence patterns.

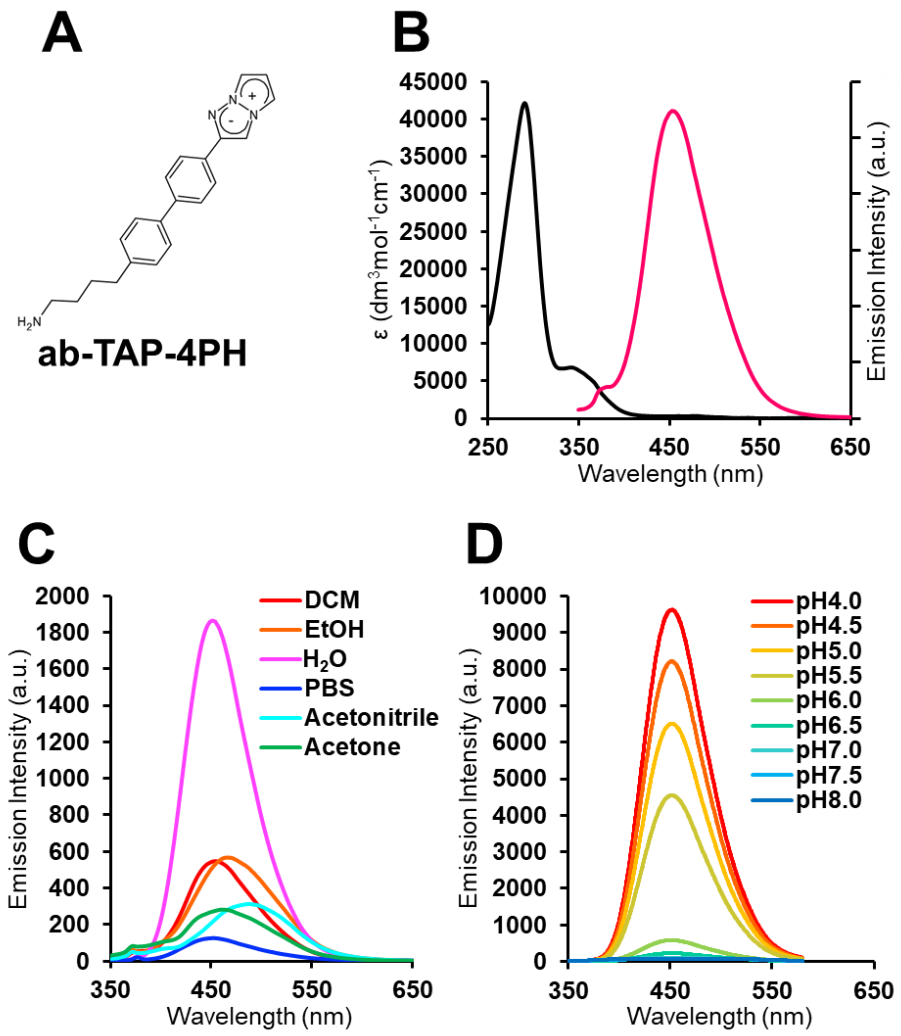

Figure 3-1. Spectroscopic properties of ab-TAP-4PH.

(A) Chemical structure of ab-TAP-4PH. (B) Absorbance and fluorescence emission spectra of 10 µM ab-TAP-4PH in dichloromethane. (C) Fluorescence emission spectra of ab-TAP-4PH in aqueous and organic solvents. λ_{ex} = 341 nm. (D) Fluorescence emission spectra of ab-TAP-4PH in buffer solution with different pH values from pH 4.0 to pH 8.0. (pH 4.0, pH 4.5, pH 5.0, pH 5.5: Acetate buffer; pH 6.0, pH 6.5, pH 7.0: MES buffer; pH 7.0, pH 7.5, pH 8.0: HEPES buffer). λ_{ex} = 341 nm. Slit width: $d_{ex} = d_{em}$ = 2.5 nm.

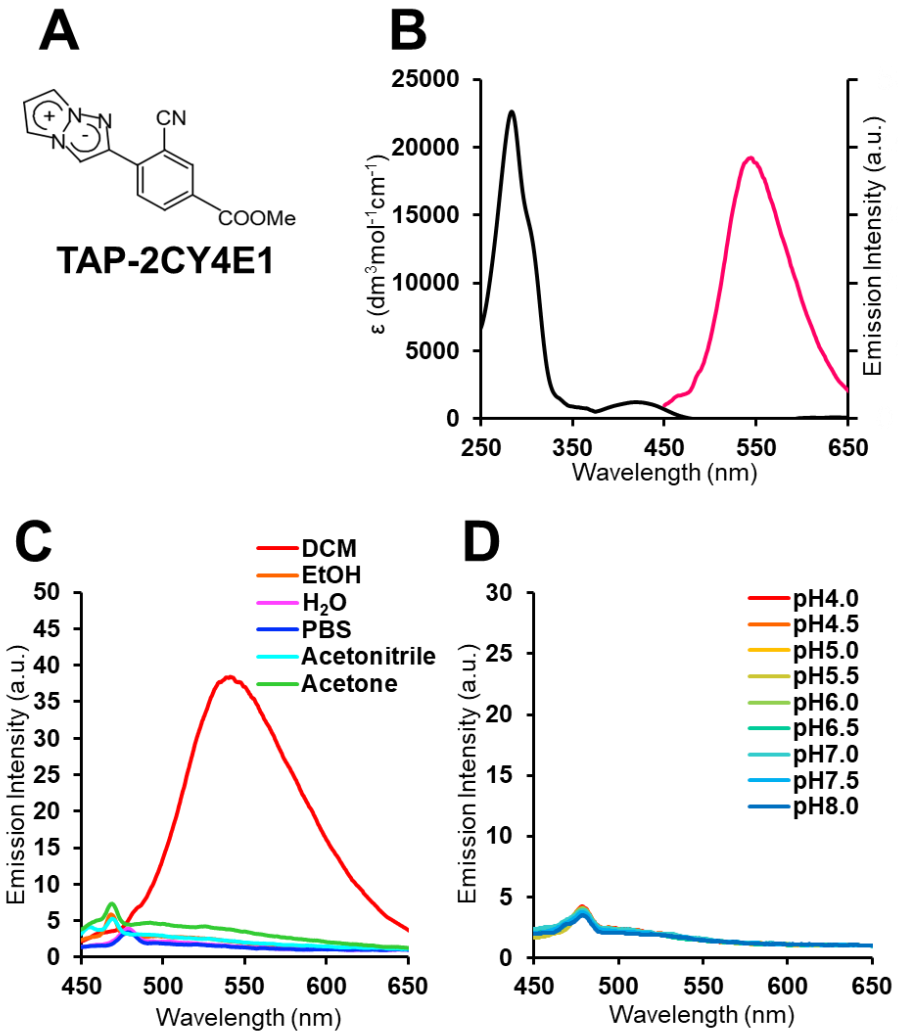

Figure 3-2. Spectroscopic properties of TAP-2CY4E1.

(A) Chemical structure of TAP-2CY4E1. (B) Absorbance and fluorescence emission spectra of 10 μM TAP-2CY4E1 in dichloromethane. (C) Fluorescence emission spectra of TAP-2CY4E1 in aqueous and organic solvents. λ_{ex} = 420 nm. (D) Fluorescence emission spectra of TAP-2CY4E1 in buffer solution with different pH values from pH 4.0 to pH 8.0. (pH 4.0, pH 4.5, pH 5.0, pH 5.5: Acetate buffer; pH 6.0, pH 6.5, pH 7.0: MES buffer; pH 7.0, pH 7.5, pH 8.0: HEPES buffer). λ_{ex} = 420 nm. Slit width: $d_{ex} = d_{em}$ = 2.5 nm.

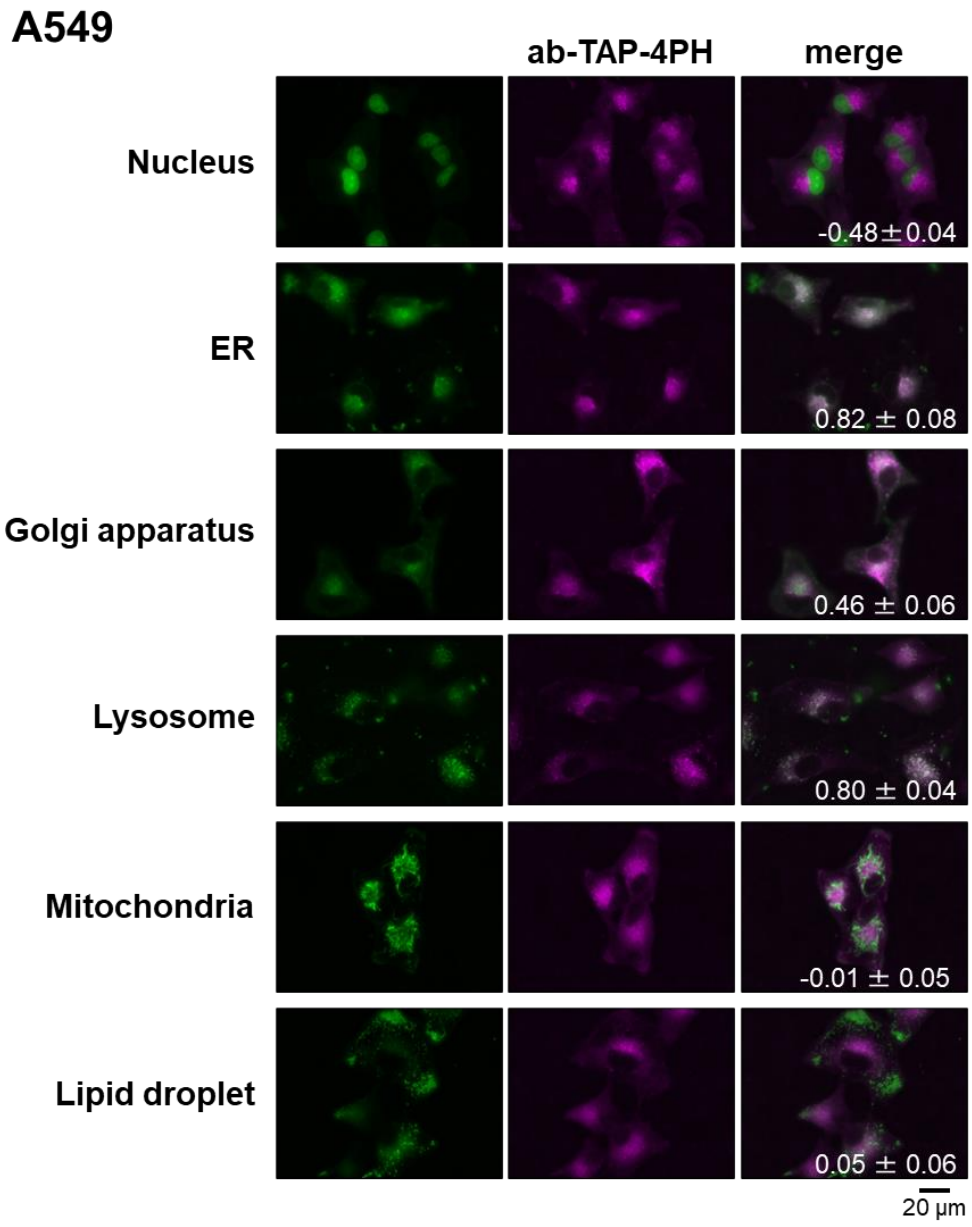

Figure 3-3. Intracellular localization of ab-TAP-4PH in A549 cells.

Fluorescence microscopy images of A549 cells costained with ab-TAP-4PH (20 μM, 30 min) and Nucleus: Nuclear Green LCS1 (2 μM, 30 min) or ER: ER Tracker Green (1 μM, 30 min) or Golgi apparatus: ViVidFluor Golgi Green/Red (5 μM, 30 min) or Lysosome: LysoTracker Green DND-26 (75 nM, 30 min) or Mitochondria: MitoTracker Red CM-H_2Xros (200 nM, 30 min) or Lipid droplet: BODIPY493/503 (1 μM, 30 min) at 37℃. ab-TAP-4PH, Ex 360/40 nm, Em 460/50 nm; Nuclear Green LCS1, ER Tracker Green, ViVidFluor Golgi Green/Red, LysoTracker Green DND-26, BODIPY493/503, Ex 470/40 nm, Em 535/50 nm; MitoTracker Red CM-H_2Xros, Ex 540/25 nm, Em 605/55 nm. Scale bar: 20 μm. Colocalization coefficients calculated by Pearson correlation coefficient are shown in the merge images. Values represents the mean ± S.D. of three independent experiments.

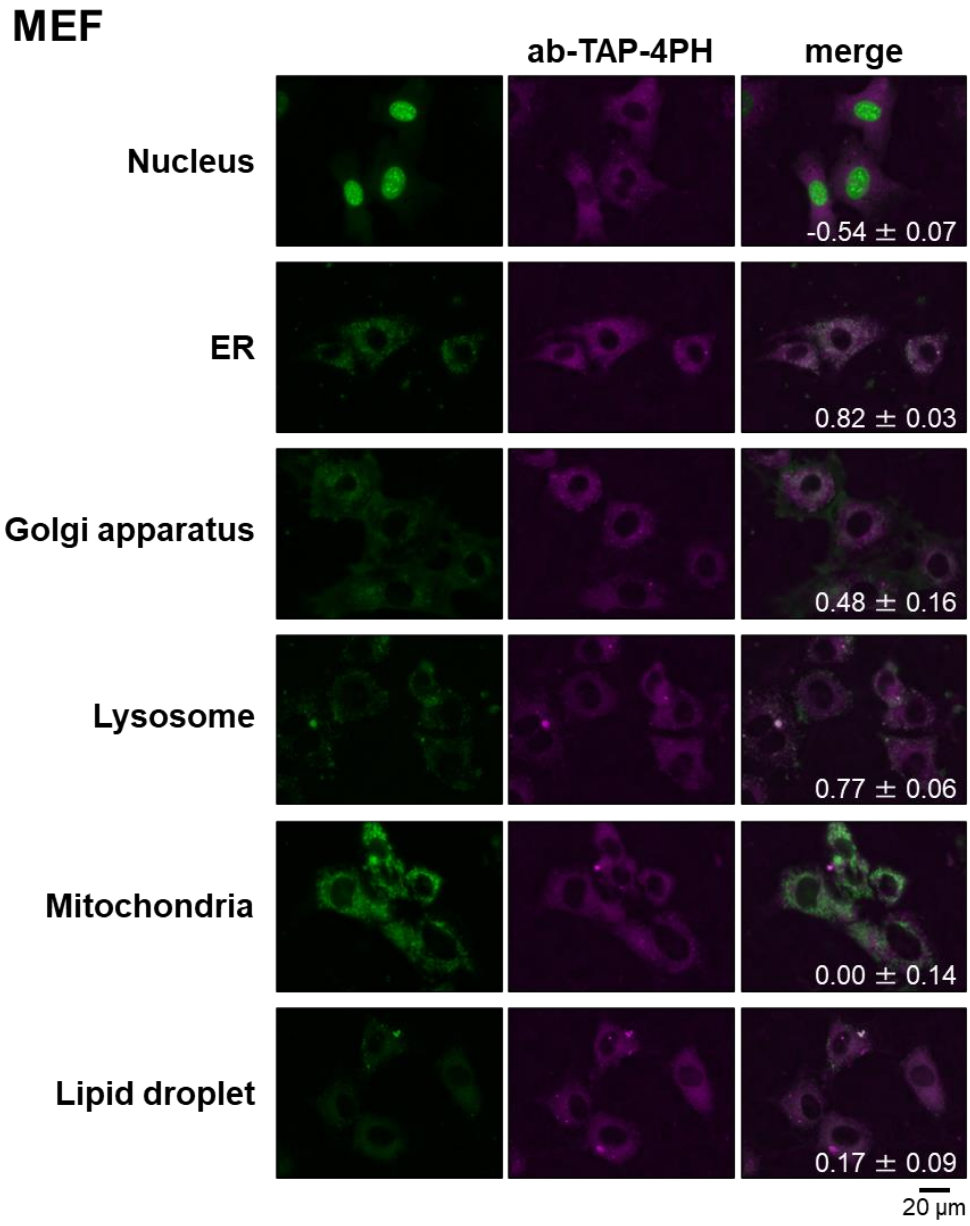

Figure 3-4. Intracellular localization of ab-TAP-4PH in MEF cells.

Fluorescence microscopy images of MEF cells costained with ab-TAP-4PH (20 μM, 30 min) and Nucleus: Nuclear Green LCS1 (2 μM, 30 min) or ER: ER Tracker Green (1 μM, 30 min) or Golgi apparatus: ViVidFluor Golgi Green/Red (5 μM, 30 min) or Lysosome: LysoTracker Green DND-26 (75 nM, 30 min) or Mitochondria: MitoTracker Red CM-H_2Xros (200 nM, 30 min) or Lipid droplet: BODIPY493/503 (1 μM, 30 min) at 37°C. ab-TAP-4PH, Ex 360/40 nm, Em 460/50 nm; Nuclear Green LCS1, ER Tracker Green, ViVidFluor Golgi Green/Red, LysoTracker Green DND-26, BODIPY493/503, Ex 470/40 nm, Em 535/50 nm; MitoTracker Red CM-H_2Xros, Ex 540/25 nm, Em 605/55 nm. Scale bar: 20 μm. Colocalization coefficients calculated by Pearson correlation coefficient are shown in the merge images. Values represents the mean ± S.D. of three independent experiments.

Table 3-1. Pearson Correlation Coefficient of ab-TAP-4PH and organelle probe.

	Average value of Pearson Correlation Coefficient[1]					
	Nucleus	**ER**	**Golgi apparatus**	**Lysosome**	**Mitochondria**	**Lipid droplet**
A549	-0.48 ± 0.04	0.82 ± 0.08	0.46 ± 0.06	0.80 ± 0.04	-0.01 ± 0.05	0.05 ± 0.06
MEF	-0.54 ± 0.07	0.82 ± 0.03	0.48 ± 0.16	0.77 ± 0.06	0.00 ± 0.14	0.17 ± 0.09

[1]Average values of Pearson Correlation Coefficent are present as the mean ± S.D. obtained via three independent images in each condition. Pearson Correlation Coefficent was calculated using ImageJ software.

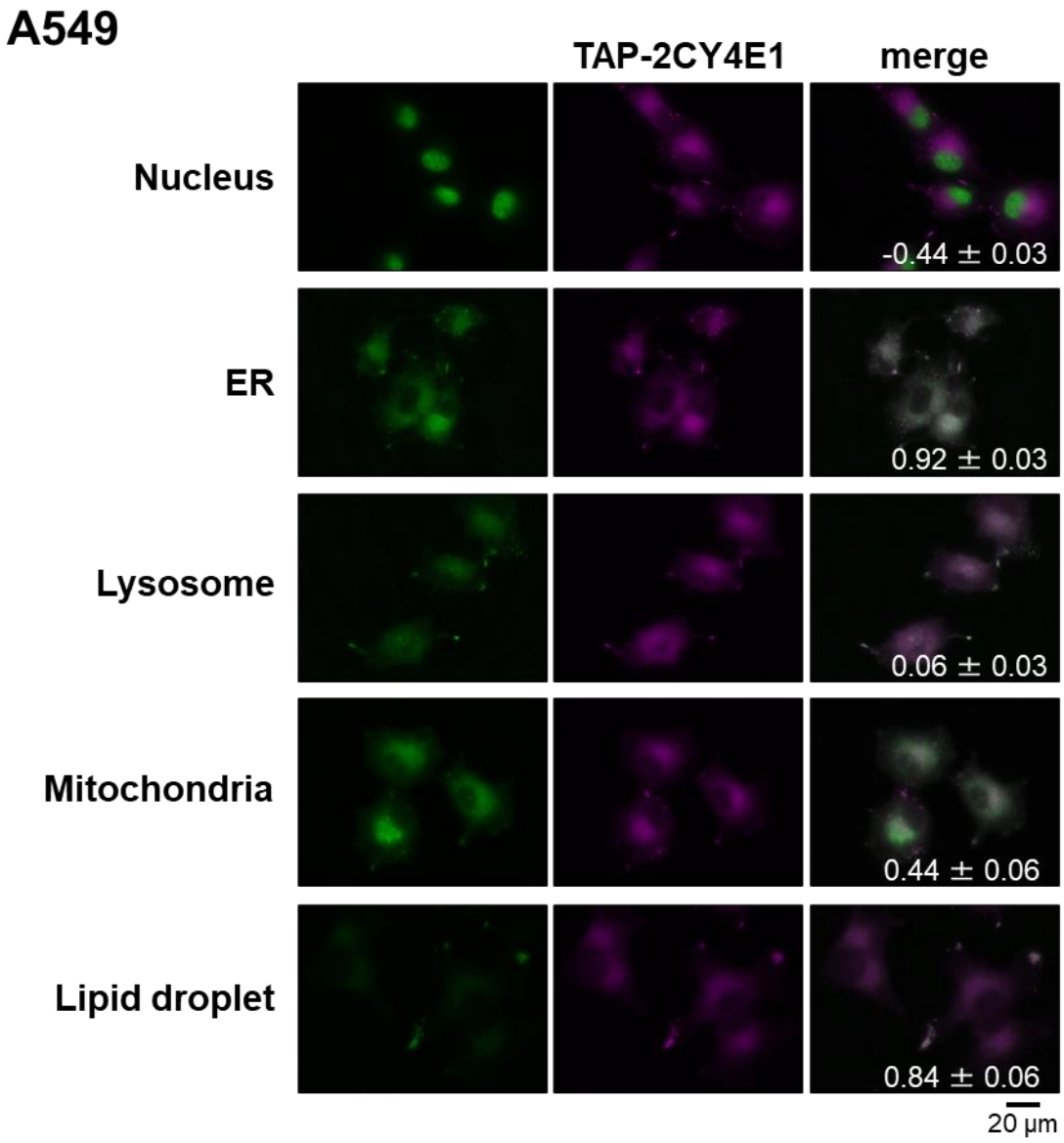

Figure 3-5. Intracellular localization of TAP-2CY4E1 in A549 cells.

Fluorescence microscopy images of A549 cells costained with TAP-2CY4E1 (10 μM, 30 min) and Nucleus: Hoechst33342 (5 μg/mL, 30 min) or ER: Cell Navigator Live Cell ER Staining Kit Blue Fluorescence (30 min) or Lysosome: LysoTracker Blue DND-22 (75 nM, 30 min) or Mitochondria: BioTracker 405 Blue Mitochondria Dye (100 nM, 30 min) or Lipid droplet: MDH (10 μM, 30 min) at 37°C. TAP-2CY4E1, Ex 452 nm, Em 607 nm; Hoechst33342, Cell Navigator Live Cell ER Staining Kit Blue Fluorescence, LysoTracker Blue DND-22, BioTracker 405 Blue Mitochondria Dye, MDH, Ex 360/40 nm, Em 460/50 nm. Scale bar: 20 μm. Colocalization coefficients calculated by Pearson correlation coefficient are shown in the merge images. Values represents the mean ± S.D. of three independent experiments.

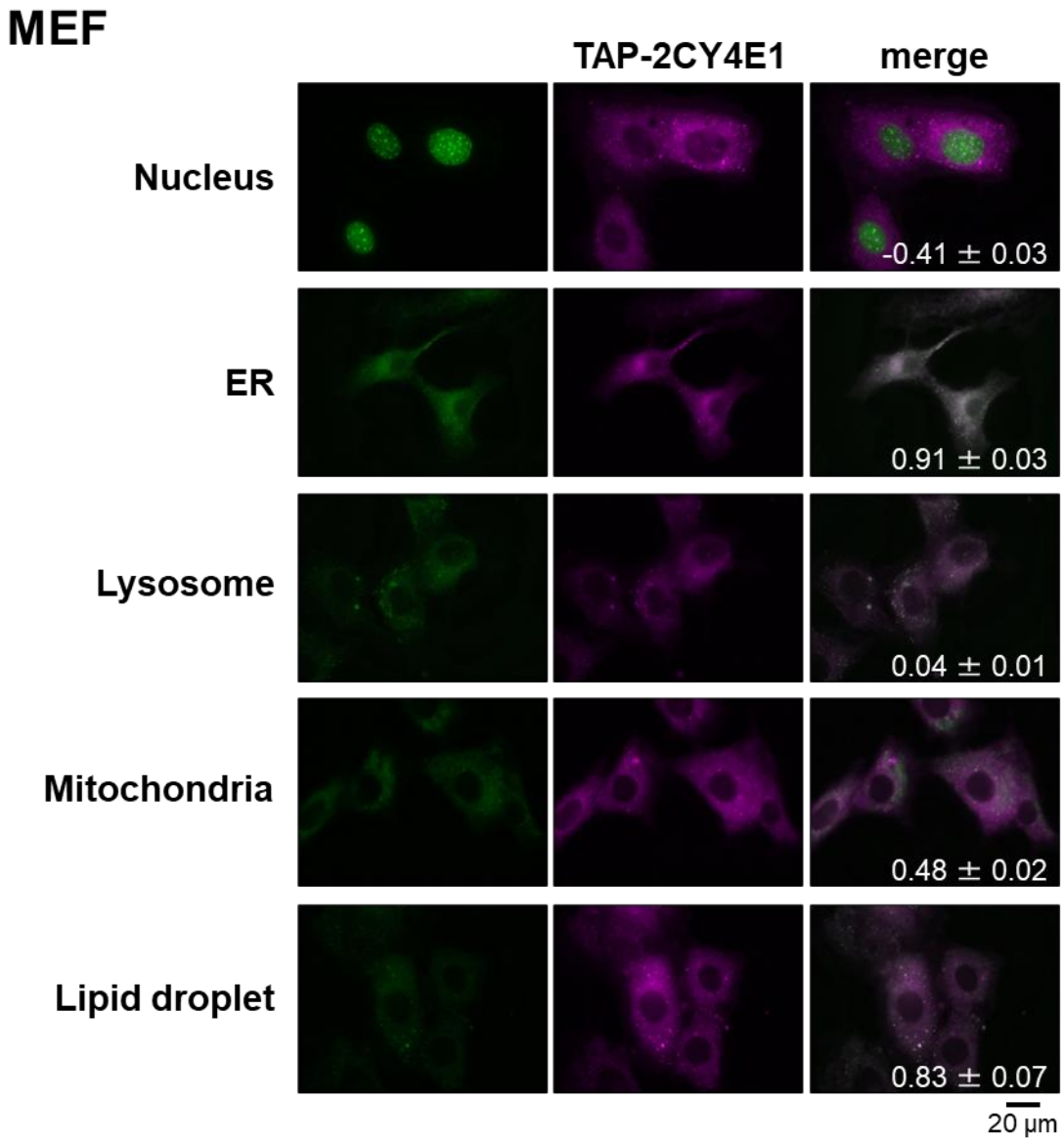

Figure 3-6. Intracellular localization of TAP-2CY4E1 in MEF cells.

Fluorescence microscopy images of MEF cells costained with TAP-2CY4E1 (10 μM, 30 min) and Nucleus: Hoechst33342 (5 μg/mL, 30 min) or ER: Cell Navigator Live Cell ER Staining Kit Blue Fluorescence (30 min) or Lysosome: LysoTracker Blue DND-22 (75 nM, 30 min) or Mitochondria: BioTracker 405 Blue Mitochondria Dye (100 nM, 30 min) or Lipid droplet: MDH (10 μM, 30 min) at 37°C. TAP-2CY4E1, Ex 452 nm, Em 607 nm; Hoechst33342, Cell Navigator Live Cell ER Staining Kit Blue Fluorescence, LysoTracker Blue DND-22, BioTracker 405 Blue Mitochondria Dye, MDH, Ex 360/40 nm, Em 460/50 nm. Scale bar: 20 μm. Colocalization coefficients calculated by Pearson correlation coefficient are shown in the merge images. Values represents the mean ± S.D. of three independent experiments.

Table 3-2. Pearson Correlation Coefficient of TAP-2CY4E1 and organelle probe.

	Average value of Pearson Correlation Coefficient[1]				
	Nucleus	**ER**	**Lysosome**	**Mitochondria**	**Lipid droplet**
A549	-0.44 ± 0.03	0.92 ± 0.03	0.06 ± 0.03	0.44 ± 0.06	0.84 ± 0.06
MEF	-0.41 ± 0.03	0.91 ± 0.03	0.04 ± 0.01	0.48 ± 0.02	0.83 ± 0.07

[1]Average values of Pearson Correlation Coefficent are present as the mean ± S.D. obtained via three independent images in each condition. Pearson Correlation Coefficent was calculated using ImageJ software.

3.4.4. Cytotoxicity of ab-TAP-4PH and TAP-2CY4E1

To evaluate the effects of ab-TAP-4PH and TAP-2CY4E1 on cell proliferation, A549 and MEF cells were treated with ab-TAP-4PH or TAP-2CY4E1 at concentrations of 0, 5, 10, 20, 30, and 50 μM, and the cell count was quantified after 24 hours. In A549 cells, the addition of ab-TAP-4PH did not affect cell numbers up to 50 μM, indicating no observable impact on cell proliferation (**Figure 3-7**). In MEF cells, ab-TAP-4PH showed a concentration-dependent tendency to reduce cell numbers; however, no significant difference was observed up to 30 μM. A significant decrease in cell numbers was noted at 50 μM. These results suggest that ab-TAP-4PH exhibits very low cytotoxicity.

Similarly, TAP-2CY4E1 showed a slight tendency to reduce cell numbers in a concentration-dependent manner in A549 cells, but no significant differences were observed (**Figure 3-8**). In MEF cells, cell numbers at concentrations of 5 μM to 30 μM TAP-2CY4E1 were approximately 75% of those at 0 μM, while a significant reduction in cell numbers was observed at 50 μM. These findings indicate that TAP-2CY4E1 has very low cytotoxicity at concentrations up to 30 μM.

3.4.5. Consecutive analysis of cellular function after TAP treatment

Our laboratory previously reported that TAP-4PH can be removed from cells by washing with PBS after its addition to the cells [17]. Similar analyses were conducted for ab-TAP-4PH and TAP-2CY4E1. A549 cells stained with ab-TAP-4PH or TAP-2CY4E1 were washed three times with PBS and then replaced with fresh medium lacking TAP compounds. The cells were observed under a fluorescence microscope after 5, 15, 30, 60, and 120 minutes. After removing ab-TAP-4PH or TAP-2CY4E1 from the medium, the fluorescence intensity decreased in a time-dependent manner (**Figure 3-9**). These results suggest that ab-TAP-4PH and TAP-2CY4E1 can be easily removed from cells by washing.

To analyze the cytotoxicity after removing ab-TAP-4PH and TAP-2CY4E1 from cells by washing, A549 and MEF cells stained with either ab-TAP-4PH, TAP-2CY4E1, or both ab-TAP-4PH and

TAP-2CY4E1 were washed three times with PBS and then replaced with fresh medium lacking TAP derivatives. The cell counts were quantified after 24 hours and 48 hours. Compared to the control, the cell counts under the conditions of ab-TAP-4PH, TAP-2CY4E1, and the co-staining of ab-TAP-4PH and TAP-2CY4E1 were similar (**Figure 3-10**). These results indicate that staining with ab-TAP-4PH and TAP-2CY4E1 does not affect cell proliferation even after wash-out.

Overall, it has been demonstrated that ab-TAP-4PH and TAP-2CY4E1 are promising compounds as live cell imaging reagents, as they exhibit very low cytotoxicity and can be easily removed from cells by wash-out.

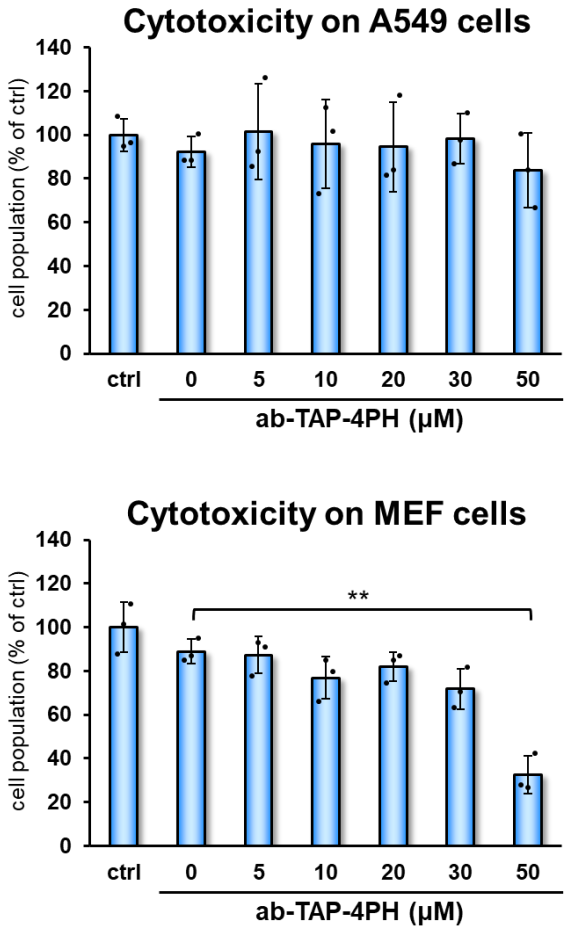

Figure 3-7. Cell proliferation after treatment with ab-TAP-4PH.

Cell number of (A) A549 cells or (B) MEF cells were treated with different concentrations of ab-TAP-4PH for 24 h. Data represents the mean ± S.D. of three independent experiments. Significance was analyzed by using Student's *t*-test. ** $p < 0.01$.

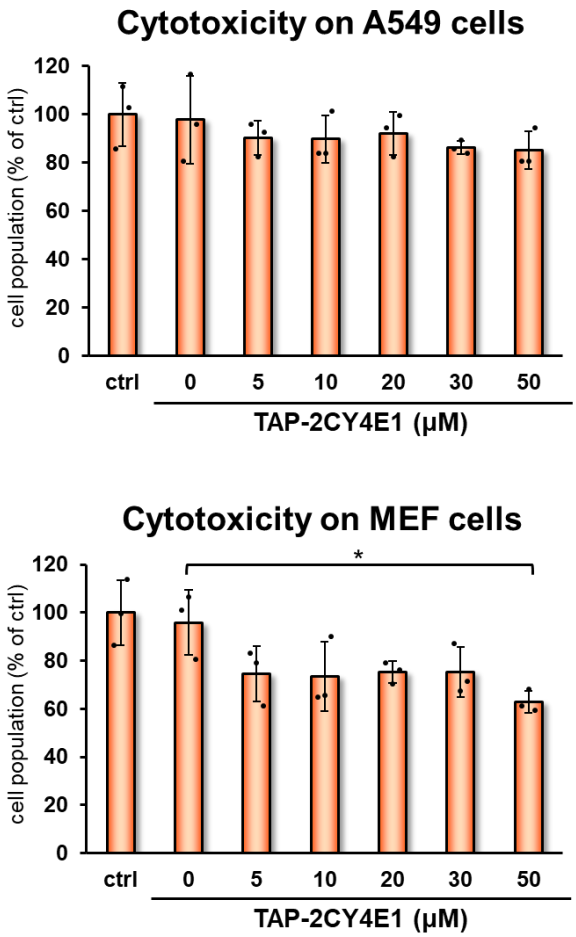

Figure 3-8. Cell proliferation after treatment with TAP-2CY4E1.

Cell number of (A) A549 cells or (B) MEF cells were treated with different concentrations of TAP-2CY4E1 for 24 h. Data represents the mean ± S.D. of three independent experiments. Significance was analyzed by using Student's *t*-test. * $p < 0.05$.

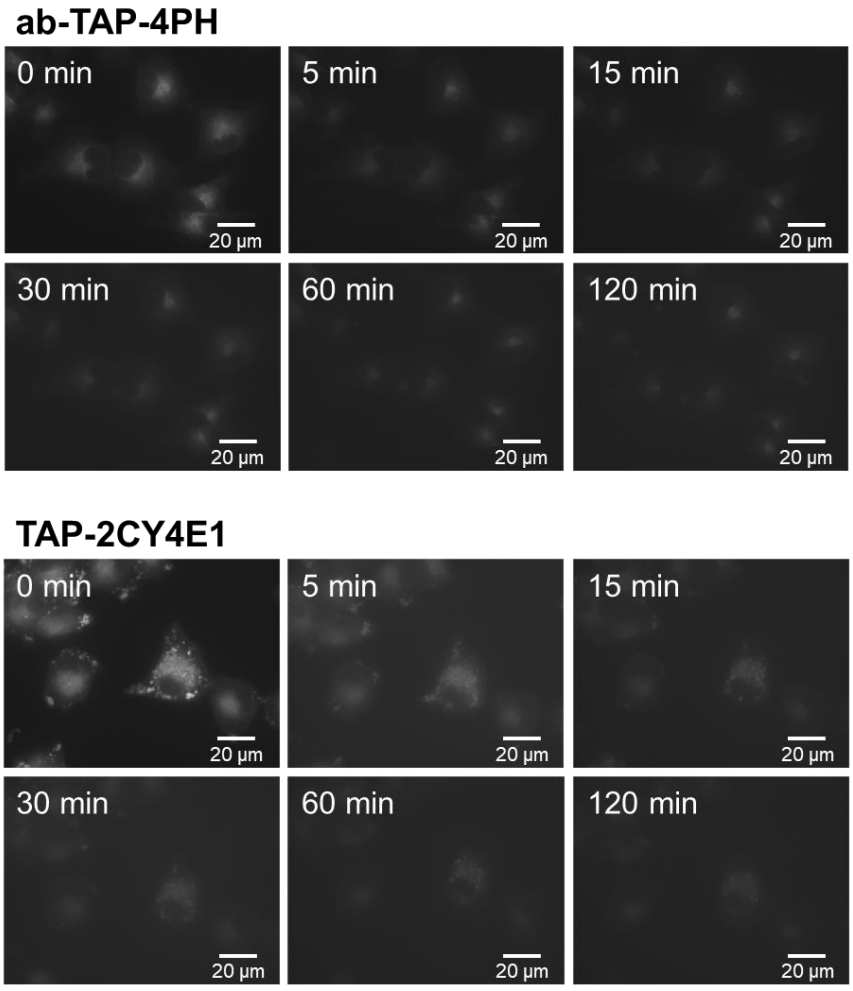

Figure 3-9. Wash out removable of ab-TAP-4PH and TAP-2CY4E1.

Fluorescence microscopy images of A549 cells incubated with ab-TAP-4PH (20 μM) or TAP-2CY4E1 (10 μM) for 30 min at 37℃, then cells were washed and incubated in fresh medium without TAP compounds (time 0 min). Fluorescence microscopy images were taken after incubation for the indicated time periods. ab-TAP-4PH, Ex 360/40 nm, Em 460/50 nm; TAP-2CY4E1, Ex 452 nm, Em 607 nm. Scale bar: 20 μm.

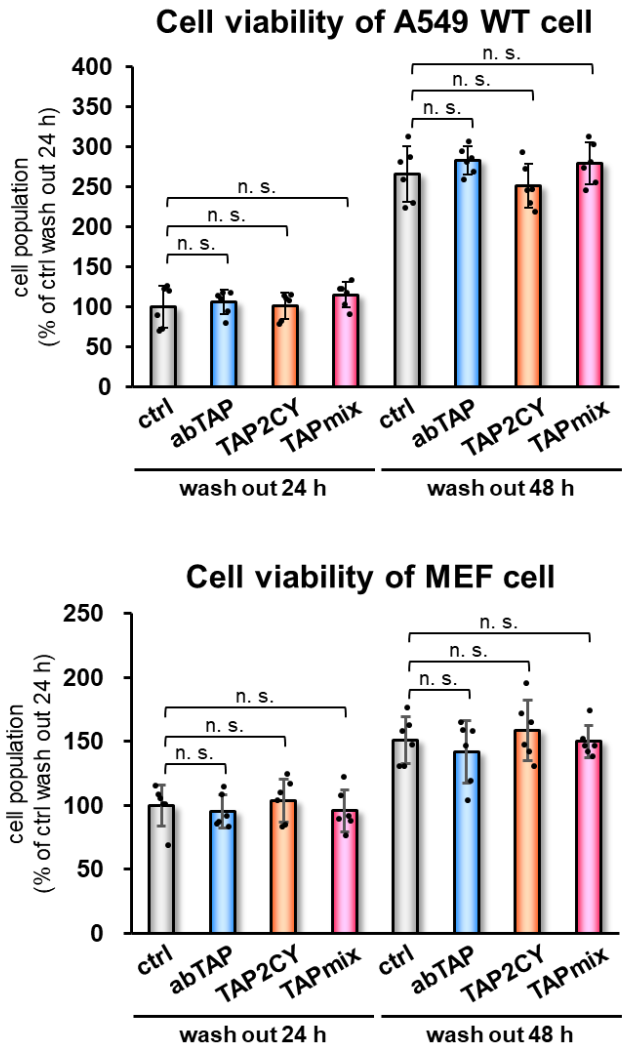

Figure 3-10. Cell proliferation after wash out TAP compounds.

Cell number of A549 or MEF cells were treated with ab-TAP-4PH (20 μM) and/or TAP-2CY4E1 (10 μM) for 30 min at 37°C, then cells were washed and incubated in fresh medium without TAP compounds for 24 h or 48 h. Data represents the mean ± S.D. of six independent experiments. n.s, not statistically significant by Student's *t*-test.

3.4.6. Detection of individual cells in mixed culture with deep learning

Identification analysis of cell types with different statuses of the tumor suppressor protein p53 was conducted. Human alveolar basal epithelial adenocarcinoma cells (A549) and human non-small cell lung cancer-derived H1299 cells were stained with ab-TAP-4PH and TAP-2CY4E1, respectively, and observed using fluorescence microscopy (**Figure 3-11**). In A549 cells, fluorescence from ab-TAP-4PH was observed surrounding the nucleus. In H1299 cells, more cells exhibited round fluorescence in the cytoplasm compared to A549. The fluorescence pattern of TAP-2CY4E1 showed bright spots in H1299 cells with higher fluorescence intensity compared to A549. A549 and H1299 cells were co-cultured and stained with ab-TAP-4PH and TAP-2CY4E1. Fluorescence images of ab-TAP-4PH, TAP-2CY4E1, and phase-contrast images from co-cultured cells at different ratios (A549:H1299 = 90%:10%, 70%:30%, 50%:50%, 30%:70%, 10%:90%) were analyzed using a deep learning model to predict cell types for each individual cell (**Figure 3-12**). The results showed that the F1 score, the harmonic mean of precision and recall, was 0.924 for 9:1, 0.964 for 7:3, 0.952 for 5:5, 0.948 for 3:7, and 0.919 for 1:9, indicating high accuracy in distinguishing cell types (**Table 3-3**). Overall, multiplex staining with ab-TAP-4PH and TAP-2CY4E1 enabled high-precision identification of A549 and H1299 cells with different p53 statuses.

To demonstrate the effectiveness of TAP derivatives in cell identification analysis, a deep learning model was evaluated using only phase-contrast images, ab-TAP-4PH fluorescence images only, and TAP-2CY4E1 fluorescence images only. The analysis combining ab-TAP-4PH fluorescence images, TAP-2CY4E1 fluorescence images, and phase-contrast images yielded a Precision of 0.977 and a Recall of 0.933, whereas the analysis using only phase contrast images resulted in a Precision of 0.676 and a Recall of 0.547 (**Table 3-4**). In the analysis using ab-TAP-4PH fluorescence images only, the Precision was 0.694 and the Recall was 0.610. In the analysis using TAP-2CY4E1 fluorescence images only, the Precision was 0.621 and the Recall was 0.535. These results demonstrate that multiplex staining with

ab-TAP-4PH and TAP-2CY4E1 is highly effective for cell identification.

Overall, successful single-cell-level cell identification was achieved using multiplex staining with ab-TAP-4PH and TAP-2CY4E1.

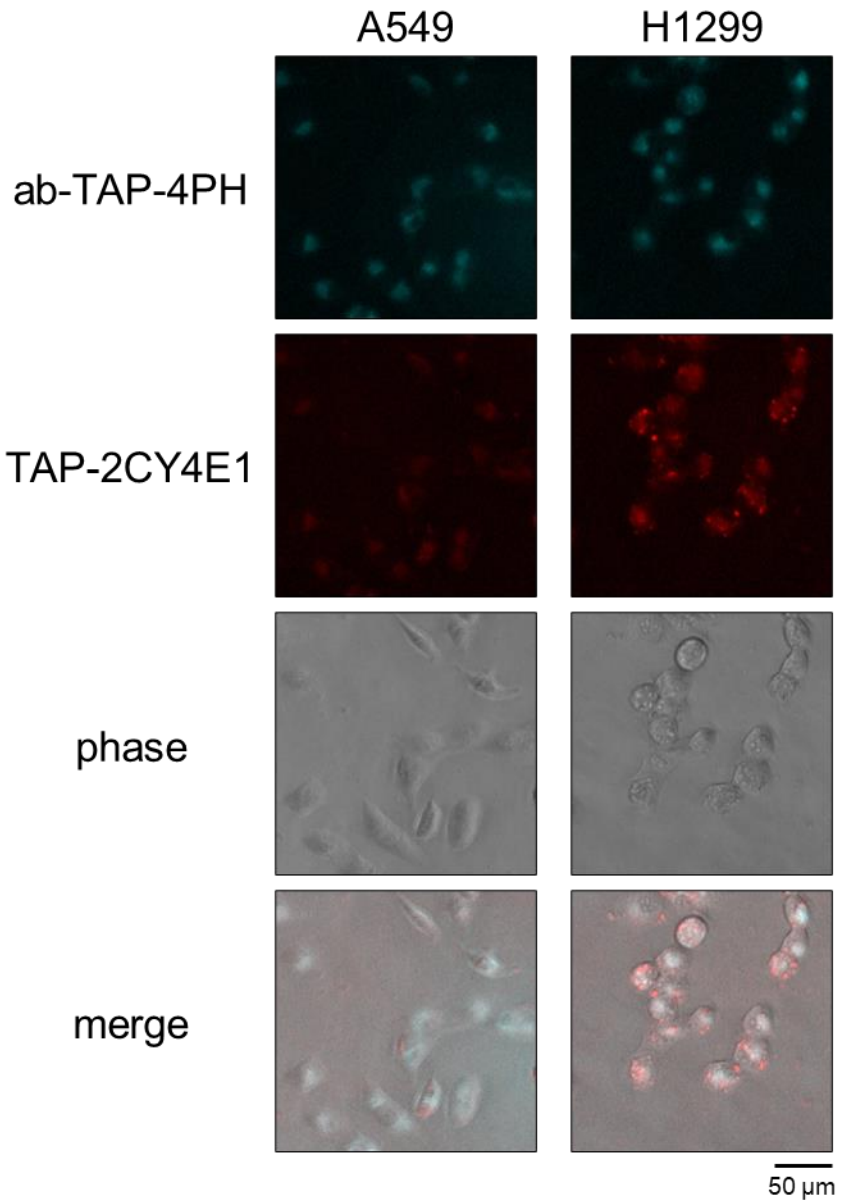

Figure 3-11. Fluorescence imaging of ab-TAP-4PH and TAP-2CY4E1 in A549 and H1299 cells.

Fluorescence microscopy images of A549 and H1299 cells costained with ab-TAP-4PH (20 μM) and TAP-2CY4E1 (10 μM) for 30 min at 37℃. ab-TAP-4PH, Ex 360/40 nm, Em 460/50 nm; TAP-2CY4E1, Ex 452 nm, Em 607 nm. Scale bar: 50 μm.

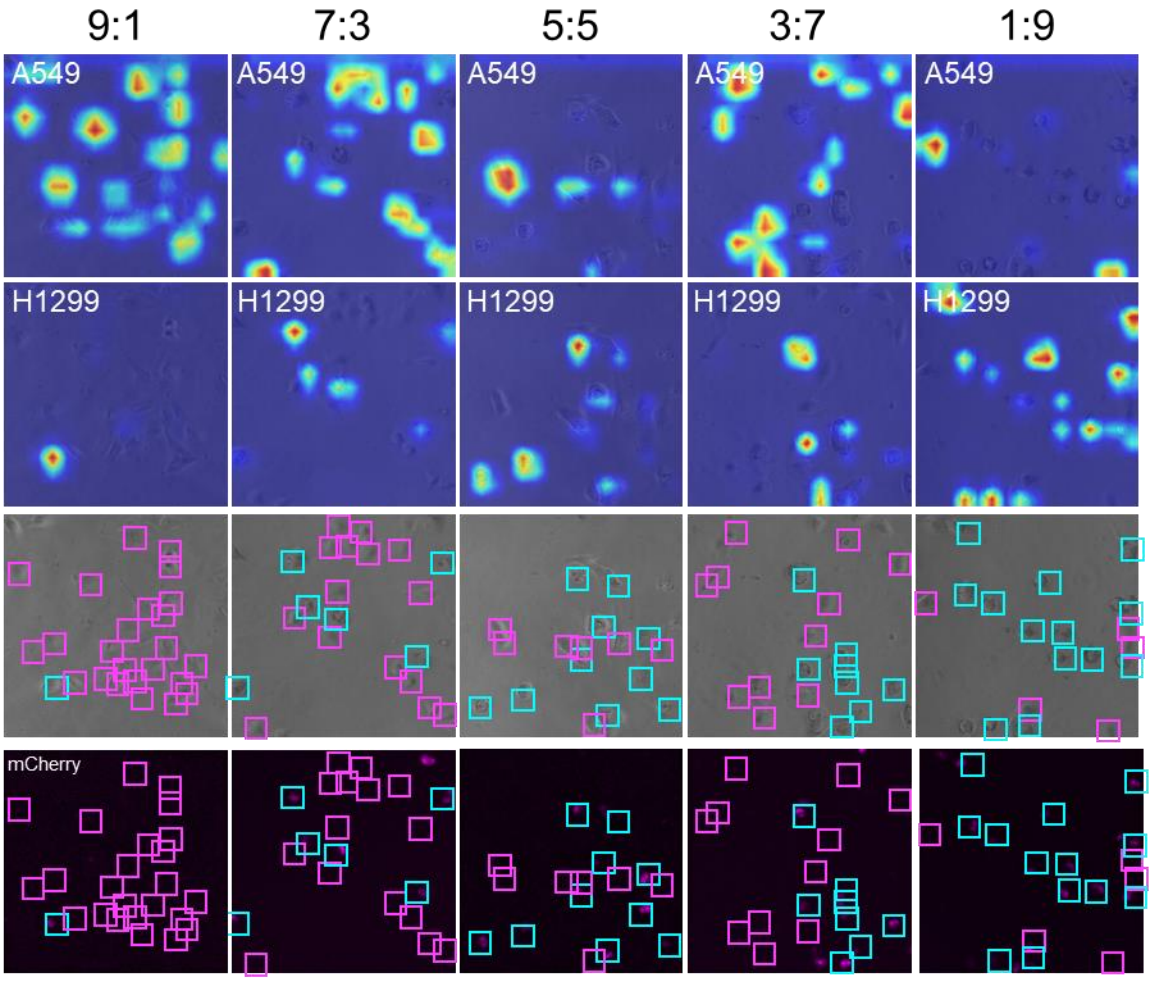

Figure 3-12. Detection of A549 and H1299 individual cells in mixed culture.

The heatmap predicting cell types was generated from the deep learning model. The magenta squares indicate cells predicted as A549, while the cyan squares indicate cells predicted as H1299.

Table 3-3. Precision, Recall, and F1 score values of cell prediction.

Ratio of A549 : H1299	9:1	7:3	5:5	3:7	1:9
Precision	0.987	0.988	0.953	0.943	0.895
Recall	0.868	0.942	0.952	0.953	0.944
F1 score	0.924	0.964	0.952	0.948	0.919

Values of Precision, Recall, and F1 score were calculated using the formula described in the method section, utilizing following values: TP (True Positive): The number of cells predicted as A549 that were actually A549; FP (False Positive): The number of cells predicted as A549 but were actually H1299; TN (True Negative): The number of cells predicted as H1299 that were actually H1299; FN (False Negative): The number of cells predicted as H1299 but were actually A549. These values obtained by twenty independent images in each condition.

Table 3-4. Precision and Recall score values of cell detection using images.

Condition	Precision	Recall
Multiplex staining	0.977	0.933
Phase contrast only	0.676	0.547
ab-TAP-4PH only	0.694	0.610
TAP-2CY4E1 only	0.621	0.535

Values of Precision and Recall score were calculated using the formula described in the method section, utilizing following values: TP (True Positive): The number of cells predicted as A549 that were actually A549; FP (False Positive): The number of cells predicted as A549 but were actually H1299; TN (True Negative): The number of cells predicted as H1299 that were actually H1299; FN (False Negative): The number of cells predicted as H1299 but were actually A549.

3.4.7. Detection of PPM1D-inhibited adipocytes with deep learning

White adipocytes with PPM1D inhibition differentiated into a novel subtype characterized by multilocular lipid droplets and increased mitochondrial activity (refer to **Section 2 Figure 2-5, 2-6, and 2-8**). White adipocytes on day 8 of differentiation (day+0), control white adipocytes 7 days post day+8 differentiation (Ctrl day+7), and white adipocytes treated with PPM1D inhibitor for 7 days post day+8 differentiation (SL-176 day+7) were stained with ab-TAP-4PH and TAP-2CY4E1 and observed under a fluorescence microscope (**Figure 3-13**). SL-176 day+7 exhibited lower fluorescence intensity of ab-TAP-4PH compared to day+0 and Ctrl day+7. Furthermore, TAP-2CY4E1 showed strong fluorescence in the lipid droplets of adipocytes, with SL-176 day+7 exhibiting smaller-sized lipid droplets compared to day+0 and Ctrl day+7. Day+0 cells were defined as state I type cells, Ctrl day+7 cells with large lipid droplets as state II type cells, and SL-176 day+7 cells with smaller, multilocular lipid droplets as state III type cells. A deep learning model was trained to classify these three cell types and analyze the differentiation process of adipocytes under PPM1D inhibition (**Figure 3-14**). The results showed that state I type cells were predominant in day+0, state II type cells in Ctrl day+7, and state III type cells in SL-176 day+7. This classification effectively distinguished day+0, Ctrl day+7, and SL-176 day+7 populations. In the control group, the proportion of state II type cells increased progressively from day+0 to day+2, day+4, and day+7, while the proportion of state I type cells decreased. Conversely, in the SL-176 group, the proportion of state II type cells increased from day+0 to day+4 and then decreased from day+4 to day+7. Meanwhile, the proportion of state III type cells gradually increased from day+0 to day+7, with a concurrent decrease in state I type cells. The results demonstrated that the deep learning model effectively distinguished changes in cell type populations, even though single-cell-level classification was not achieved.

Changes in the proportions of the three cell types are presented in **Table 3-5** and **Figure 3-15**. At the start of differentiation (day+0), almost all cells (around 99%) were classified as state I. In the

control group, state II cells started to appear by day+2 and gradually increased, eventually making up the majority by day+7 (approximately 80%). State III cells remained a minor subset during this period. In contrast, in the SL-176-treated group, state II cells increased rapidly between day+2 and day+4. However, by day+7, most cells (over 80%) had shifted to state III, which is characterized by smaller, multilocular lipid droplets. These results indicate that, under control conditions, cells progressively transition from state I to state II (with large lipid droplets) over seven days. Meanwhile, under PPM1D inhibition, cells initially increase in state II but ultimately adopt the state III phenotype marked by smaller, multilocular lipid droplets. In conclusion, multiplex staining with TAP derivatives effectively distinguished populations of white adipocytes.

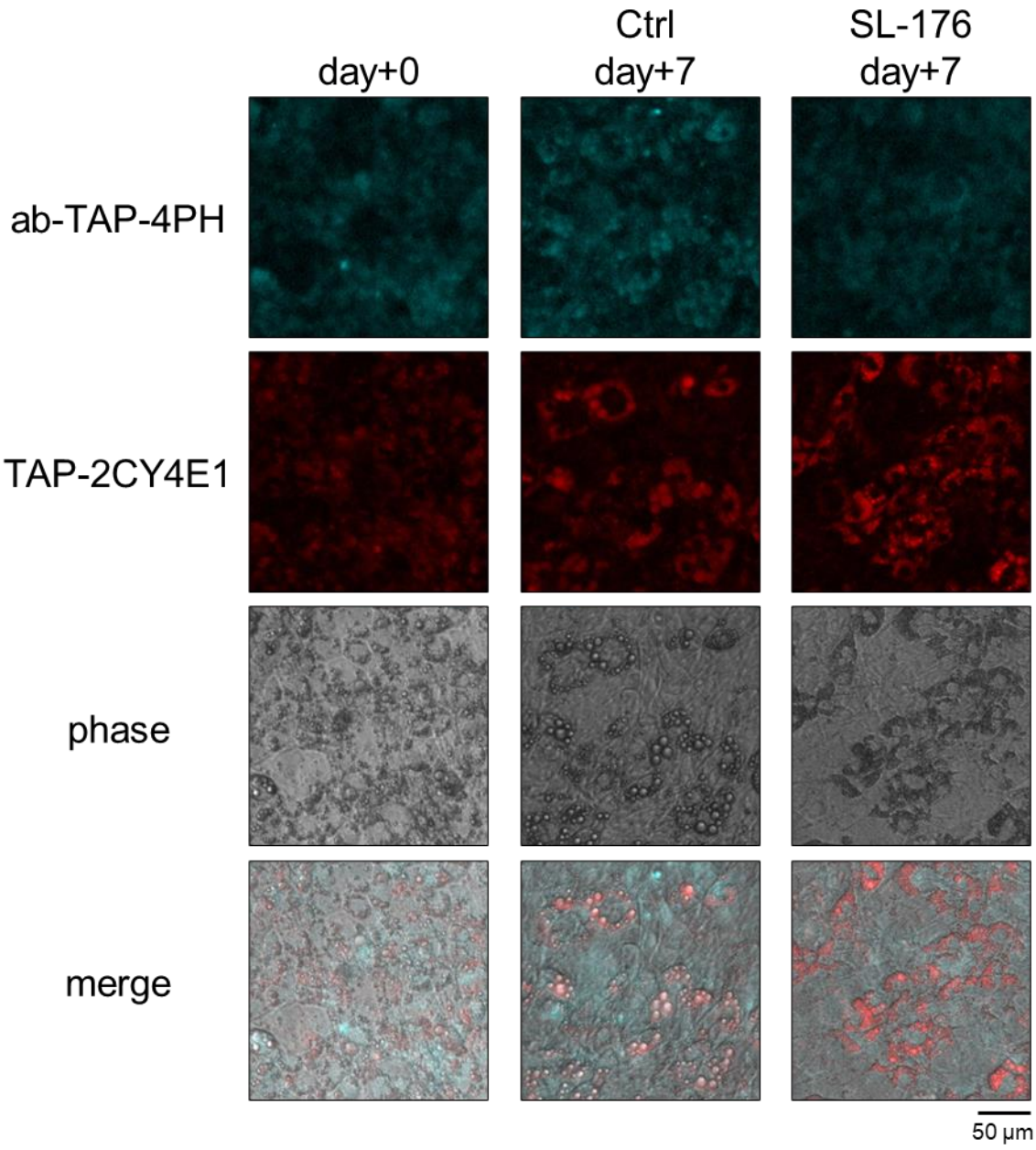

Figure 3-13. Fluorescence imaging of ab-TAP-4PH and TAP-2CY4E1 in 3T3-L1 adipocytes.

Fluorescence microscopy images of 3T3-L1 adipocytes day8 (day+0), 3T3-L1 adipocytes day15 (Ctrl day+7) and PPM1D-inhibited 3T3-L1 adipocytes (SL-176 day+7) costained with ab-TAP-4PH TAP-2CY4E1 (20 μM) and TAP-2CY4E1 (10 μM) for 30 min at 37℃. 3T3-L1 cells were differentiated into adipocytes for 8 days followed by treatment of SL-176 (15 μM) for 7 days. ab-TAP-4PH, Ex 360/40 nm, Em 460/50 nm; TAP-2CY4E1, Ex 452 nm, Em 607 nm. Scale bar: 50 μm.

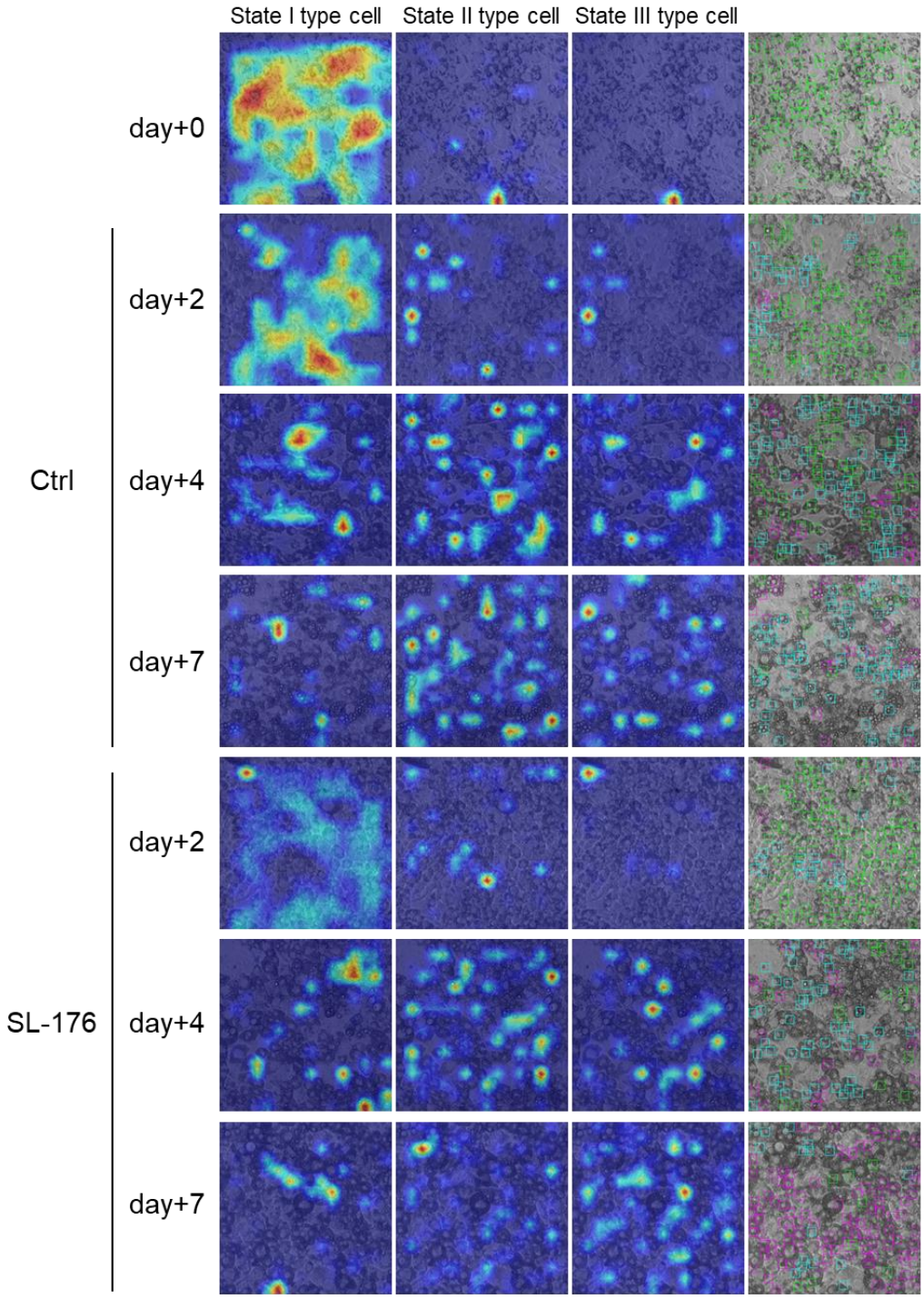

Figure 3-14. Prediction of adipocyte cell types.

The heatmap predicting cell types was generated using the deep learning model. Day+0 cells were defined as state I type cells, Ctrl day+7 cells with large lipid droplets as state II type cells, and SL-176 day+7 cells with small, multilocular lipid droplets as state III type cells. The green squares indicate cells predicted as state I type cell, the cyan squares indicate cells predicted as state II type cell, and the magenta squares indicate cells predicted as state III type cell.

Table 3-5. Probability of adipocyte cell types.

		State I type cell (%)	State II type cell (%)	State III type cell (%)
	day+0	99.28 ± 0.58	0.72 ± 0.58	0.00 ± 0.00
	day+2	71.72 ± 2.91	26.91 ± 2.93	1.37 ± 0.65
Ctrl	day+4	29.71 ± 4.76	67.48 ± 4.97	2.81 ± 0.49
	day+7	0.71 ± 0.40	79.90 ± 1.54	19.39 ± 1.37
	day+2	81.81 ± 1.22	17.90 ± 1.18	0.29 ± 0.15
SL-176	day+4	3.52 ± 1.66	83.67 ± 2.82	12.80 ± 3.01
	day+7	0.00 ± 0.00	16.15 ± 4.70	83.85 ± 4.70

Values are presented as the mean ± S.D. of values obtained via four independent sets, each set consisting of 45 pictures out of a total of 180 pictures in each condition.

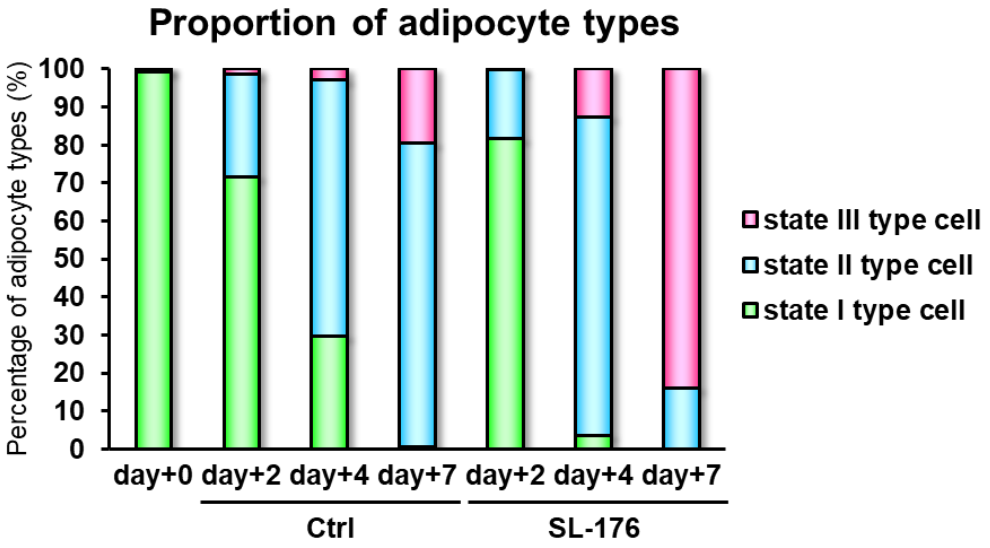

Figure 3-15. Proportion of adipocyte cell types.

Bar chart showing the percentages of adipocyte cell types (state I, state II, and state III) in 3T3-L1 adipocytes from day+0 to day+7, with and without SL-176 treatment.

3.5. Discussion

ab-TAP-4PH, which contains an aminobutyl group in its side chain, exhibited pH-dependent changes in fluorescence intensity, with an increase in fluorescence intensity as the pH decreased. The analysis of intracellular localization revealed a strong localization in the ER and lysosomes. The pH of lysosomes is in the range of 4.5 to 5.0, representing a low pH environment within the cell [21]. Therefore, it is suggested that the high fluorescence intensity of ab-TAP-4PH in lysosomes is due to this acidic environment. TAP-2CY4E1 exhibited high fluorescence intensity in DCM, which is a highly hydrophobic solvent, and localization analysis indicated strong localization in the ER and lipid droplets. Lipid droplets are highly hydrophobic organelles surrounded by a phospholipid monolayer containing triacylglycerols and cholesterol [22], which explains the strong fluorescence of TAP-2CY4E1 in hydrophobic environments. Abnormal pH changes are associated with cellular dysfunction and are observed in various diseases, including cancer and neurodegenerative disorders [23]. Moreover, the complex parameter of polarity is suggested to be closely related to various physiological processes such as membrane fusion, protein denaturation, and peptide aggregation. Abnormal polarity changes are closely linked to diseases like diabetes and cancer [24]. Therefore, multiplex staining with ab-TAP-4PH and TAP-2CY4E1 has the potential to detect cellular dysfunction caused by abnormal pH changes and polarity shifts. Additionally, it has been demonstrated that ab-TAP-4PH and TAP-2CY4E1 can visualize various cellular states due to their broad localization and fluorescence emission within cells.

The addition of ab-TAP-4PH and TAP-2CY4E1 showed almost no cytotoxicity at high concentrations in A549 and MEF cells. Furthermore, they could be easily removed through wash-out with PBS, having little to no impact on the cells even after removal. These findings demonstrate that ab-TAP-4PH and TAP-2CY4E1 are extremely low in cytotoxicity and can be used as fluorescent probes in live cells.

Staining human alveolar basal epithelial adenocarcinoma cells A549 and human non-small cell

lung cancer-derived H1299 with ab-TAP-4PH and TAP-2CY4E1 revealed distinct fluorescence patterns for each cell type. These differences in fluorescence patterns are likely due to variations in hydrophobic regions, pH, and the sizes of intracellular organelles between A549 and H1299 cells Furthermore, by mixing A549 and H1299 cells and staining them with ab-TAP-4PH and TAP-2CY4E1, machine learning was employed for cell identification, demonstrating the ability to distinguish cell types at the single-cell level. In live cell identification, several fluorescent probes that are protein-oriented or metabolism-oriented and specialized for identifying specific cell types have been reported [5]. Multiplex staining with ab-TAP-4PH and TAP-2CY4E1, which broadly localize within cells and visualize cellular states, suggests a novel approach for facilitating the identification of various cell types.

Multiplex staining with ab-TAP-4PH and TAP-2CY4E1 successfully distinguished different types of adipocytes. In control (Ctrl) adipocytes, both state II cells with large lipid droplets and state III cells with small, multilocular lipid droplets increased over the 7-day differentiation period, with state II cells eventually becoming predominant. By contrast, in PPM1D-inhibited adipocytes, state II cells initially increased up to day+4 but then decreased by day+7, while state III cells gradually became more frequent and ultimately predominated on day+7. These findings suggest that PPM1D inhibition may promote the formation of state III cells. It is also possible that state III cells arise through different pathways under control conditions and under PPM1D inhibition.

In this study, single-cell-level identification of adipocytes was not achieved. Whereas PPM1D-inhibited adipocytes developed small, multilocular lipid droplets, Ctrl adipocytes formed large lipid droplets, indicating that the deep learning model likely relies on changes in lipid droplet morphology for distinguishing different adipocyte types. Developing TAP derivatives that stain nuclei, along with multiplex staining using three types of TAP derivatives, could make single-cell-level identification of adipocytes feasible. In the future, such an approach would enable more detailed analyses of the novel subtype that emerges under PPM1D inhibition.

In this study, I developed a novel method for visualizing the cellular states and identifying cells at the single-cell level using multiplex staining with ab-TAP-4PH and TAP-2CY4E1.

3.6. References

1. A. M. Cypess, Reassessing Human Adipose Tissue, *N. Engl. J. Med.*, **386**, 768–779 (2022). https://doi.org/10.1056/NEJMRA2032804/SUPPL_FILE/NEJMRA2032804_DISCLOSURES.PDF.
2. A. J. Richard, U. White, C. M. Elks, and J. M. Stephens, Adipose Tissue: Physiology to Metabolic Dysfunction, *Endotext*, (2020).
3. B. Maniyadath, Q. Zhang, R. K. Gupta, and S. Mandrup, Adipose tissue at single-cell resolution, *Cell Metab.*, **35**, 386–413 (2023). https://doi.org/10.1016/J.CMET.2023.02.002.
4. A. K. Sárvári, E. L. Van Hauwaert, L. K. Markussen, E. Gammelmark, A. B. Marcher, M. F. Ebbesen, R. Nielsen, J. R. Brewer, J. G. S. Madsen, and S. Mandrup, Plasticity of Epididymal Adipose Tissue in Response to Diet-Induced Obesity at Single-Nucleus Resolution, *Cell Metab.*, **33**, 437-453.e5 (2021). https://doi.org/10.1016/J.CMET.2020.12.004/ASSET/7FB97ECC-A0BA-46DD-96C6-AF3CAC243E49/MAIN.ASSETS/GR6.JPG.
5. X. Liu and Y. T. Chang, Fluorescent probe strategy for live cell distinction, *Chem. Soc. Rev.*, **51**, 1573–1591 (2022). https://doi.org/10.1039/D1CS00388G.
6. P. Gao, W. Pan, N. Li, and B. Tang, Fluorescent probes for organelle-targeted bioactive species imaging, *Chem. Sci.*, **10**, 6035–6071 (2019). https://doi.org/10.1039/C9SC01652J.
7. N. E. Choi, J. Y. Lee, E. C. Park, J. H. Lee, and J. Lee, Recent Advances in Organelle-Targeted Fluorescent Probes, *Mol. 2021, Vol. 26, Page 217*, **26**, 217 (2021). https://doi.org/10.3390/MOLECULES26010217.
8. Y. Wen, N. Jing, F. Huo, and C. Yin, Recent progress of organic small molecule-based fluorescent probes for intracellular pH sensing, *Analyst*, **146**, 7450–7463 (2021). https://doi.org/10.1039/D1AN01621K.
9. P. E. Hande, Y. G. Shelke, A. Datta, and S. J. Gharpure, Recent Advances in Small Molecule-Based Intracellular pH Probes, *ChemBioChem*, **23**, e202100448 (2022). https://doi.org/10.1002/CBIC.202100448.
10. X. Tian, L. C. Murfin, L. Wu, S. E. Lewis, and T. D. James, Fluorescent small organic probes for biosensing, *Chem. Sci.*, **12**, 3406–3426 (2021). https://doi.org/10.1039/D0SC06928K.
11. K. Namba, A. Osawa, S. Ishizaka, N. Kitamura, and K. Tanino, Direct synthesis of fluorescent 1,3a,6a-triazapentalene derivatives via click-cyclization-aromatization cascade reaction, *J. Am. Chem. Soc.*, **133**, 11466–11469 (2011). https://doi.org/10.1021/JA203917R/SUPPL_FILE/JA203917R_SI_002.CIF.
12. K. Namba, A. Mera, A. Osawa, E. Sakuda, N. Kitamura, and K. Tanino, One-pot synthesis of highly fluorescent 2,5-disubstituted-1,3a,6a- triazapentalene, *Org. Lett.*, **14**, 5554–5557 (2012). https://doi.org/10.1021/OL302668Y/SUPPL_FILE/OL302668Y_SI_001.PDF.

13. A. Nakayama, S. Nishio, A. Otani, A. Mera, A. Osawa, K. Tanino, and K. Namba, Substituent Effect at the C4-Position of 1,3a,6a-Triazapentalene, *Chem. Pharm. Bull.*, **64**, 830–837 (2016). https://doi.org/10.1248/CPB.C16-00196.
14. A. Mera, M. Ito, A. Nakayama, and K. Namba, Synthesis of 2,6-Disubstituted-1,3a,6a-Triazapentalenes and Their Fluorescence Properties, *Chem. Lett.*, **46**, 539–542 (2017). https://doi.org/10.1246/CL.170078.
15. B. Verbelen and W. Dehaen, Two-Step Synthesis of Fluorescent 3-Arylated 1,3a,6a-Triazapentalenes via a Three-Component Triazolization Reaction, *Org. Lett.*, **18**, 6412–6415 (2016). https://doi.org/10.1021/ACS.ORGLETT.6B03309/ASSET/IMAGES/LARGE/OL-2016-03309J_0001.JPEG.
16. K. Namba, A. Osawa, A. Nakayama, A. Mera, F. Tano, Y. Chuman, E. Sakuda, T. Taketsugu, K. Sakaguchi, N. Kitamura, and K. Tanino, Synthesis of yellow and red fluorescent 1,3a,6a-triazapentalenes and the theoretical investigation of their optical properties, *Chem. Sci.*, **6**, 1083–1093 (2015). https://doi.org/10.1039/C4SC02780A.
17. R. Kamada, F. Tano, F. Kudoh, N. Kimura, Y. Chuman, A. Osawa, K. Namba, K. Tanino, and K. Sakaguchi, Effective Cellular Morphology Analysis for Differentiation Processes by a Fluorescent 1,3a,6a-Triazapentalene Derivative Probe in Live Cells, *PLoS One*, **11**, e0160625 (2016). https://doi.org/10.1371/JOURNAL.PONE.0160625.
18. A. Nakayama, A. Otani, T. Inokuma, D. Tsuji, H. Mukaiyama, A. Nakayama, K. Itoh, A. Otaka, K. Tanino, and K. Namba, Development of a 1,3a,6a-triazapentalene derivative as a compact and thiol-specific fluorescent labeling reagent, *Commun. Chem. 2020 31*, **3**, 1–9 (2020). https://doi.org/10.1038/s42004-019-0250-0.
19. D. Tsuji, A. Nakayama, R. Yamamoto, S. Nagano, T. Taniguchi, R. Sato, S. Karanjit, N. Muguruma, T. Takayama, K. Itoh, and K. Namba, 1,3a,6a-Triazapentalene derivatives as photo-induced cytotoxic small fluorescent dyes, *Commun. Chem. 2023 61*, **6**, 1–11 (2023). https://doi.org/10.1038/s42004-023-00838-0.
20. E. Moen, D. Bannon, T. Kudo, W. Graf, M. Covert, and D. Van Valen, Deep learning for cellular image analysis, *Nat. Methods 2019 1612*, **16**, 1233–1246 (2019). https://doi.org/10.1038/s41592-019-0403-1.
21. J. Zeng, O. S. Shirihai, and M. W. Grinstaff, Modulating lysosomal pH: a molecular and nanoscale materials design perspective, *J. life Sci. (Westlake Village, Calif.)*, **2**, 25 (2020). https://doi.org/10.36069/JOLS/20201204.
22. T. Fujimoto and R. G. Parton, Not Just Fat: The Structure and Function of the Lipid Droplet, *Cold Spring Harb. Perspect. Biol.*, **3**, a004838 (2011). https://doi.org/10.1101/CSHPERSPECT.A004838.
23. W. Chen, X. Ma, H. Chen, S. Hua Liu, and J. Yin, Fluorescent probes for pH and alkali metal

ions, *Coord. Chem. Rev.*, **427**, 213584 (2021). https://doi.org/10.1016/J.CCR.2020.213584.

24. H. Xiao, P. Li, and B. Tang, Recent progresses in fluorescent probes for detection of polarity, *Coord. Chem. Rev.*, **427**, 213582 (2021). https://doi.org/10.1016/J.CCR.2020.213582.

4. Conclusions

White adipocytes play a crucial role in energy storage and release, maintaining systemic energy homeostasis. Excessive formation of lipid droplets, which store energy, leads to hypertrophy of white adipocytes, contributing to obesity. PPM1D is involved in various physiological functions, including immune responses and spermatogenesis. Recently, PPM1D has been suggested to play a role in lipid accumulation and metabolic regulation. Our laboratory has previously demonstrated that inhibition of PPM1D suppresses adipocyte differentiation.

In Chapter 2, the role of PPM1D in adipocyte differentiation and lipid droplet formation was analyzed. PPM1D was shown to regulate differentiation during the early stages of white adipocyte differentiation by inducing the expression of transcription factors. Additionally, PPM1D was found to control lipid droplet formation by dephosphorylating perilipin 1 at Ser511. Furthermore, it was suggested that PPM1D is involved in the differentiation of a novel subtype of adipocytes with characteristics of beige adipocytes. These results clarify that PPM1D regulates adipocyte differentiation and lipid droplet formation.

In Chapter 3, a novel cell identification method using new TAP derivatives was developed. Multicolor staining was performed using ab-TAP-4PH, which possesses an aminobutyl group, and TAP-2CY4E1, which includes 3-cyano benzoic acid, both newly designed TAP derivatives. When cellular images of lung cancer-derived p53 wild-type and p53-deficient cells were analyzed using a deep learning model, the cells were identified with exceptionally high accuracy. These findings demonstrate that multicolor staining with the novel TAP derivatives ab-TAP-4PH and TAP-2CY4E1 enables highly accurate identification of cellular states and responses at the single-cell level. Furthermore, the cell identification method through multiplex staining with TAP derivatives by the deep learning model successfully identified the novel subtype induced by PPM1D inhibition in adipocytes. In the future, achieving single-cell-level identification in adipocytes is expected to enable detailed analyses of this

novel subtype.

In summary, I have elucidated the regulatory mechanisms of adipocyte differentiation and maturation mediated by PPM1D phosphatase. Furthermore, I have demonstrated a novel single-cell analysis method using new TAP derivatives and deep learning. This study has the potential to contribute to the development of treatments for obesity and obesity-related diseases.

5. Acknowledgements

I would like to express my greatest appreciation to my supervisor Professor Kazuyasu Sakaguchi (Laboratory of Biological Chemistry) for his guidance over the past six years. Professor Sakaguchi provided me with valuable instruction on research methodologies, how to present at conferences, and document preparation, all of which were essential for the execution of my research.

I would like to thank Associate Professor Rui Kamada (Laboratory of Biological Chemistry) for guiding me through many aspects of my research, from discussions essential for executing my work to preparing for conference presentations. I am grateful for your support that has allowed me to advance my research to this point.

I would like to express my gratitude to Professor Kazuhiro Abe (Laboratory of Molecular Biochemistry), Professor Akinori Takaoka (Division of Signaling in Cancer and Immunology), Professor Ken'ichiro Matsumoto (Laboratory of Biosynthetic Chemistry), and Professor Keiji Tanino (Laboratory of Organic Chemistry II) for their valuable comments and discussions on my thesis.

I am grateful to Professor Keiji Tanino (Laboratory of Organic Chemistry II) who provided ab-TAP-4PH, TAP-2CY4E1, and PPM1D inhibitor SL-176.

I wish to express my appreciation to Assistant Professor Natsumi Nakagawa (Laboratory of Biological Chemistry) who provide helpful comments and support. I am very grateful to all the members of the Laboratory of Biological Chemistry, with special thanks to Mr. Daiki Kurosu.

Finally, I would like to thank my family for their support and encouragement throughout my studies and my life.